

2015

Characterizing targeted drug delivery and endothelial cell dynamics using in vitro blood vessel models

Antony Thomas
Lehigh University

Follow this and additional works at: <http://preserve.lehigh.edu/etd>



Part of the [Biomedical Engineering and Bioengineering Commons](#)

Recommended Citation

Thomas, Antony, "Characterizing targeted drug delivery and endothelial cell dynamics using in vitro blood vessel models" (2015). *Theses and Dissertations*. 2842.
<http://preserve.lehigh.edu/etd/2842>

This Dissertation is brought to you for free and open access by Lehigh Preserve. It has been accepted for inclusion in Theses and Dissertations by an authorized administrator of Lehigh Preserve. For more information, please contact preserve@lehigh.edu.

CHARACTERIZING TARGETED DRUG DELIVERY and
ENDOTHELIAL CELL DYNAMICS USING *IN VITRO* BLOOD
VESSEL MODELS

By

Antony Thomas

Presented to the Graduate and Research Committee
of Lehigh University
in Candidacy for the Degree of
Doctor of Philosophy

In
Bioengineering

Lehigh University

August 2015

Copyright © 2015
Antony Thomas
All Rights Reserved

Approved and recommended for acceptance as a dissertation in partial fulfillment of the requirements for the degree of Doctor of Philosophy.

Antony Thomas

Characterizing targeted drug delivery and endothelial cell dynamics using *in vitro* blood vessel models

Defense Date

Dr. Yaling Liu, Dissertation Director, Chair

Accepted Date

Committee Members:

Dr. Yaling Liu

Dr. Linda Lowe-Krentz

Dr. Daniel Ou-Yang

Dr. Xuanhong Cheng

Acknowledgements

I would like to thank everyone who has made this dissertation possible. This dissertation represents a relationship with many amazing and inspiring people that I have met over the years since beginning my graduate work. First I would like to thank my advisor Dr. Yaling Liu, who has supported and pushed me throughout my time in graduate school. I would like to thank my committee members Dr. Linda Lowe-Krentz, Dr. Daniel Ou-Yang, and Dr. Xuanhong Cheng for their advice and guidance. I would also like to thank Dr. Vladimir Muzykantov and Dr. Susan Perry for their considerable assistance with my study.

Special gratitude goes to all the Bioengineering department professors and supporting staff. Thank you for going above and beyond your daily responsibilities to create a supportive environment. I am also very grateful to my labmates, past and present, who has provided me with valuable insight and resources through productive discussions and were always around to bounce ideas off, troubleshoot, and learn from.

I would finally like to thank all my friends and family, especially my parents Thomas and Philomina, and my wife Anu. Without their support and encouragement this work would never have been possible. I would also like to thank my sister and brother-in-law who showed continuous support and were always there for me.

Table of contents

List of Tables	vii
List of figures	ix
ABSTRACT	1
Chapter 1: Introduction	6
Chapter 2: Background and Significance	11
2.1 Blood vessel; its structure and function	15
2.1.1 Types of Blood Vessels	16
2.2 Targeted Drug delivery	18
2.3 Drug carrier properties	19
2.4 Specificity in drug carrier targeting	20
2.5 Influence of vessel geometry in drug carrier distribution	22
2.6 Distribution of drug carriers under the influence of RBC	23
2.7 Current challenges in the study of drug delivery and distribution	24
2.8 Microfluidics	24
2.9 Biomimetic platforms	25
Chapter 3: Model 1: endothelial cell receptor protein (ICAM-1) coated microvasculature mimicking platform	28
3.1 Introduction	28
3.2 Methods	29
3.2.1 Fabrication of microfluidic device	29
3.2.2 ICAM-1 functionalized PDMS substrate	29
3.2.3 Substrate ICAM-1 density characterization	30
3.2.4 Anti-ICAM-1 coated micro/nano particles	31
3.2.5 Particle anti-ICAM-1 density characterization	31
3.3 Results and Discussion	33

3.3.1	Characterization of particle and PDMS substrate protein densities	33
3.3.2	Specificity of anti-ICAM-1 coated particle binding to ICAM-1 coated surface	33
3.4	Conclusion	35
Chapter 4:	Characterization of targeted nano and micro particle delivery in microcirculation	36
4.1	Introduction	36
4.2	Methods	37
4.2.1	Microfluidic flow test cases	37
4.3	Results and Discussion	42
4.3.1	210 nm and 2 μ m particle binding distribution	42
4.3.2	Comparison between binding of 210 nm particle and 2 μ m particles	48
4.3.3	Daughter channels with asymmetric flow velocity	51
4.3.4	Attachment and detachment profiles	54
4.3.5	Derivation of attachment and detachment rates from experimental data	56
4.3.6	Normalization process to bring all flow cases to a total particle count of 10^6 /flow case	58
4.4	Conclusion	60
Chapter 5:	Model 2: endothelial cell coated vascular morphology mimicking platform	63
5.1	Introduction	63
5.2	Materials and Methods	65
5.2.1	Materials	65
5.2.2	Fabrication of bio-mimetic blood vessel model	65
5.2.3	Endothelial cell culture in the device	67
5.2.4	Application of shear stress	67
5.3	Results and Discussion	69

5.3.1 Design of microfluidic device	69
5.3.2 On-chip cell culture	70
5.3.3 endothelial cell alignment and stress fiber arrangement under FSS	71
5.4 Conclusion	77
Chapter 6: Dynamics of endothelial activation by local action of pro-inflammatory cytokines	78
6.1 Introduction	78
6.2 Methods	81
6.2.1 TNF- α treatment	81
6.2.2 Binding of anti-ICAM-1 coated particles on BAOEC layer	81
6.2.3 Preparation and characterization of anti-ICAM-1 coated particles	83
6.3 Results and Discussion	86
6.3.1 Targeted binding of anti-ICAM-1 coated particles on BAOEC layer	86
6.3.2 Time course study on TNF- α based expression of surface ICAM-1 by BAOECs under static culture	88
6.3.3 BAOECs treated with TNF- α from the basal and apical side of the cell	88
6.3.4 Characterization of flow-mediated localized BAOEC activation using fluorescent probes	89
6.3.5 ICAM-1 and F-actin distribution pattern along the channel length	92
6.3.6 Targeted binding of anti-ICAM-1 coated particles of 1 micron size	95
6.3.7 Dynamic nature of surface ICAM-1 expression by endothelial cells	96
6.4 Conclusion	98

Chapter 7:Characterizing vascular permeability using a biomimetic microfluidic blood vessel model	100
7.1 Introduction	100
7.1.1 Vascular permeability and pathological significance	100
7.1.2 Associated diseases	101
7.1.3 Dynamic nature of vessel permeability	102
7.1.4 Current <i>in vivo</i> and <i>in vitro</i> platforms	103
7.1.5 Significance of FSS	105
7.1.6 Thrombin	106
7.2 Material and Methods	109
7.2.1 Fabrication and endothelial cell culture	109
7.2.2 Thrombin treatment and cell permeability assay	110
7.2.3 Quantifying vascular permeability	111
7.2.4 Localization of Actin Filaments and Immunofluorescence Staining	112
7.2.5 Statistical analysis	114
7.3 Results and Discussions	115
7.3.1 On-chip cell culture	115
7.3.2 Characterizing vascular permeability on biomimetic blood vessel model	117
7.3.3 Characterizing vascular permeability using transwell inserts	120
7.3.4 F-actin cytoskeletal remodeling	121
7.3.5 Comparison of biomimetic model to transwell insert study	126
7.4 Conclusion	128
Chapter 8:Some general discussion and suggestions for future research	130

8.1 General discussions	130
8.2 Future research	133
8.2.1 Co-culture of endothelial cells and SMCs	
133	
8.2.2 Leukocyte recruitment and trans-migration studies	134
8.2.3 Modeling tumor environment	135
References	137
Curriculum Vitae	150

List of Tables

Table 1: Shear rates in the parent channel and in daughter channels a and b for the different flow cases studied. Image shows the top view of the flow channel design that produces asymmetric flow in daughter channels.....	51
Table 2: Detailed steps of the normalization process performed to bring all flow cases to a total particle count of 106/flow case.....	58
Table 3: Final particle concentration (#/ml) for 210 nm and 1 μ m particles. The total particle volume is constant for both particles.....	81
Table 4: FSS and corresponding volumetric flow rate values along with flow time for 6, 12 and 18 dyne/cm ² cases. Flow time decreases with FSS to maintain the 'total number of particles/flow case' a constant.....	81

List of figures

Figure 1: Layers of the blood vessel. Outer tunica adventitia, middle tunica media, and inner tunica intima, their corresponding cell composition and functions. _____ 12

Figure 2: Schematics of the vasculature endothelium and selected molecular determinants that play a pivotal role in targeted drug delivery to the endothelium. Surface-modified drug carriers decorated with specific antibodies, peptides, or small molecules were shown to accumulate in the endothelium. _____ 18

Figure 3: Binding density of anti-ICAM-1 and negative control (Goat IgG control) antibody coated (A) 210 nm particles and (B) 2 μm particles under 200 s^{-1} shear rate for both pure buffer and RBC 25% flow cases. _____ 33

Figure 4: (A) CAD design of microchannel geometry, enlarged part illustrates the straight and bifurcation section of the channel; (B) The flow test set-up. _____ 39

Figure 5: Normalized particle binding density ($\#/\text{mm}^2$) at shear rates 200-1600 s^{-1} ; at branching section of channels under (A) pure buffer flow and (B) RBC flow for 210 nm particles; at straight section of channels under (C) pure buffer flow and (D) RBC flow for 210 nm particles. Binding densities are plotted for 1905.3, 1257.1 and 625.8 anti-ICAM-1/ μm^2 particle antibody densities. Error bars represent standard deviation for three independent flow cases each. _____ 42

Figure 6: Particle binding density ($\#/\text{mm}^2$) at shear rates between 200-1600 s^{-1} under RBC flow for 210 nm particles at (A) branching section of channels and (B) straight section of channels without data normalization; (C) Particle binding density of 210 nm particles with an anti-ICAM-1 coating density of 1905.3/ μm^2 under RBC flow at 200 s^{-1} and 550 s^{-1} shear rate without normalization. 200 s^{-1} shear rate case was subjected to an extended flow of 45 minutes to match with the total number of particles flown for the 550 s^{-1} case (15 minutes flow). _____ 43

Figure 7: (A) Zoomed in image of 210 nm particle binding at 1250 s^{-1} shear rate for 1905.25/ μm^2 anti-ICAM-1 particle coating density; (B) Phase contrast image of Fig S2 A ; (C) 6X times zoomed in image scan of Fig S2 A showing each 210 nm particle. _____ 44

Figure 8: Confocal microscopy scan of free suspending 210 nm particle localization to the near wall region for: (A) Pure buffer case at 200/s shear rate (B) RBC 25% case at 200/s shear rate (C) RBC 25% case at 550/s shear rate (D) RBC 25% case at 900/s shear rate in the 100 μm wide microfluidic channel at a particle concentration of 108/ml. The image is a sum of the stack of confocal scan images from 1 μm above the channel base to a height of 5 μm in the z direction. _____ 44

Figure 9: Normalized particle binding density (#/mm²) at shear rates between 200-1600 s⁻¹; at branching section of channels under (A) pure buffer flow and (B) RBC 25% flow for 2 μm particles; at straight section of channels under (C) pure buffer flow and (D) RBC 25% flow for 2 μm particles. Binding densities are plotted for two different anti-ICAM-1 particle coating densities; 1199.2 and 272.2 anti-ICAM-1/μm². Error bars represent standard deviation for three independent flow cases each. _____ 46

Figure 10: Normalized particle binding density (#/mm²) for 210 nm (1257.1 anti-ICAM-1/μm²) and 2 μm (1199.2 anti-ICAM-1/μm²) particles are compared for (A) pure buffer flow case and (B) RBC 25% flow case at different shear rates; (C) Comparing ratio of particle binding density of RBC flow case to pure buffer flow case for 210 nm (1257.1 anti-ICAM-1/μm²) and 2 μm (1199.2 anti-ICAM-1/μm²) particles at different shear rates; _____ 49

Figure 11: Normalized particle binding density in parent channel and daughter channels a and b for the asymmetric flow case under RBC flow for (A) 210 nm particles at 1905.3 anti-ICAM-1/μm² and (B) 2 μm particles at 1199.2 anti-ICAM-1/μm². _____ 52

Figure 12: Attachment and detachment time history profile of normalized particle binding density data for 210 nm particles at shear rates (A) 200 s⁻¹ (B) 550 s⁻¹ (C) 900 s⁻¹ (D) 1250 s⁻¹ & (E) 1600 s⁻¹. All three anti-ICAM-1 particle densities of 1905.25, 1257.1 and 625.8 /μm² are studied. Dashed green line indicates the start of detachment period. Error bars represent standard deviation for three independent flow cases. _____ 53

Figure 13: Attachment and detachment time history profiles of normalized particle binding density for 2 μm particles at shear rates (A) 200 s⁻¹ (B) 550 s⁻¹ (C) 900 s⁻¹ (D) 1250 s⁻¹ & (E) 1600 s⁻¹. Both anti-ICAM-1 particle densities of 1199.2 and 272.2 / μm² are studied. Dashed green line indicates the start of detachment period. Error bars represent standard deviation for three independent flow cases. _____ 55

Figure 14: Particle attachment and detachment rates for 210 nm (A-B) and 2 μm particles (C-D), respectively. _____ 57

Figure 15: A, Graphical schematic (left) and photograph (center) of the bi-layer device showing the upper (marked with yellow lines) and lower (marked with red lines) channel separated by the semi-permeable membrane. Schematic on the extreme right depict endothelial cell growth on semi-permeable membrane and TNF-α treatment from the lower channel. B, (a) Bright field image of the top (marked with yellow lines) and bottom (marked with red lines) channel defining the upstream, TNF-α activated and downstream sections, (b) Fluorescence

labeled actin cytoskeleton (FITC phalloidin) images of confluent BAOEC layer aligned to flow (12 dyne/cm² FSS for 24 hrs). The cells grow on the semi-permeable membrane in the top channel of the device. Arrow shows flow direction (Scale bar: 100 μ m). 68

Figure 16: Organization of F-actin stress fibers (green) in BAOECs assessed by confocal microscopy (A) Static case; Cell stress fibers tend to align parallel to the width of the channel. (B) After 4 hrs of flow at 12 dyne/cm² FSS; Cell stress fibers tend to align parallel to the flow direction. Inserts show zoomed in images of stress fiber alignment. Arrow marks the flow direction. (C) Quantitative measurement of stress fiber alignment angle (α) to the width of the channel under static and flow shear stress case (* $p < 0.001$, ** $p < 0.0001$, *** $p < 0.00001$, by Student's t test). 71

Figure 17: Reorganization of cortical actin into stress fibers in BAOECs subjected to FSS. Flow-induced actin remodeling was observed by fluorescence labeling of the actin cytoskeleton with FITC-conjugated phalloidin in BAOECs treated with 12 dyne/cm² FSS for 4 hrs. Comparison of (A) Cortical actin thickness; (B) Stress fiber width; distribution in static and flow (12 dyne/cm² FSS for 4 hrs) culture conditions. (* $p < 0.001$, ** $p < 0.0001$, *** $p < 0.00001$, by Student's t test). 72

Figure 18: Comparison of stress fiber distribution in BAOECs subjected to FSS with no flow case. Actin stress fibers of BAOECs are labeled with FITC-conjugated phalloidin. (A), Fluorescence intensity (grayscale value) of stress fibers is quantified using ImageJ software across the marked line and corresponding line graphs are plotted for, (a,b) no flow (control) case; and (c,d) endothelial cells treated with 12 dyne/cm² FSS for 4 hrs. (B), (a) Total number of fluorescence intensity (grayscale value) peaks of stress fibers in control and flow case; (b) Thin and thick actin stress fibers were marked by classifying stress fibers based on grayscale value ≤ 50 as thin and > 50 as thick in the BAOECs for both control and FSS case. Arrow indicates flow direct. (Scale bar: 10 μ m). 73

Figure 19: Binding of Anti-ICAM-1/Control IgG coated 210 nm particles on BAOECs under flow. A, Fluorescence micrographs show binding of particles to TNF- α activated BAOECs under different conditions, (a) Anti-ICAM-1 coated particles with a density of $\sim 1900/\mu\text{m}^2$ (~ 230 molecules/particle) at FSS of 6 dyne/cm²; (b) Anti-ICAM-1 coated particles with a density of $\sim 1000/\mu\text{m}^2$ (~ 110 molecules/particle) at FSS of 6 dyne/cm²; (c) Control IgG coated particles at FSS of 6 dyne/cm². (Scale bar: 20 μ m). B, Quantification of anti-ICAM-1 and control

IgG coated particle binding per cell at FSS of 6 dyne/cm² on TNF- α activated BAOECs, (a) Anti-ICAM-1 coated particles with a density of $\sim 1900/\mu\text{m}^2$ (~ 230 molecules/particle) and Control IgG coated particles; (b) Anti-ICAM-1 coated particles with a density of $\sim 1000/\mu\text{m}^2$ (~ 110 molecules/particle) and Control IgG coated particles. (* $p < 0.001$, ** $p < 0.0001$, *** $p < 0.00001$, by Student's t test).

85

Figure 20: Binding of Anti-ICAM-1/Control IgG coated 210 nm particles on BAOECs cultured in a petri dish. A, Fluorescence micrographs show binding of particles to 2 hr TNF- α (10 U/ml) activated BAOECs, (a) Anti-ICAM-1 coated particles with a density 232.5 anti ICAM-1/particle; (b) Control IgG coated particles. (Scale bar: 20 μm). B, Quantification of anti-ICAM-1 and control IgG coated particle binding per cell on TNF- α activated and control BAOECs.

87

Binding of anti-ICAM-1 coated 210 nm particles (232.5 anti ICAM-1/particle) on BAOECs treated with TNF- α (10U/ml) from the basal and apical side of the cell, (A) Schematic illustrating the TNF- α treatment procedure; (B) Particle binding/cell quantification of anti-ICAM-1 coated 210 nm particles (232.5 anti ICAM-1/particle) on ICAM-1 expressing BAOECs. (n=100 cells from three independent experiment for each case)

88

Figure 22: Targeted binding of anti-ICAM-1 coated particles of different antibody coating density on BAOECs in the upstream, TNF- α treated and downstream sections of the channel at different shear rates. Quantification of particle binding density per cell at 6, 12 and 18 dyne/cm² for 210 nm particles with A, anti-ICAM-1 coating density of 232.5 ± 25 anti-ICAM-1/particle and B, anti-ICAM-1 coating density of 112.9 ± 19 anti-ICAM-1/particle. Data are shown as mean \pm S.D. (n=50 cells). $p < 0.01$ by one way ANOVA test for particle binding data compared between upstream, TNF- α treated and downstream regions for both 232.5 ± 25 and 112.9 ± 19 anti-ICAM-1/particle cases.

89

Figure 23: Analysis of particle binding and F-actin stress fiber arrangement along the length of the channel after TNF- α treatment. A, Particle binding per cell at 6 dyne/cm² FSS along the length of the channel divided into upstream, TNF- α treated and downstream sections. Data are shown as mean \pm S.D. B, F-actin stained image of BAOECs aligned to FSS at 12 dyne/cm² for 4 hrs and TNF- α treated for 2 hrs at 10 U/ml. Zoomed in images (corresponding to dashed boxes) give better understanding of F-actin arrangement. Yellow bordered image represents control BAOECs flow aligned to 12 dyne/cm² FSS. Dashed boxes and magnified images are arranged in the same order. Arrow indicates flow direction. (Scale bar: 100 μm).

93

Figure 24: Targeted binding of anti-ICAM-1 coated particles of 1 micron size on flow aligned BAOECs in the upstream, TNF- α treated and downstream sections of the channel at 1.5 dyne/cm². A, Fluorescence micrographs show binding of particles on TNF- α activated BAOECs. B, Quantification of particle binding density per area at 1.5 dyne/cm² for 1 μ m particles with anti-ICAM-1 coating density of \sim 1500/ μ m². _____ 95

Figure 25: (A) Illustration of the real time particle binding study system on live cells. 210 nm particle binding per cell data over time to characterize surface ICAM-1 expression by BAOECs. (B) Images of 210 nm (green fluorescence) particle binding over stained (red) cells for different time points; (C) Particle binding per cell data for BAOECs before and after TNF- α over time. _____ 97

Figure 26: Schematic describing transport of molecules through the cardiovascular and lymphatic system in normal tissue with basal blood vessel permeability and tumor or other inflammatory tissues with increased blood vessel permeability. _____ 102

Figure 27: *In vivo* (A,B & C) and *in vitro* (D & E) techniques to analyze vascular permeability. A, Tumor vessel (red) showing localized leaky spots (green) [182]; B, Fluorescent dye highlights intact blood vessel with basal permeability (Left). Tumor blood vessel with increased vascular permeability (Right)[183]; C, Normal mouse retina. Right image (Left). Abnormal blood vessel growth and permeability characteristic of diabetes and inflammatory signaling [184-186]; D, Commercial *in vitro* vascular permeability test platform based on transwell inserts [187]; E, Bi-directional transport studies using Caco-2 cells on transwell insert [188]. _____ 104

Figure 28: (A) Photograph of the bi-layer device showing the upper and lower channel separated by the semi-permeable membrane along with their inlets and outlets. The apical side of the endothelial cell layer face the upper channel are exposed to media flow. Thrombin and tracer molecule are added to media to study blood vessel permeability under acute inflammation. Tracer molecule diffusion to the lower channel is controlled by the extend of endothelial cell permeability under inflammation. The diffused data sample is collected from the lower channel. (B) Bright field image of the membrane with 1 μ m diameter pores at an average density of 1.5×10^7 /cm². (C) Schematic depiction of endothelial cell growth on semi-permeable membrane, thrombin treatment from upper channel and tracer molecule diffusion through intercellular gaps. (D) Fluorescence labelled actin cytoskeleton (FITC-phalloidin) images of confluent BAOEC layer aligned to flow (12 dyne/cm² FSS for 6 hrs) in the upper channel. Arrow shows flow direction (Scale bar: 100 μ m) _____ 114

Figure 29: Permeability of the tracer molecule through the endothelial cell layer in the biomimetic device. (A) Permeability of FITC dye through the endothelial cell layer when treated with thrombin at 1 U/ml compared to control case. (B) Permeability of FITC dextran 4kDa through the endothelial cell layer when treated with thrombin at 1 U/ml compared to control case. (C) Normalized comparison of FITC dye and FITC dextran 4 kDa permeability on the endothelial cell monolayer when treated with thrombin at 1 U/ml. FITC dye with a lower molecular weight has higher permeability compared to FITC dextran 4 kDa. Asterisks indicate values significantly different from control values ($p < 0.05$).

118

Figure 30: Permeability of tracer molecule through the endothelial cell layer in the transwell insert study. (A) Permeability of FITC dextran 4kDa through the endothelial cell layer when treated with thrombin at 1 U/ml compared to control case. (B) Normalized comparison of FITC dextran 4 kDa permeability on the endothelial cell monolayer in the biomimetic device and transwell insert case on thrombin treatment. Endothelial cell monolayer in the biomimetic device recovers its barrier integrity within about 60 min compared to about 80 min in the transwell insert case. Asterisks indicate values significantly different from control values ($p < 0.05$).

121

Figure 31: Thrombin induces F-actin remodeling on BAOECs cultured on a cover slip. (A) Control case not subjected to thrombin treatment. Note the tight intercellular contact and predominantly peripheral cortical actin staining; (B) 20 minutes of thrombin treatment at 1 U/ml appears to induce intercellular gap formation and marked increase in actin stress fiber formation. (C) 40 minutes of thrombin treatment at 1 U/ml increases intercellular gap formation and produces notable decrease in cell size possibly due to acto-myosin based cell contraction. (D) 60 minutes of thrombin treatment at 1 U/ml seems to reduce intercellular gaps. (E) 80 minutes of thrombin treatment at 1 U/ml has significantly reduced intercellular gaps and there is significant decrease in F-actin stress fiber presence. (F) 100 minutes of thrombin treatment at 1 U/ml produce cell characteristics comparable to control case. (Scale bar: 25 μm)

123

Figure 32: BAOECs cultured in the microfluidic biomimetic device are treated with thrombin along with flow which induces F-actin remodeling. (B) 20 minutes of thrombin treatment at 1 U/ml produce regions without F-actin stress fibers between cells which signify inter-cellular gap formation. (C) These gaps tends to reduce and bridge by increased cortical actin presence towards the cell periphery after 40 minutes of thrombin treatment. (D) There is steady presence of F-actin filaments on the cell monolayer after 60 minutes of thrombin treatment, signifying the decrease in inter-cellular gaps. (Scale bar: 25 μm)

124

Figure 33: Image of a microfluidic platform devised to co-culture endothelial cells and SMCs on the opposite sides of a membrane. (A) Culture of endothelial cells and SMCs on the opposite sides of a porous membrane; Brightfield micrograph of the upper channel (B) and of the lower channel (C); Calcein AM stained (D) BAOECs in upper channel and (E) BAOSMCs in lower channel.

136

ABSTRACT:

Endothelial cells form the inner lining of blood vessels and regulate key blood vessel functions including host defense reactions, vascular smooth muscle tone, angiogenesis, and tissue fluid homeostasis. The occurrence of a pathological condition can lead to inflammation, a protective and tightly regulated response involving host cells, blood vessels and proteins. This process is promoted by circulating cytokines and other chemical mediators such as tumor necrosis factor- α (TNF- α), interleukins, thrombin, a few examples. Inflammation can be acute or chronic in nature and is characterized by specific cell receptor expression patterns on the endothelial layer and an increase in endothelial cell-cell gaps. Upregulation of intercellular adhesion molecule-1 (ICAM-1) on endothelial surface occurs during inflammation, and ICAM-1 plays an important role in leukocyte adhesion and recruitment. Understanding the dynamic nature of receptor expression and endothelial cell gap formation during inflammation would provide fundamental physiological information and is also essential for evaluating drug and other biomolecules targeted binding and uptake by endothelial cells.

The far reaching accessibility combined with heterogenic behaviour make microvascular endothelium an attractive target for targeted drug delivery. Dynamic and complex processes governing the targeted drug particle binding and distribution on blood microvasculature are still partially understood. Part of this work focuses on the characterization of particle delivery in microcirculation on an ICAM-1 coating based blood vessel mimicking microfluidic device. In microvasculature the vessel size is comparable to that of red blood cells (RBCs)

and the existence of blood cells largely influences the dispersion and binding distribution of drug loaded particles. Various factors that influence particle distribution and delivery such as the vessel geometry, shear rate, blood cells, particle size, particle antibody density were considered in this study.

Better understanding of the pathologically challenged local endothelial cell layer microenvironment can help us engineer drug carriers decorated with specific biomolecules which can improve the pharmacokinetics and pharmacodynamics of drugs. In this study we also developed a biomimetic blood vessel model by culturing confluent, flow aligned, Endothelial cells in a microfluidic platform, capable of being treated with inflammatory mediators locally. Primary bovine aortic endothelial cells (BAOECs) were grown on semi-permeable membrane with pores that separates an upper and lower channel made of polydimethylsiloxane (PDMS). This dual channel design allowed localized direct TNF- α treatment on the endothelial cell layer leading to expression of surface ICAM-1. This model simulated spatially controlled healthy and pathologically challenged endothelial cells in the same channel and thus has the ability to investigate the microenvironment of locally activated endothelial cells. We characterized endothelial cell culture in this platform and performed real-time *in situ* characterization of localized pro-inflammatory endothelial activation. Anti-ICAM-1 coated particles (210 nm and 1 μ m diameter) of different antibody coating densities were used as imaging probes and availability of ICAM-1 was probed. This allowed the investigation of spatial resolution and accessibility of ICAM-1 molecules on endothelial cells for targeted binding studies. Anti-ICAM-1 coated particles

specifically bound to TNF- α activated BAOECs in an antibody coating density, FSS and particle size dependent manner. F-actin remodelling was also observed in TNF- α treated and downstream sections of the channel. This work has developed a more realistic *in vitro* vascular model that can independently integrate various factors to effectively mimic a complex physiological endothelial cell microenvironment and has been applied to study endothelial cell microenvironment under localized inflammatory triggering.

Inflammatory responses in endothelial cells are characterized by an increase in vascular permeability by formation of intercellular gaps. The biomimetic blood vessel model developed by culturing confluent, flow aligned, and endothelial cells in a microfluidic platform (described prior) was utilized in characterizing the dynamic nature of vascular permeability under inflammation. BAOECs were subjected to *in vivo* levels of prolonged flow and then treated with thrombin, a serine protease. Thrombin induced profound increase of endothelial cell monolayer permeability in a rapid and reversible way. Endothelial cells cultured in the upper channel were exposed to media mixed with thrombin and a tracer molecule. Tracer molecule samples were collected real time and analysed using spectroscopy, and the dynamic nature of the process was studied. The remodelling of F-actin in BAOECs after thrombin treatment was also characterized for different time points. Better understanding of the dynamics involved in increased vascular permeability can help engineer strategies to enhance targeted drug delivery through these para-cellular gaps.

Chapter 1

Introduction

Endothelial cells form the inner lining or 'tunica intima' of blood vessels and are exposed to dynamically varying factors like hemodynamic conditions (shear stress, laminar, turbulent flow), biochemical signals (cytokines) and interaction with other cell types (smooth muscle cells, monocytes, platelets etc). Blood vessel functions are regulated by an interaction between these factors. They form an interface between circulating blood in the lumen and the tissue layer beyond the vessel wall. Thus they form a barrier, and a potential target for localized, enhanced and effective targeted drug delivery. Endothelial cells express specific cell-surface molecules under various pathological conditions, which are absent or barely present on healthy and normal blood vessels [1]. Targeting these epitopes on the endothelial cell surface by coupling these potential endothelial cell surface markers with carefully engineered drug carriers (considering features such as valence and surface density of ligands, the carrier geometry and encapsulation into protective polymeric carriers) effective and active vascular-targeted drug delivery systems can be achieved. These systems will be capable of avoiding toxicity based drug side effects and thus acceptable in a clinical domain.

Delivery systems in the form of liposomes, dendrimers, micelles and polymers, as well as the more conventional and inorganic carbon, silica, iron and gold based platforms are widely used as drug carriers [2-5]. The size of the carrier plays a pivotal role in ligand-receptor based molecular recognition and binding to cell

surface (a larger particle would be less efficient in targeting receptors closer to cell plasmalemma). The uptake efficacy of nanoparticle (NP) based drug carriers is higher compared to their larger micron scale counterparts, which are easily cleared off by the human mononuclear phagocyte system [6]. Pathological studies of conditions like inflammation, atherosclerosis and cancer have observed accumulation of NP based drug therapies based on increased permeability of blood vessels in the disease region [7-11]. Various techniques in targeted drug delivery have been developed in recent years to reduce side effects, toxicity, and drug dosage [12]. Dynamic and complex processes governing the targeted drug particle binding and distribution on endothelial cell surface are still only partially understood.

Targeted binding of drug carriers should occur specifically on endothelial cells of blood vessels in the pathologically challenged region for maximum efficacy and to prevent drug toxicity related side-effects. The complex inflammatory cellular mechanisms contributing to upregulation of adhesion molecules on endothelial cell surface that can act as drug targets have proved elusive. A better understanding of the dynamic nature of the pathological process and the contribution of various heterogeneous factors towards the cellular mechanisms governing these processes would help us develop therapeutic strategies that can have enhanced impact.

Scientists have employed *in vivo* and *in vitro* platforms to shed more light on blood vessel physiology. *In vivo* studies often require complex mammalian models and time-consuming surgical protocols, making them expensive and challenging

platforms. They also raise ethical issues and such models also respond differently than to humans as interspecies predictability is low in response to drugs and diseases [13]. *In vivo* studies also allow only limited control of the heterogeneous physical, chemical, and biological parameters influencing the blood vessel and present challenges with respect to imaging as well [14]. Relatively easier and simple *in vitro* platforms are also under use, but endothelial cells tend to lose their native phenotype in these conditions. This demands an alternative, practical, human-centered and bio-mimetic blood vessel mimicking platform that can provide culture conditions for endothelial cells that are comparable to the 3D native *in vivo* endothelium. This might also help sustain the endothelial cell phenotype closer to its native state while being cultured *in vitro*. Such a platform should maintain the quiescent phenotype of endothelial cells under normal conditions by down-regulating the pro-inflammatory and proliferative pathways of vascular endothelial cells. A blood vessel model can achieve this by subjecting the endothelial cells to native *in vivo* conditions, like constantly renewing essential biomolecule supply, flow conditions, constant removal of waste and undesirable molecules, etc. [15-16]. Such a biomimetic model can simulate disease related inflammatory conditions when triggered in a close to *in vivo* manner, and we can apply such a system to study the dynamics of endothelial cell microenvironments.

The two main objectives of this work are, **1)** understand the optimal drug carrier properties for targeted delivery in specific microvascular geometries and hemodynamic conditions for drug carrier transport and binding on endothelial cells in the blood stream; and **2)** study the dynamic and heterogeneous nature of

receptor upregulation and intercellular gap formation in a blood vessel microenvironment under inflammatory conditions.

These objectives have been accomplished through the completion of the following aims:

Aim 1: Develop a microfluidic blood vessel model mimicking a microvasculature blood vessel environment in an inflammatory state by specific cell receptor protein coating.

Aim 2: Apply this platform towards characterizing targeted particle binding and distribution, considering various factors like blood vessel geometry, flow shear rate, effect of blood cell flow and drug carrier features like size, shape and ligand coating (affinity and coating density).

The receptor-targeted delivery system designed to quantitatively assess multivalent nanoparticle adhesion under physiological shear flow conditions allows optimization of carrier adhesion for maximizing the binding efficiency. ICAM-1 has been directly associated with pathological conditions like atherosclerosis, autoimmune disorder, transplant rejection, and cancer. We apply ICAM-1 protein coating on a microfluidic platform at a density expressed *in vivo* by pathologically challenged endothelium. Polystyrene particles of 210 nm and 2 μ m diameter coated with monoclonal antibody specific for ICAM-1 are used as model delivery carriers. This study provides a mechanical understanding of drug carrier transport and binding in microvessels. The tool also defines parameters for optimal drug

dosage and targeting in specific vascular geometries and hemodynamic conditions.

Aim 3: Engineer an alternative, human-centered, bio-mimetic blood vessel mimicking platform by growing endothelial cells in culture conditions close to their native *in vivo* environment. This platform can mimic localized disease conditions by spatially controlled pro-inflammatory stimulation of endothelial cells.

Aim 4: Apply this platform to investigate the microenvironment of locally activated endothelial cells by studying the dynamic nature of cell receptor upregulation and increase in vessel permeability under inflammation.

This model integrates a confluent, flow aligned cell layer in a microfluidic platform and is designed to allow the culture of endothelial cells expressing quiescent and inflammatory response in the same channel. This investigation of endothelial cell microenvironment during both these states in the same channel brings to light the nature of transition between the two states. We studied the localized dynamics of ICAM-1 protein expression on the surface of endothelial cells using imaging probes and their related cytoskeletal remodelling under inflammation in this work. By tuning the design and assay protocol it was also possible to use the same microfluidic blood vessel model to study the increase in blood vessel permeability under inflammation. Endothelial cells were treated with thrombin, an acute inflammatory mediator and the increase in vessel permeability was characterised by studying diffusion of tracer molecules. Applying this biomimetic platform towards targeted nanodrug delivery and trans-endothelial migration studies allows

the understanding on cellular level chemistry and mechanics involved in drug carrier binding and uptake by endothelial cells.

Chapter 2

Background and Significance

Blood vessels extend throughout the body and mediate gas exchange, nutrient and waste transport, and immune defense [15]. An endothelial cell monolayer forms the inner layer and is in constant contact with blood flow. This cell layer contributes a basement membrane composed of fibronectin, collagen IV, laminins, and heparan sulfate proteoglycans, which directly or indirectly influences diverse blood vessel processes such as cell differentiation, attachment, migration, polarization, guidance, and survival [16]. Vascular smooth muscle cells or pericytes cover the endothelial cells and form the middle layer, depending on the blood vessel size and position. Arteries are supported by smooth muscle cells thereby regulating the vessel tone, whereas capillaries are sparsely supported by specialized mesenchymal cells denoted as pericytes. The fibroblasts and matrix form the outer layer of the blood vessels. The different layers of a blood vessel are detailed in Figure 1 along with their functions.

The endothelial cell layer or tunica intima of the blood vessel forms an interface between circulating blood in the lumen and the tissue layer beyond the vessel wall. This layer regulates multiple functions including host defense reactions, vascular smooth muscle tone, angiogenesis, and tissue fluid homeostasis. The endothelial cell layer does play a part in regulating these processes by secreting specific cell signalling factors. For example, urokinase and tissue-type plasminogen activators are secreted by endothelial cell to dissolve blood clots through the generation of

the fibrin-degrading protease and plasmin. Similarly blood vessel tone is controlled by nitric oxide, prostacyclin, and additional factors, and endothelial factors are also able to suppress platelet aggregation as antithrombotic factors. A failure by the blood vessel endothelial cells to perform their physiologic functions is referred to as endothelial dysfunction or endothelial activation. This is often a maladaptive response to a pathological stimuli. Endothelial cells secrete a variety of agents including cytokines, reactive oxygen species, growth factors, and a variety of chemoattractants during thrombosis or other pathological conditions that are associated with the inflammation process. Endothelial dysfunction is characterized by upregulated expression of cellular adhesion molecules, compromised barrier integrity (leading to increased leukocyte recruiting), increased vascular smooth muscle tone [secondary to impaired processing of vasodilators (nitric oxide and prostacyclin) as well as increased production of vasoconstrictors including endothelin], and reduced resistance to thrombosis as phenotypic features [17-19].

In developed countries cardiovascular diseases form the primary reason for mortality and morbidity. A report in 2012 by the American Heart Association found that in 2008 an average of one death occurred every 39 seconds due to cardiovascular diseases, accounting to more than 2200 American deaths each day. Annual report by the American Cancer Society estimated 1,658,370 new cancer cases diagnosed and 589,430 cancer deaths in the US during the year of 2015 [20]. Pathogenesis of a broad spectrum of human diseases is marked by alterations of endothelial cells and the vasculature. The endothelium is directly involved in stroke, diabetes, insulin resistance, chronic kidney failure, tumor

growth, metastasis, venous thrombosis, and severe viral infectious diseases, along with cardiovascular diseases (restenosis, atherosclerosis, hypertension, ischemia), neurological disorders (stroke, Alzheimer's disease) and other systemic inflammatory diseases (rheumatoid arthritis, inflammatory bowel diseases, lupus, psoriasis, spondyloarthritis) [17, 21-26]. Therefore the dysfunction of the vascular endothelium can be considered a mark of human diseases.

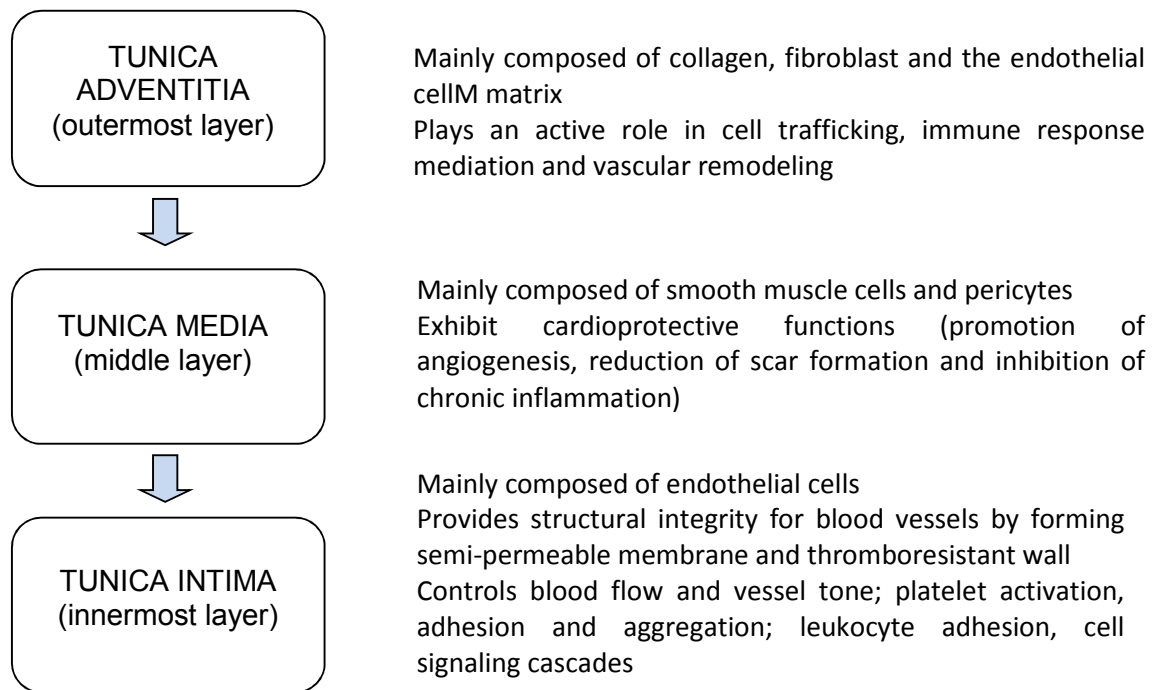


Figure 1: Layers of the blood vessel. Outer tunica adventitia, middle tunica media, and inner tunica intima, their corresponding cell composition and functions.

Blood vessels are an intricate network and have accessibility throughout the body. The human vascular system possesses unique physiological features that can be exploited for enhanced and effective targeted drug delivery. Many human vascular diseases are exquisitely restricted to specific types of vessels. For example, the part played by platelets in the initiation of arterial and venous thrombosis differs,

as does the level of risk these two types of blood vessels are exposed to in atherosclerosis. It is also common for vasculitis to show preference for specific arteries, veins, or capillaries or for certain organs. Tumor cells may show similar predilection in metastasizing via specific vascular beds [27]. The thin layer of endothelial cell lining the interior surface of blood vessels has the accessibility and uniqueness to be a potential target for localized, enhanced and effective targeted drug delivery. Endothelial cells express specific cell-surface molecules under various pathological conditions, which are absent or barely present on healthy and normal blood vessels [1]. By coupling potential endothelial cell surface markers with carefully engineered drug carriers (considering features such as valence and surface density of ligands, the carrier geometry and encapsulation into protective polymeric carriers), effective and active vascular-targeted drug delivery systems can be achieved, avoiding side effects and acceptable in a clinical domain [28].

The vascular networks in healthy and disease state also differ in their morphological characteristics other than the molecular receptors expressed. The pathology of several inflammation related conditions (atherosclerosis, ischemia reperfusion injury, stroke, hypertension and also thrombosis, diabetes, acute lung injury, and sepsis, etc.) are characterized by endothelial cell layers with intercellular gaps that form pores, making them leaky. Physiological and pathological conditions of inflammatory diseases bring about this increased permeability in vasculature [19]. The same mechanism has been found to enhance drug carrier delivery to vascularized solid tumors via a phenomena termed enhanced permeation and retention effect [29-30]. The increase in permeability of

the vascular network in pathologically challenged regions can be used to potentially increase the delivery of therapeutic agents to the site of infection. This change in morphological characteristics of the endothelium can be combined with the marked increase in expression of specific cell receptors to facilitate enhanced targeted drug delivery.

Strict regulations are in effect for drug development and testing. Conventional animal experimental models to evaluate drug delivery systems raise ethical issues and such models also respond different than humans as interspecies predictability is low in response to drugs and diseases [13]. *In vivo* studies also allow only limited control of the heterogeneous physical, chemical, and biological parameters influencing the blood vessel and present challenges with respect to imaging as well [14]. This demands a practical, human-centered and bio-mimetic alternative testing platform, which can provide pharmaceutical research greater security and shorten the path to new drugs and delivery systems. By applying the principles of engineering and biology, novel *in vitro* biological substitutes to test drug delivery systems can be developed. Creating a bio-hybrid artificial blood vessel by incorporating tissue specific endothelial cells and studying endothelial cell microenvironment for specific disease foci holds huge potential.

2.1 Blood vessel; its structure and function

Blood vessels are intricate networks of hollow tubes that transport blood throughout the entire body. This is an essential function as blood delivers valuable nutrients and removes wastes from our cells. Blood vessels are constructed of layers of connective tissue and muscle. The inner blood vessel layer is formed of

endothelium. In capillaries and sinusoids, the endothelium comprises the majority of the vessel. Blood vessel endothelium is continuous with the inner tissue lining of organs such as the brain, lungs, skin, and heart.

2.1.1 Types of Blood Vessels

Arteries

Arteries are elastic vessels that transport blood away from the heart. Pulmonary arteries carry blood from the heart to the lungs where oxygen is picked up by red blood cells. Systemic arteries deliver blood to the rest of the body.

Veins

Veins are elastic vessels that transport blood to the heart. Veins can be categorized into four main types: pulmonary, systemic, superficial, and deep veins.

Capillaries

Capillaries are extremely small vessels located within the tissues of the body that transport blood from the arteries to the veins. Fluid exchange between capillaries and body tissues takes place at capillary beds.

Sinusoids

Sinusoids are extremely small vessels located within the liver, spleen, and bone marrow.

Blood is circulated through the body via the cardiovascular system. This system is comprised of the heart and the circulatory system. Blood vessels carry blood from the heart to all areas of the body. The blood travels from the heart via arteries to smaller arterioles, then to capillaries or sinusoids, then to venules, to veins, and back to the heart. Microcirculation deals with the flow of blood from arterioles to

capillaries or sinusoids to venules. As blood moves through the capillaries, substances such as oxygen, carbon dioxide, nutrients, and wastes are exchanged between the blood and the fluid that surrounds cells. Regions of blood vessel with the microcirculation play a critical role in targeted drug delivery as these regions have accessibility all throughout the body facilitating transport for drug carriers to site of delivery.

The endothelial cell layer exhibits both morphological and molecular heterogeneity among and within tissues. Capillary endothelium expresses variation in arrangement for different vascular sites and it is recognized based on differences in function. The capillary endothelium in brain and retina is lined by continuous endothelial cells connected by tight junctions. This helps to maintain the blood-brain barrier, an essential physiological feature. The liver, spleen, and bone marrow sinusoids have a discontinuous endothelial cell lining that allows cellular trafficking between intercellular gaps. Meanwhile, fenestrated endothelial cells are present in intestinal villi, endocrine glands, and kidneys to allow selective permeability essential for efficient absorption, secretion, and filtering [31]. The phenotype and protein expression on endothelial cells from diverse tissues are also heterogeneous. For example, von Willebrand factor (a common endothelial cell marker) is not uniformly expressed on all types of vessels [32]. Also, only 3% of vascular endothelial cells express tissue type plasminogen activator *in vivo* and a constant and active expression of urokinase-type PA is confined only to renal endothelial cells [33-34]. The expression of specific cell signaling molecules after exposure to cytokines or endotoxin is also restricted to specific vessels

[35], among other examples of multiple cases of heterogeneity at the level of protein expression. These heterogeneities in protein expression and endothelial cell arrangement pattern can be utilized in designing drug delivery systems that are locked for specific endothelial cell location, and morphological or molecular expression state.

2.2 Targeted Drug delivery

Recently there has been a vast increase in the number of drug carrier systems which have been explored or already approved for use in the clinic and producing a significant impact on the diagnosis, treatment, and potential cure of many chronic diseases, including cancer, diabetes mellitus, psoriasis, Parkinson disease, Alzheimer disease, rheumatoid arthritis, HIV infection, infectious diseases, cardiovascular disorders, asthma, and drug addiction [19]. But most of the pharmaceutical systems do not work based on the ability of the drug agent to accumulate selectively and specifically in the pathological organ, tissue, or cell. These drug agents are distributed within the human body and non-specifically target the pathological situation. This leads to a situation where the drug has to cross various biological barriers, like other organs, cells, and intracellular compartments. These steps can inactivate or express undesirable and non-specific reactions on organs and tissues that are not involved in the pathological process. Specific targeting of drugs to the target organ will allow higher tissue selectivity and local concentration. This also limits the level of drugs in non-targeted cells and organs below toxic levels and without side effects to the host.

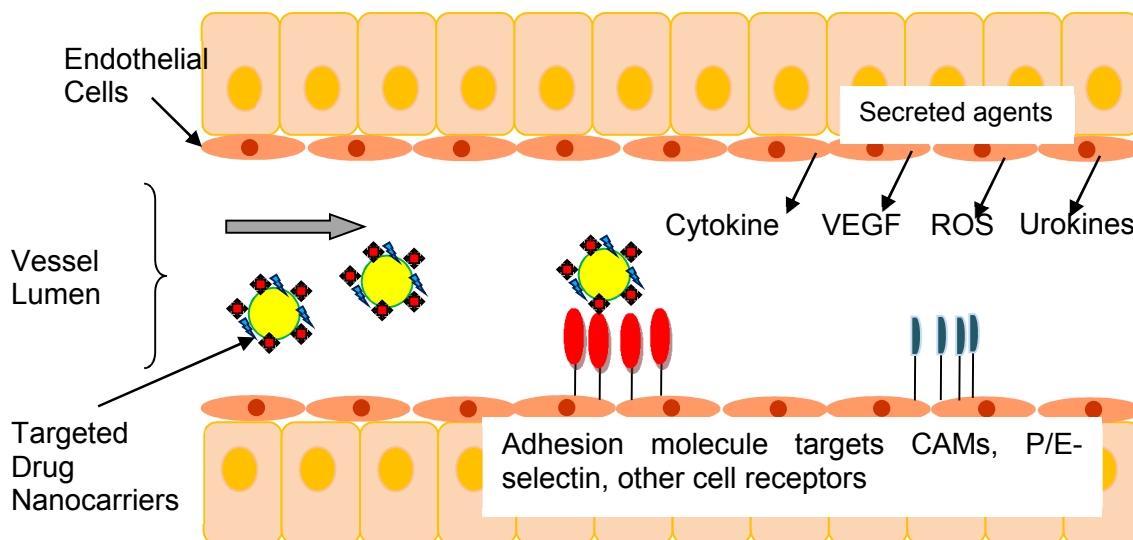


Figure 2: Schematics of the vasculature endothelium and selected molecular determinants that play a pivotal role in targeted drug delivery to the endothelium. Surface-modified drug carriers decorated with specific antibodies, peptides, or small molecules were shown to accumulate in the endothelium.

A drug carrier targeted to the vasculature should specifically bind to the intended endothelial cell layer expressing the specific molecules/features of pathological condition while withstanding the hydrodynamic forces of blood flow. Various clinical disorders over-express specific cell surface antigens and molecules on the endothelial cell layer as a response to altered physiological conditions and this can be exploited to achieve active vascular targeting of drug carrier systems [19]. Various techniques in targeted drug delivery have been developed in recent years to reduce side effects, toxicity, and drug dosage [12]. The use of drug carriers instead of drug molecules produces high affinity binding and enhanced vascular immuno-targeting at disease regions [36-38].

2.3 Drug carrier properties

Various techniques in targeted drug delivery have been developed in recent years to reduce side effects, toxicity, and drug dosage [12]. The use of particles as drug

carrier help in targeted delivery and release of drugs at diseased region, serving the dual role of diagnosis and therapy [36-37]. Specificity in targeting is introduced by applying ligand-receptor chemistry. Particles are coated with ligands and the efficacy of targeted drug delivery depends on various factors like size and shape of the drug carrier, its affinity and accessibility to cell surface receptor, ligand coating density, and multivalent or monovalent ligand configuration and its arrangement, among others.

The size of the carrier plays a pivot role in ligand-receptor based molecular recognition and binding to cell surface (a larger particle would be less efficient in targeting receptors closer to cell plasmalemma). The uptake efficacy of nanoparticle (NP) based drug carriers is higher compared to their larger micron scale counterparts, which are easily cleared off by the human mononuclear phagocyte system [6]. This also increases the bioavailability of these drugs. NPs also have larger surface to volume ratio[39], which enhances their targeting capabilities while carrying lower drug dosages. Pathological studies of conditions like inflammation, atherosclerosis and cancer have observed accumulation of NP based drug therapies based on increased permeability of blood vessels in the disease region [7-11]. This phenomenon should be studied in detail to exploit the chance of achieving improved drug therapy success and clinical application.

2.4 Specificity in drug carrier targeting

Specific and nonspecific interactions can occur at the cell/particle interface when targeting a carrier to the endothelial cell layer. The specific interactions are controlled by the formation and breakage of molecular bonds among receptor

molecules expressed at the cell membrane and ligand molecules distributed over the carrier surface. Nonspecific interactions are balanced between the attractive and repulsive short-range forces including van der Waals, electrostatic, and steric forces. This becomes significant and to be considered when the particle is in close proximity to the vessel walls.

A large variety of molecular determinants on the endothelial cell surface are available to be utilized for effective targeted drug delivery to the endothelium, as shown in Figure 2. Inflammation and other different clinical conditions can lead to diverse molecular cascade profiles by endothelial cells and this may lead to overexpression of different target receptors. Endothelial cell adhesion molecules (CAMs) are attractive candidates for targeted delivery and this family of molecules includes, vascular adhesion molecule-1 (VCAM-1), intracellular adhesion molecule-1 (ICAM-1), platelet-endothelial adhesion molecule-1 (Pendothelial cellAM-1) and P/E selectin. CAM molecules serve as targets for both diagnosis and treatment of vascular inflammatory signaling cascades [40]. Tumor cells produce pro-angiogenic cytokines, such as vascular endothelial growth factor, basic fibroblast growth factor, transforming growth factor b, and different interleukins which make tumor blood vessels highly proliferative [41]. This pro-angiogenic state leads to the expression of prior mentioned surface antigens on the endothelial cells, which are not expressed by normal endothelium. Thus these antigens form good candidates for targeted vascular drug delivery. Integrin proteins which are over-expressed in angiogenic tumor endothelial cells and malignant tumor cells also are potential target endothelial cell receptors for drug

delivery.

Intercellular Adhesion Molecule-1 (ICAM-1) expressed on the surface of endothelial cells is accepted as a safe, relevant and accessible receptor for targeted drug delivery [1]. ICAM-1, a cell-surface glycoprotein member of the Ig super-family, is expressed basally on normal vascular endothelium. Under inflammatory conditions, interaction between endothelial cells and blood constituents occurs by the up-regulation of intercellular adhesion molecules such as ICAM-1 on the surface of endothelial cells and leukocytes [42-43]. This mediates the targeted migration of leukocytes into specific areas of inflammation [44]. Various ICAM-1 based therapeutic agents for cancer immunotherapy and other modes of treatment are used nowadays [45-46]. This mediates the targeted migration of leukocytes into specific areas of inflammation [44]. ICAM-1 is considered a versatile anchor for targeted drug delivery and various therapeutic agents are applied nowadays in the context of oxidative stress, inflammation, and thrombosis as well as for cancer immunotherapy and other modes of treatment [1, 45-46]. Our biomimetic vascular model applies endothelial cell surface ICAM-1 molecules for targeting drug carriers. ICAM-1 antibody coated particles acts as model drug carriers based on ICAM-1:anti-ICAM-1 binding affinity.

2.5 Influence of vessel geometry in drug carrier distribution

The human circulatory system consists of large blood vessels such as arteries and veins (~15-0.5 mm), and smaller vessels such as arterioles, venules (100-500 μm) and capillaries (~10 μm). The distribution of drug particles in a real vascular network having a hierarchical geometry will depend on local shear rate, flow

velocity, pressure and volume [47]. Our study considers the distribution of nano and micron sized particles in a branching channel that mimics the geometry and flow conditions of a dividing microvascular network. Microvasculature refers to part of the circulatory system consisting of capillaries, arterioles, and venules [48]. Microvasculature parameters such as vascular geometry, target-receptor expression levels and flow shear rate must be considered while performing *in vitro* tests.

2.6 Distribution of drug carriers under the influence of RBC

Drug carriers interact with blood *in vivo*, a complex bio-fluid consisting of RBCs, monocytes, platelets, proteins etc. Blood flow in microvasculature is a two-phase flow as the vessel diameter becomes comparable to the size of RBCs. *In vitro* studies on RBC mediated particle delivery have to consider various *in vivo* microvasculature parameters, such as Fåhræus–Lindqvist effect [49], Segre–Silberberg effect [50-51], CFL formation [52-54], vessel geometry/bifurcations [55] and blunt velocity profile [56-59]. RBCs have a biconcave shape of $\sim 8 \mu\text{m}$ diameter and $\sim 2 \mu\text{m}$ thickness, and are highly deformable [54, 60]. The flexible RBCs migrate radially towards the center region in microvessels based on various hemorheology factors such as shear rate, viscosity, hematocrit concentration, RBC aggregation and deformability. This results in a RBC concentrated core region and a cell-free plasma layer near the vascular wall called CFL [52, 60-61]. Particles flowing along with RBCs can diffuse towards these CFL and this will influence their distribution and binding dynamics across a channel [62-64].

2.7 Current challenges in the study of drug delivery and distribution

Theoretical modelling studies on drug delivery usually have limited predictive capability beyond the parameters used to create the model [65]. Due to bioethical regulations and complex physiological conditions, it is challenging to quantify the particle delivery process using *in vivo* animal models [66-67]. Most of the current *in vitro* studies are carried out in flow chambers or channels [68-69], but these platforms lack the flexibility to study the effects of branching vascular geometry and varying vessel diameter on drug delivery. They also require significant sample volumes making it an expensive platform. Targeted drug delivery systems hold promise for innovative medical treatment for various pathological conditions. Strict regulations are in effect for drug development and testing. Conventional animal experimental models to evaluate drug delivery systems raise ethical issues and such models also respond different to humans as interspecies predictability is low in response to drugs and diseases [13]. *In vivo* studies also allow only limited control of the heterogeneous physical, chemical, and biological parameters influencing the blood vessel and present challenges with respect to imaging as well [14]. This demands a practical, human-centered and bio-mimetic alternative testing platform, which can provide pharmaceutical research greater security and shorten the path to new drugs and delivery systems.

2.8 Microfluidics

An *in vitro* bio-mimetic blood vessel should be able to model *in vivo* physiological characteristics like localized pathology microenvironment, relevant flow dynamics and vessel shape dimensions. Microfluidic engineering enables integration of

precisely controlled flow in channels, whose shape and dimensions can be designed to requirement with resolution limits in the micron scale. Microfluidic devices made of PDMS are used in this work. They have added advantages like rapid prototyping, optical transparency (for effortless imaging), ease of surface modification (through protein coating), biocompatibility and ease of integration, which facilitates multiplexing and high-throughput analysis [70], along with other features like smaller device footprint and reduced reagent volumes. Microfluidics have been applied for the past three decades for the development of DNA chips, lab-on-a-chip technology, micro-propulsion, and micro-thermal technologies. At this size scale faster diffusive mixing of liquids leads to rapid, accurate and highly repeatable reactions. These features highlight the potential of microfluidic platforms in studying targeted drug particle delivery on a blood vessel mimicking model.

2.9 Biomimetic platforms

By engineering the right structure and function of biological systems in a device, for example; one that contain human cells and mimics the blood vessels and tissues of living organs, a new suite of devices is emerging. These are the biomimetic organ-on-a-chip platforms. These complex, three-dimensional models of human organs are fabricated by relevant principles to design materials and devices that transform medical treatment, from the diagnosis of a disease to the discovery and delivery of appropriate drugs. In order to more accurately and realistically mimic various kinds of *in vivo* tissues in an *in vitro* set-up, great effort has also been made to imitate fine-structure and natural microenvironment of *in*

vivo tissues. This has led to better physiologically relevant tissue engineering and thus precise reappearance of physiological events and disease patterns *in vitro* [71-72]. Experimentation at the interfaces of biology, engineering and medical sciences is critical for this. These platforms have begun to revolutionize the way drug testing and disease treatments are being performed now. Traditional cell cultures in petri dishes and animal models are used to understand how a human body may react to a drug, toxin, or disease. Animal models often fail due to a variety of reasons explained previously, costing the pharmaceutical industry billions of dollars and years of time. Research that intends to create more realistic *in vitro* living tissue or organ models by accurately mimicking human host responses may accelerate the drug screening process with the hopes of fast-tracking new and potentially life-saving treatments to commercial deployment. Successful implementation of this research is anticipated to shorten drug development times and lower costs, benefiting both pharmaceutical companies and patients.

It is a true integration of biology and engineering that makes it possible to design “biomimetic” environments that subject the cell to a combination of factors known to guide tissue development and help maintain the right phenotype. Novel bioengineered culture platforms can provide tight environmental control along with the physiological transport and signaling, and thereby enable study of development, regeneration, and disease under conditions that predict the human *in vivo* context. In this study we developed an endothelial cell coated blood vessel biomimetic model. It has an upper and lower channel separated by a semi-

permeable, porous, cell culture friendly membrane. Specific endothelial cells can be grown on the membrane, which can be cultured under *in vivo* levels of flow and precisely controlled supply of essential biomolecules and external cues. The channels are designed such that a section of the upper channel can be accessed from the lower channel through the semi-permeable membrane. This facilitates an access to the blood vessel model from the lumen (inside the blood vessel) side and the ablumen (from the tissue) side, to provide physiologically relevant external cues in a spatially controlled localized way. This platform provides us the ability to draw physiologically relevant biological conclusions.

Chapter 3

Model 1: endothelial cell receptor protein (ICAM-1) coated microvasculature mimicking platform

3.1 Introduction

This section studies the binding distribution of anti-ICAM-1 coated particles on an ICAM-1 protein coated microfluidic device. Various factors like, vessel geometries (straight and branched channels), flow shear rates ($200-1600 \text{ s}^{-1}$), particle flow along with RBCs, particle size (210 nm and 2 μm), and particle ligand coating density, that influence particle binding distribution are analyzed. Around 10% higher particle binding density is observed at bifurcation regions of the mimetic microvasculature geometry compared to straight regions. Particle binding density is found to decrease with increased shear rates. RBCs enhance particle binding for both 210 nm and 2 μm . The particle binding density increases about 2-3 times and 6-10 times when flowing in whole blood at 25% RBC concentration compared to the pure particle case, for 210 nm and 2 μm particles respectively. With RBCs, the binding enhancement is more significant for 2 μm particles than that for 210 nm particles, which indicates an enhanced size dependent exclusion of 2 μm particles from the channel center to the CFL. Increased particle antibody coating density leads to higher particle binding density for both 210 nm and 2 μm particles.

3.2 Methods

3.2.1 Fabrication of microfluidic device

The required microfluidic design is photo-lithographically patterned on a silicon wafer using SU-8 2050 photoresist. Microfluidic devices are fabricated using Sylgard 184 PDMS. PDMS base is mixed with its cure at 1:10 (v/v) ratio following the basic techniques in soft lithography [35]. The PDMS mixture is poured on the silicon wafer, which acts as the master template. The hard PDMS layer is peeled out after baking and the features are inspected. The microfluidic device is made by binding the PDMS pattern on a clean glass slide after exposing them to oxygen (O₂) plasma. The flow channels are 100 µm wide and 100 µm in height. Both straight and bifurcating features are included in the design. The bifurcating channels have a branching angle of 60°.

3.2.2 ICAM-1 functionalized PDMS substrate

PDMS devices were coated with ICAM-1 as previously reported[10]. After binding with glass the PDMS microfluidic devices were silanized with 3-aminopropyltrimethoxysilane to improve protein adsorption. After washing the device with an adsorption buffer (0.1M NaHCO₃, pH 9.2), the devices were incubated for 2 hrs at room temperature with saturating concentration of protein G in adsorption buffer (100 µg/ml). ICAM-1 Fc chimera protein solution in PBS (100 nM) was introduced after washing the substrates three times with PBS to remove any excess protein G. The devices were incubated with ICAM-1 for 1 hr at room

temperature. The microfluidic chips were purged with 1% BSA containing 0.05% Tween20 one hour prior to testing.

3.2.3 Substrate ICAM-1 density characterization

In order to quantify the ICAM-1 protein density on the PDMS surface, ELISA was performed using an HRP-conjugated anti mouse IgG1 antibody. ELISA reaction was carried out in a 12-well plate and PDMS coated 22 mm circular glasses were used. The technique for substrate ICAM-1 characterization was performed as reported in literature [10].

Silicone isolators (Grace Bio Labs) were used to assure that the same volume of reagents were applied on PDMS coated glass as in the microfluidic device, to maintain the same surface area to volume ratio. Once the PDMS coated cover slips were coated with ICAM-1 Fc protein, they were blocked before silicone isolators were removed. This was followed by incubation with mouse anti-ICAM-1 at 2 µg/ml for 1 hr at 4 °C, and incubation with HRP-conjugated mouse antibody (1:1000 dilution). Each step was followed by washing with ice cold PBS. After the final wash step, the cover slips were placed in the well plate. Amplex Ultra Red reagent was used to initiate the ELISA reaction and was allowed to incubate for 10 min at room temperature. Fluorescence was measured on a microplate reader at 544 nm excitation/590 nm emission. The readings were compared to a calibration curve and the ICAM-1 surface density was calculated.

3.2.4 Anti-ICAM-1 coated micro/nano particles

Neutravidin coated 210 nm and streptavidin coated 2 μm fluorescent particles were diluted to 1010 and 108 particles/ml respectively using Block-Aid, and sonicated for 5 minutes. Biotinylated antibody (anti-ICAM-1, control or both) was added next after diluting the particles in 1% BSA. The 210 nm particles were diluted to 109 particles/ml and the 2 μm particles were brought down to 107 particles/ml and the antibody concentration was kept to a total of 10 $\mu\text{g/ml}$. Particles were incubated for 3 hours while shaking at room temperature and the unbound antibody was removed by centrifugation. The particles were washed in 1% BSA solution to remove any leftover unbound antibody and then diluted to working concentration for the flow tests. Particle concentration was analyzed on a microplate reader at 485 nm excitation/530 nm emission and compared to a calibration curve constructed from stock particle solution.

3.2.5 Particle anti-ICAM-1 density characterization

An ELISA was performed using HRP conjugated anti-mouse k-light chain specific monoclonal antibody to characterize the particle surface antibody density. The specificity of the reagent to mouse antibody light chain provides a direct measurement of the anti-ICAM-1 binding sites available on the particle. Particles were incubated with 5% HRP conjugated anti-mouse k-light chain specific monoclonal antibody for 30 minutes, followed by washing with 1% BSA solution and clearing out of unbound antibody through centrifugation. 50 μl of the particle solution were loaded on a 96-well plate and the particle concentration was analyzed. Then 50 μl of Amplex Ultra Red reagent was added to each well and the

HRP-substrate reaction was allowed to proceed for 10 minutes at room temperature. The fluorescence intensity of the particle sample with Amplex Ultra Red reagent was observed on a microplate reader at 544 nm excitation and 590 nm emission. The fluorescence intensities were converted to the number of HRP molecule using the calibration curves prepared using biotinylated-HRP conjugation to the neutravidin/streptavidin coated particles. Assuming a 1:1 binding ratio between anti-ICAM-1 and secondary antibody, the anti-ICAM-1 density on the particles were determined. In order to make sure the reaction mechanism and kinetics involved for anti-ICAM-1 binding on particle and while performing ELISA are same in the nano and micron sized particles, we compared the fluorescence intensity for similar anti-ICAM-1 density case of both particle sizes. This helps to make sure that the different protein and antibody binding reactions involved while performing ELISA doesn't vary based on particle size and other possible steric hindrance factors.

3.3 Results and Discussion

3.3.1 Characterization of particle and PDMS substrate protein densities

ICAM-1 coating density of the microfluidic channels was kept the same for all flow cases. It was determined by applying ELISA on PDMS coated glass slides as described before [68]. ICAM-1 density on our microfluidic channels was measured to be 121 ± 12 sites/ μm^2 .

NeutrAvidin coated 210 nm and Streptavidin coated 2 μm particles were functionalized with anti-ICAM-1 based on biotin-avidin chemistry. The anti-ICAM-1 coating density on the particle was determined using ELISA. Complete saturation of antibody coating on 210 nm particles produced 239.3 ± 25 anti-ICAM-1/particle. This was brought down to 157.9 ± 19 and 78.6 ± 9 anti-ICAM-1/particle. This corresponds to $1905.3 \pm 199/\mu\text{m}^2$ for the maximum antibody density case, followed by 1257.1 ± 151 and 625.8 ± 71 anti-ICAM-1/ μm^2 . The 2 μm particles were tuned to have a density of 12184.1 ± 264 and 2767.9 ± 103 anti-ICAM-1/particle which corresponds to 1199.2 ± 25 and 272.2 ± 10 anti-ICAM-1/ μm^2 respectively. Particle coating density was tuned using biotinylated goat IgG control antibody.

3.3.2 Specificity of anti-ICAM-1 coated particle binding to ICAM-1 coated surface

The specificity of particle binding to ICAM-1 coated surfaces was studied by comparing the binding of anti-ICAM-1 coated particles to negative control case (Figure 3) 210 nm and 2 μm sized particles were coated with 1905.3 and 1199.2 anti-ICAM-1/ μm^2 respectively. Both pure buffer and RBC 25% cases were performed at a shear rate of 200 s^{-1} . Particles specifically bound to ICAM-1 coated

microfluidic channel with around ten times higher density when compared to the negative control case, for both pure buffer and with RBCs cases.

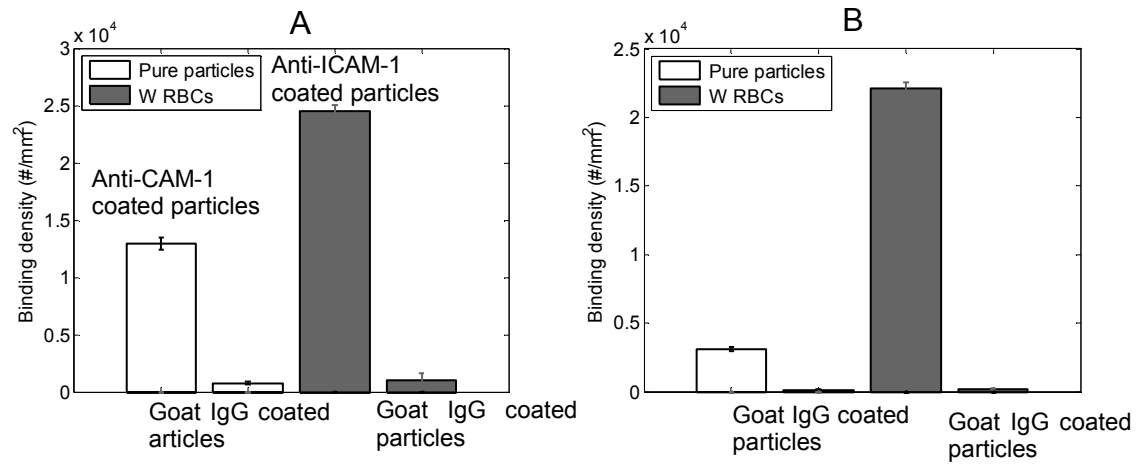


Figure 3: Binding density of anti-ICAM-1 and negative control (Goat IgG control) antibody coated (A) 210 nm particles and (B) 2 μ m particles under 200 s^{-1} shear

3.4 Conclusion

A bifurcating microvasculature mimicking PDMS microfluidic platform has been developed in this work. We are capable of tuning the channel shape, size and specific receptor protein coating based modelling of desired blood vessel state with control of protein coating density. We also produced drug carrier modelling particles coated with specific ligand molecules with the ability to control the coating density. The channels were coated with ICAM-1 and the protein density was set to model a microvessel in an inflamed state. The 210 nm and 2 μm particles were coated with ICAM-1 antibody at different coating densities and characterized. The specificity tests of anti-ICAM-1 coated particle binding to ICAM-1 coated surfaces have also been performed using anti-ICAM-1 and negative control (Goat IgG control) antibody coated 210 nm particles and 2 μm particles binding under flow test at 200 s^{-1} shear rate for both pure buffer and RBC 25% flow cases.

Chapter 4

Characterization of targeted nano and micro particle delivery in microcirculation

4.1 Introduction

This section studies the binding distribution of anti-ICAM-1 coated particles on ICAM-1 protein coated microfluidic device. Various factors like, vessel geometries (straight and branched channels), flow shear rates ($200-1600 \text{ s}^{-1}$), particle flow along with RBCs, particle size (210 nm and 2 μm), and particle ligand coating density, that influence particle binding distribution were analyzed. Around 10% higher particle binding density is observed at bifurcation regions of the mimetic microvasculature geometry compared to straight regions. Particle binding density is found to decrease with increased shear rates. RBCs enhance particle binding for both 210 nm and 2 μm . The particle binding density increases about 2-3 times and 6-10 times when flowing in whole blood at 25% RBC concentration compared to the pure particle case, for 210 nm and 2 μm particles respectively. With RBCs, the binding enhancement is more significant for 2 μm particles than that for 210 nm particles, which indicates an enhanced size dependent exclusion of 2 μm particles from the channel center to the CFL. Increased particle antibody coating density leads to higher particle binding density for both 210 nm and 2 μm particles.

4.2 Methods

4.2.1 Microfluidic flow test cases

The microfluidic device is designed to mimic the geometry of typical microvasculature. The design contains both straight and branching sections. The bifurcating angle was decided from measurements on arterial microcirculation system, theoretical values based on Murray's law and the bifurcation angle relationships of minimum work principle [73]. Particle binding density at straight and branching regions are calculated separately. The area considered to be the bifurcation section starts from the point where straight channels begin to bifurcate and ends in the daughter channel at a length of 2.5 times the vessel diameter from the apex of bifurcation (Figure 4). This was based on the principle that it takes about 2 times the distance of vessel diameter for the re-establishment of parabolic flow after bifurcation [74].

Anti-ICAM-1 coated particles were subjected to flow through ICAM-1 modified microfluidic devices at different shear rates between 200 and 1600 s^{-1} . This corresponds to physiologically relevant values observed in the microvessels [75-76]. The binding session was followed by a PBS only flushing session to remove unbound particles and to study particle detachment. This is performed at the same shear rate used to study particle attachment. The shear rate of flow in daughter channels are half that of the parent channel after branching, as they have the same dimension as the parent channel and also the daughter channels are of the same length. The particle concentration is kept at $10^8/\text{ml}$ and $10^6/\text{ml}$ for 210 nm and 2 μm particles respectively. The duration of flow was fixed at 15 and 20 minutes for

210 nm and 2 μm particles respectively. These time periods and particle concentrations were decided to accommodate all particle binding studies to a window where the binding rate was steady and the binding density could be practically quantified. Since the particle concentration and flow time are kept constant for all shear rates, the numbers of total particles introduced into the channels increase with shear rate. This factor is considered while calculating the particle binding density. The results were normalized to a total particle count of $10^6/\text{flow case}$ for all studies performed. The normalization process is explained in the supplementary information (Table S7). To compare the effect of particle size on binding, few flow cases were performed at $10^6/\text{ml}$ concentration for 210 nm particles.

Particle binding density was computed from confocal scans of the bottom surface of the channel. Time lapse imaging was performed in order to determine the attachment and detachment profile of the particles under different flow conditions. Analysis of particle binding was performed on a high resolution laser confocal fluorescence microscope (FV1000-IX81, Olympus). The particle binding density is computed at the center section of the bottom channel surface. The center section of the channel is decided by excluding areas within 25% of the channel width from edges. Flow conditions are more stable at the center compared to the edges of the channel and thus the variation in particle binding density is low here.

Flow tests were performed with particles diluted in pure buffer and whole blood with 25% RBC hematocrit, which represents the average hematocrit in microvessels [77]. Whole blood with 40% RBC concentration was brought down

to 25% by diluting in human blood plasma. The RBC flow case studies the influence of RBCs on particle diffusion and binding in microvessels. Blood plasma can contain soluble factors like CAM molecules which vary from donor to donor and can possibly affect the binding of particles on ICAM-1 modified substrates [78-79]. Thus the same pool of plasma and whole blood was used for all RBC flow test cases and the tests were performed the same day to normalize the effect of these soluble factors.

Fluid flow was generated using a programmable syringe pump (Harvard Apparatus), which controls the volumetric flow rate that is proportional to the wall shear rate. The wall shear rate $\dot{\gamma}$ was derived from the volumetric flow rate Q using the following relation:

$$\dot{\gamma} = (6Q/H^2W) (1 + H/W) f * (H/W)$$

Where H is the height and W is the width of the microfluidic device. 'f' is a geometry factor derived from the ratio of width to height. In this study, a microfluidic channel with a height and width of 100 μm is used, thus $f=0.5928$ [80].

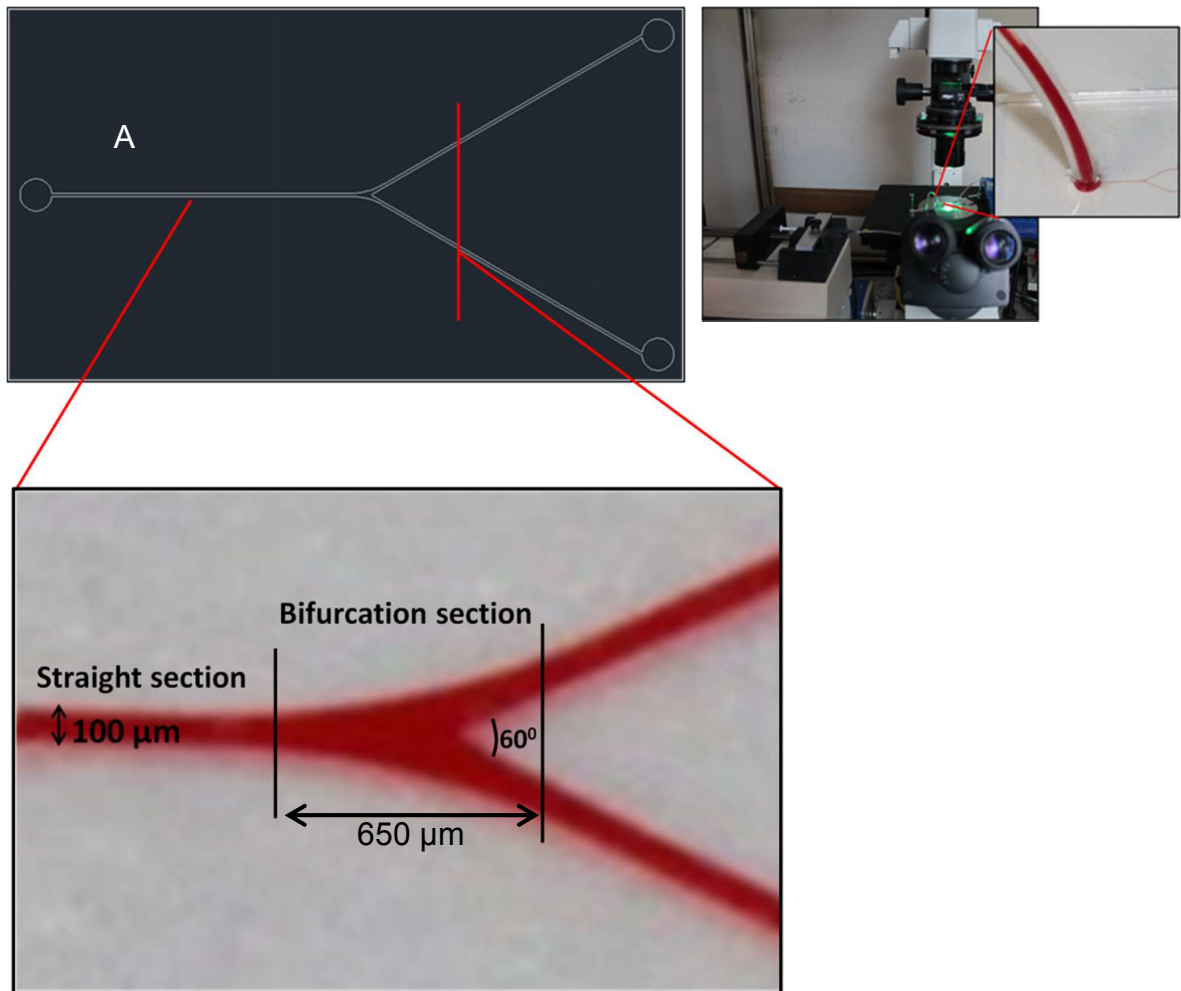


Figure 4: (A) CAD design of microchannel geometry, enlarged part illustrates the straight and bifurcation section of the channel; (B) The flow test set-up.

The effect of asymmetric flow between daughter branches on particle binding was also studied. For daughter channels with identical width and height, the relationship between flow rate and resistance is simplified to $L_a Q_a = L_b Q_b$ [81] (L_a, Q_a, L_b and Q_b are the length and flow rate of the daughter channels a and b respectively). Based on this, a change in length in one of the daughter channel would proportionally change the flow rate in that channel. A change in flow rate would translate to a direct proportional change in shear rate of flow (Table 1 on page 25). Channels were designed to generate different flow distribution in the two

daughter channels as shown in Table 1. The shear rate in one of the daughter channel is half of the other. Only straight sections of both the parent and daughter channels (after branching) were scanned to quantify the particle binding density in this case. Particle binding was quantified at the same distance from branching apex for both the daughter channels.

4.3 Results and Discussion

4.3.1 210 nm and 2 μm particle binding distribution

In order to study the binding and flow dynamics of particles studies were performed on 210 nm and 2 μm particles suspended in both pure buffer and whole blood (25% RBC). Binding of particles on both straight and bifurcating regions of the channel was examined. The binding density of 210 nm and 2 μm particles decreases with shear rate in both straight and branching channels for pure buffer case (

Figure 5, Figure 9; A and C). This can be explained by the decreased available time for particle to diffuse/marginate toward the wall under increased flow rate. However, for the RBC 25% flow case (

Figure 5, Figure 9; B and D) an increase in binding density is observed till the 550 s^{-1} shear rate.

The decrease in particle binding density with an increase in shear rate can be explained as the binding process being in a reaction limited regime as explained. The RBC 25% flow case showed ~2-3 times enhanced binding density when compared to pure buffer flow case for 210 nm particles, with the difference decaying with increase in shear rate (

Figure 5). The 2 μm particles showed around 6-10 times increase in binding density when suspended in 25% RBC depending on the shear rate (Fig 5 B and D) when compared to the pure buffer case. This increase in particle binding density can be explained by the availability of more particles close to the near wall region when

flowing with RBCs. The presence of RBCs pushes out particles from the channel center towards the near wall CFL region, thereby bringing more particles closer to the ICAM-1 coated surface. As the shear rate increases from 550 s^{-1} to the higher shear regime, particle binding density drops for the RBC case like the pure buffer case. This is likely because the localization of particles to the CFL saturates or drag force produced by flow shear exceeds adhesion force between ICAM-1 and anti-ICAM-1 receptor ligands.

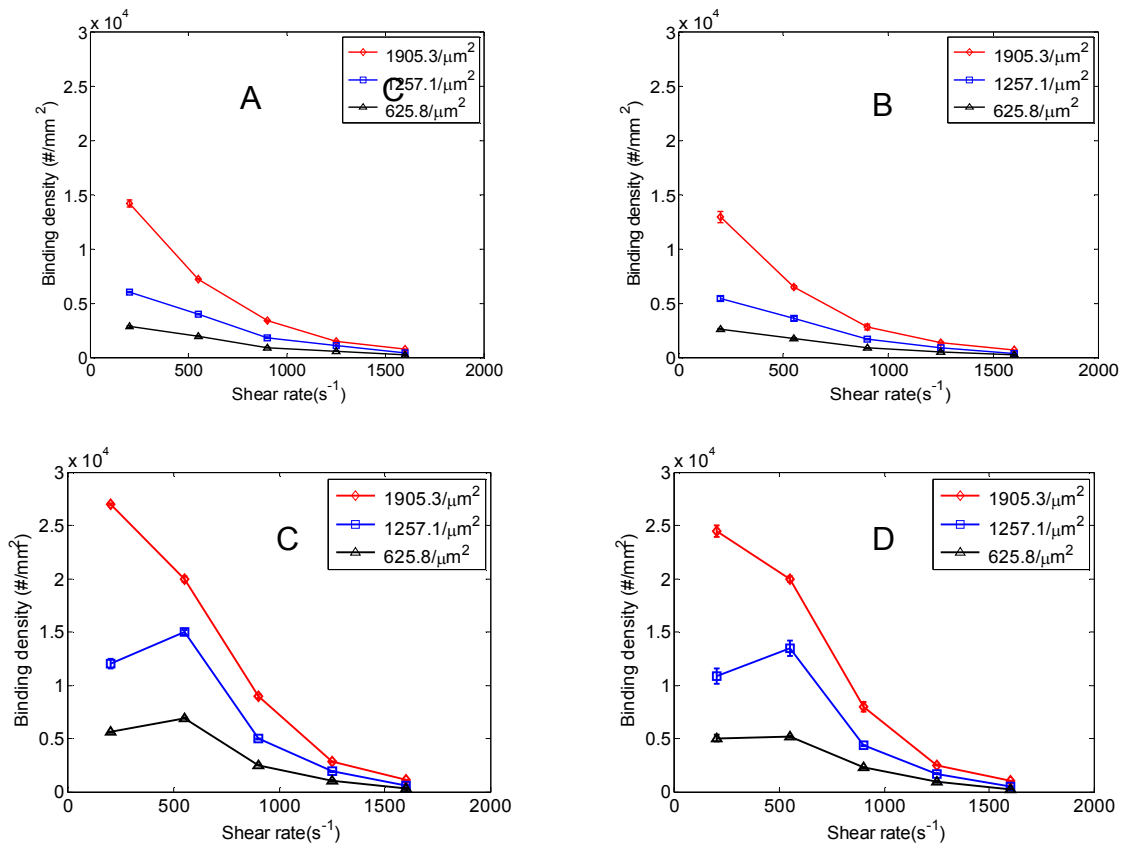


Figure 5: Normalized particle binding density ($\#/mm^2$) at shear rates 200-1600 s^{-1} ; at branching section of channels under (A) pure buffer flow and (B) RBC flow for 210 nm particles; at straight section of channels under (C) pure buffer flow and (D) RBC flow for 210 nm particles. Binding densities are plotted for 1905.3, 1257.1 and 625.8 anti-ICAM-1/ μm^2 particle antibody densities. Error bars represent standard deviation for three independent flow cases each.

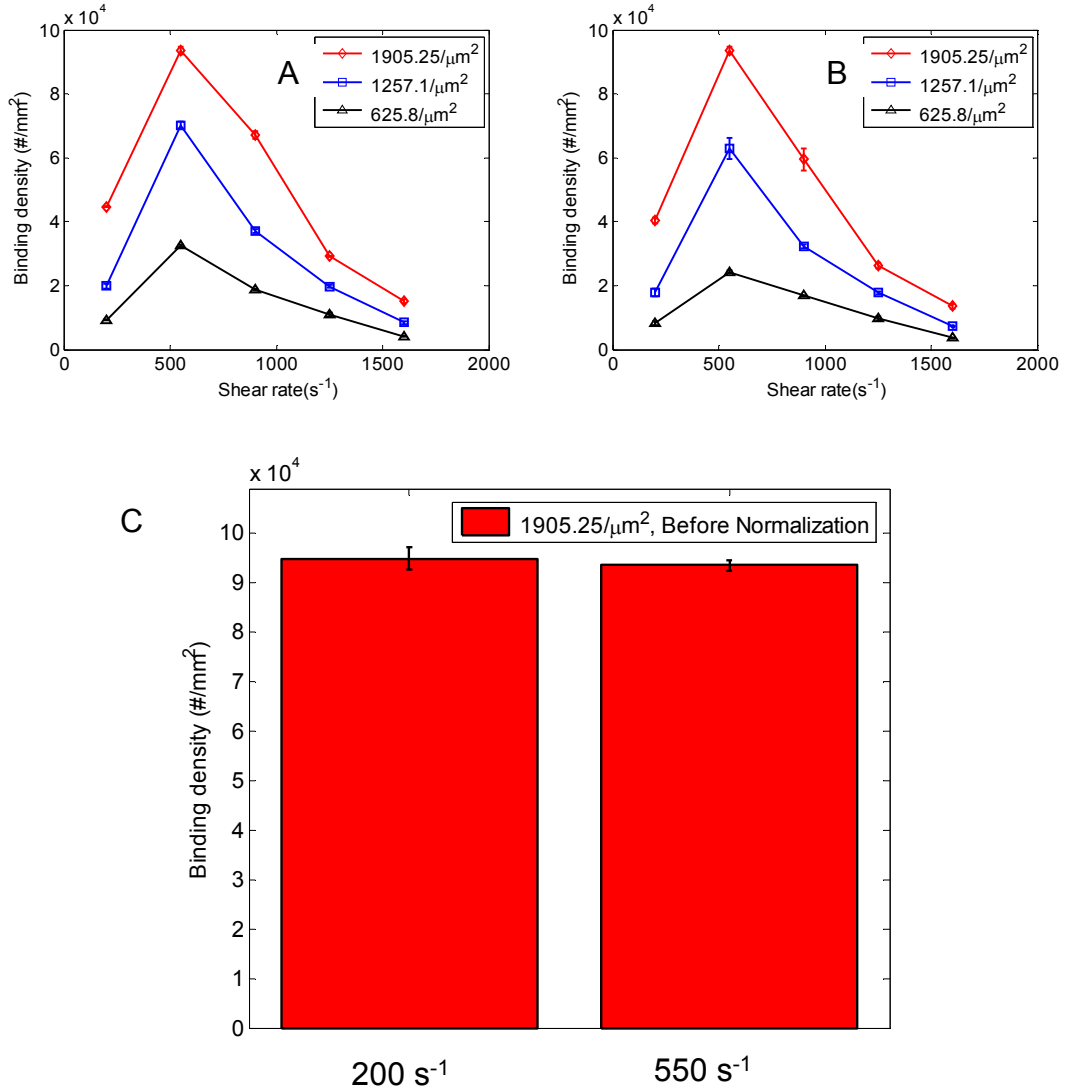


Figure 6: Particle binding density (#/mm²) at shear rates between 200-1600 s⁻¹ under RBC flow for 210 nm particles at (A) branching section of channels and (B) straight section of channels without data normalization; (C) Particle binding density of 210 nm particles with an anti-ICAM-1 coating density of 1905.3/μm² under RBC flow at 200 s⁻¹ and 550 s⁻¹ shear rate without normalization. 200 s⁻¹ shear rate case was subjected to an extended flow of 45 minutes to match with the total number of particles flown for the 550 s⁻¹ case (15 minutes flow).

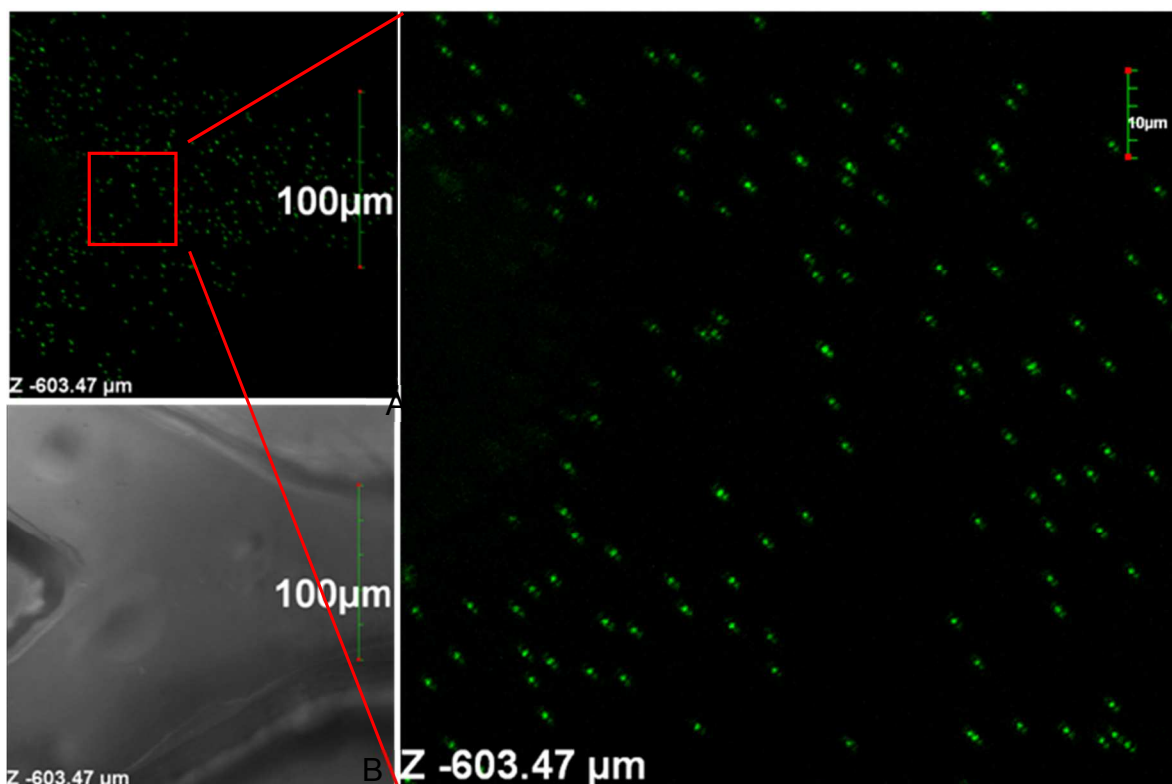


Figure 7: (A) Zoomed in image of 210 nm particle binding at 1250 s^{-1} shear rate for $1905.25/\mu\text{m}^2$ anti-ICAM-1 particle coating density; (B) Phase contrast image of Fig S2 A ; (C) 6X times zoomed in image scan of Fig S2 A showing each 210 nm particle.

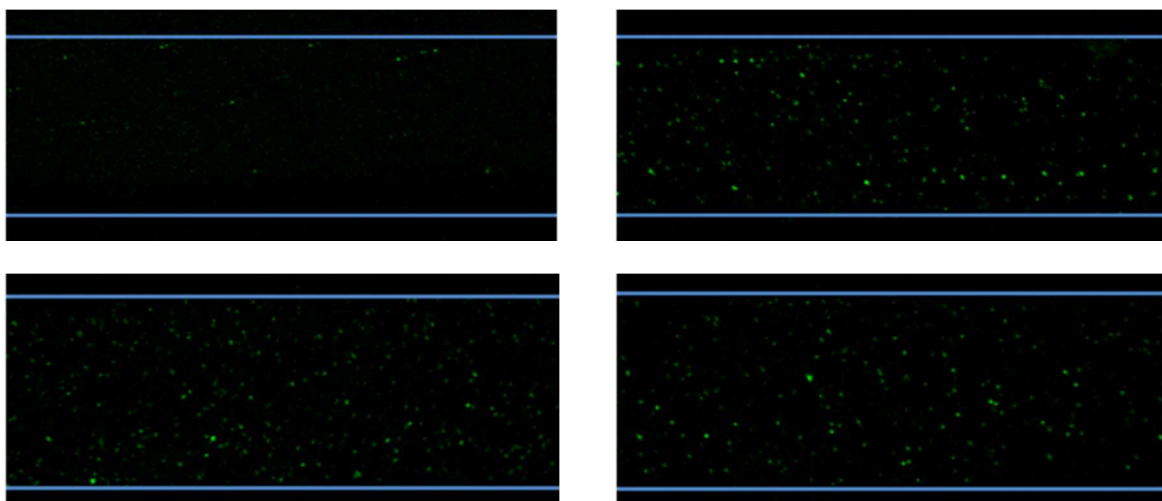


Figure 8: Confocal microscopy scan of free suspending 210 nm particle localization to the near wall region for: (A) Pure buffer case at 200/s shear rate (B) RBC 25% case at 200/s shear rate (C) RBC 25% case at 550/s shear rate (D) RBC 25% case at 900/s shear rate in the $100 \mu\text{m}$ wide microfluidic channel at a particle concentration of $10^8/\text{ml}$. The image is a sum of the stack of confocal scan images from $1 \mu\text{m}$ above the channel base to a height of $5 \mu\text{m}$ in the z direction.

The decrease in particle binding density with an increase in shear rate can be explained as the binding process being in a reaction limited regime as explained in *Namdee et al's* and *Charoenphol et al's* work [82-83]. A similar drop in particle binding density for 210 nm particles with increase in shear rate is also observed in Haun and Hammer's work [68]. At higher shear rates the larger drag force can easily wash away larger attached particles regardless of anti-ICAM-1 coating density. Work by *Patil et al.* found the shear rate required to set in motion a firmly adhered microsphere to decrease with increasing microsphere diameter [84]. This is a result of same shear producing higher drag force on larger particles. Thus shear rate based detachment effects are more dominant in the larger 2 μm particles compared to the 210 nm ones. This is consistent with existing literature [84-86].

The binding density also increases with particle anti-ICAM-1 density for all flow cases and both particle sizes under study. Higher antibody coating density provides a better possibility of enough ligand-receptor bond formation to assure firm attachment of the particles to the ICAM-1 coated surface [68, 87]. For 2 μm particles at 200 s^{-1} shear rate there is about five time increase in particle binding density for the 1199.2/ μm^2 case over the 272.2/ μm^2 anti-ICAM-1 density case (Figure 9 B and D). However such antibody coating density induced increase in binding density decays at higher shear rates for the 2 μm particles. It is observed that at 1600 s^{-1} shear rate both particle anti-ICAM-1 coating densities show similar binding density. At lower shear rates the particle binding is influenced more by the receptor-ligand interaction. However at higher shear rates the 2 μm particle binding

process is influenced more by the availability of particles near the wall region and the detachment of particles by the high flow shear rate. In terms of channel geometry, 10% higher NP binding density is observed at bifurcations compared to straight channels. Flow disturbances or alteration of flow at bifurcation regions lead to enhanced particle collision with the wall, which enhance binding [88-91].

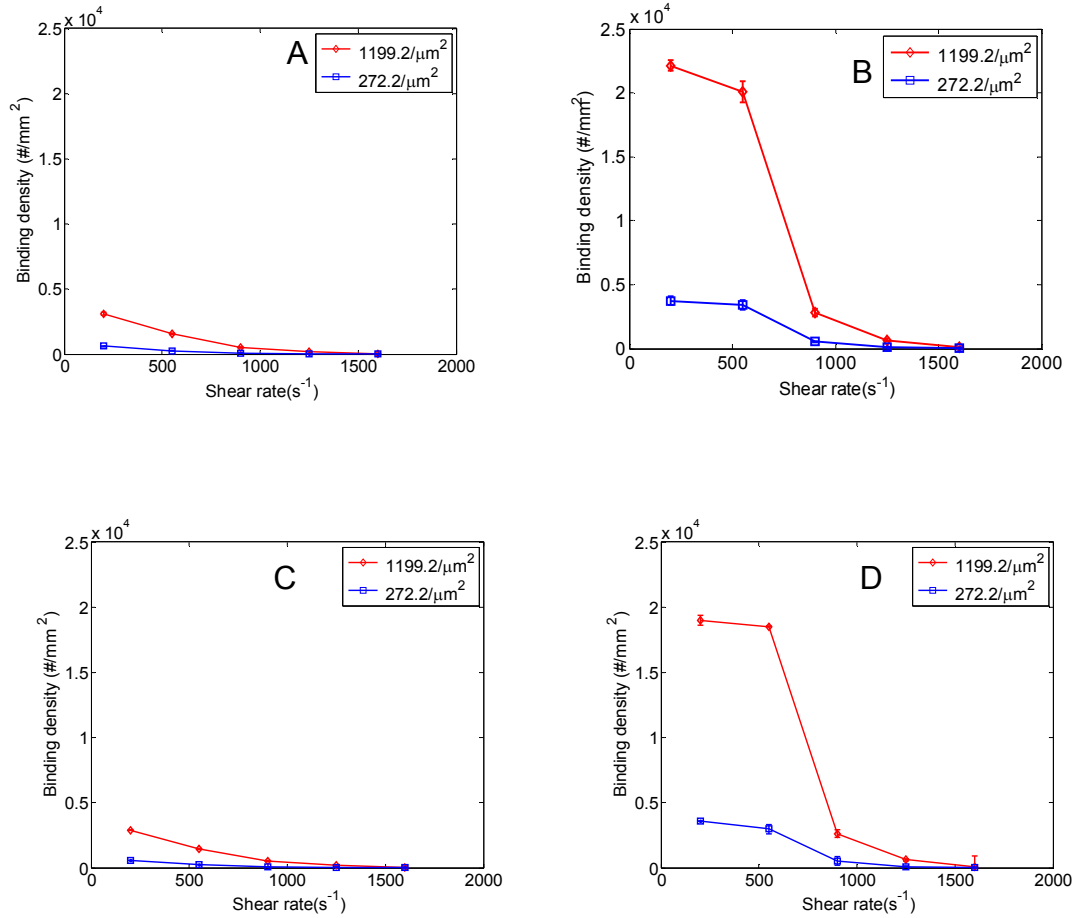


Figure 9: Normalized particle binding density ($\#/mm^2$) at shear rates between 200-1600 s^{-1} ; at branching section of channels under (A) pure buffer flow and (B) RBC 25% flow for 2 μm particles; at straight section of channels under (C) pure buffer flow and (D) RBC 25% flow for 2 μm particles. Binding densities are plotted for two different anti-ICAM-1 particle coating densities; 1199.2 and 272.2 anti-ICAM-1/ μm^2 . Error bars represent standard deviation for three independent flow cases each.

4.3.2 Comparison between binding of 210 nm particle and 2 μm particles

A comparison is performed on the binding density characteristics of 210 nm and 2 μm particles with similar anti-ICAM-1 densities (1257.1 and 1199.2 anti-ICAM-1/ μm^2 for 210 nm particles and 2 μm particles respectively) in this section.

Fig 7 A and B compares the particle binding density for 210 nm and 2 μm particles for pure buffer and RBC 25% flow case respectively. For the RBC flow case 2 μm particles show higher binding for shear rates up to 550 s^{-1} . This is constant with work by *Namdee et al.* [83] who also observes increased binding for 2 μm particles compared to 200 nm when flowing in a 30% RBC solution. For higher shear rates the larger drag force acting on bigger 2 μm particles leads to detachment and thus produces less particle binding compared to 210 nm particles.

For the pure buffer case the binding density of 210 nm particles is 2-3 times higher than 2 μm particles. However, it should be noted that this study was conducted at a particle concentration of 108/ml for the 210 nm particles and 106/ml for the 2 μm particles. In order to understand the effect of this 100 times increase in particle concentration on binding density, we also did flow tests at 106/ml particle concentration for 210 nm particles. It was observed that both the pure buffer and RBC 25% flow cases produced particle binding that didn't vary significantly with changes in factors such as shear rate, particle antibody density or flow with RBCs (data not shown). To understand this we measured the localization of 210 nm particles at this concentration near the wall region for the pure buffer and RBC 25% case using confocal microscope scanning. No significant fluorescence signal was observed near the wall region when compared to the 108/ml case (Fig S3), which

indicates the lack of particle localization to near wall CFL region. Our study was conducted at a particle concentration of 108/ml for the 210 nm particles and 106/ml for the 2 μm particles and the results were normalized to 106 particles/flow case for both particle sizes. Thus this 100 times higher 210 nm particle concentration should have translated to the higher particle binding density observed in the pure buffer case. The work by *Namdee et al.* [83] also observes an increase in particle binding density with increased particle concentration for the pure buffer case.

Fig. 7C compares the magnitude of increase in particle binding density for RBC 25% whole blood case compared to the pure buffer case for the 2 μm and 210 nm particles with similar anti-ICAM-1 density. This is done by calculating the ratio of increase in particle binding density for the RBC 25% case over the pure buffer case under the same shear rates for both 2 μm and 210 nm particles. 2 μm particles show almost three times increase in binding ratio when flowing with RBCs compared to similar 210 nm particle case for shear rate up to 550 s^{-1} . Even at high shear rates above 550 s^{-1} 2 μm particles show almost twice the binding ratio compared to 210 nm particles, although detachment becomes dominant as shear rate increases.

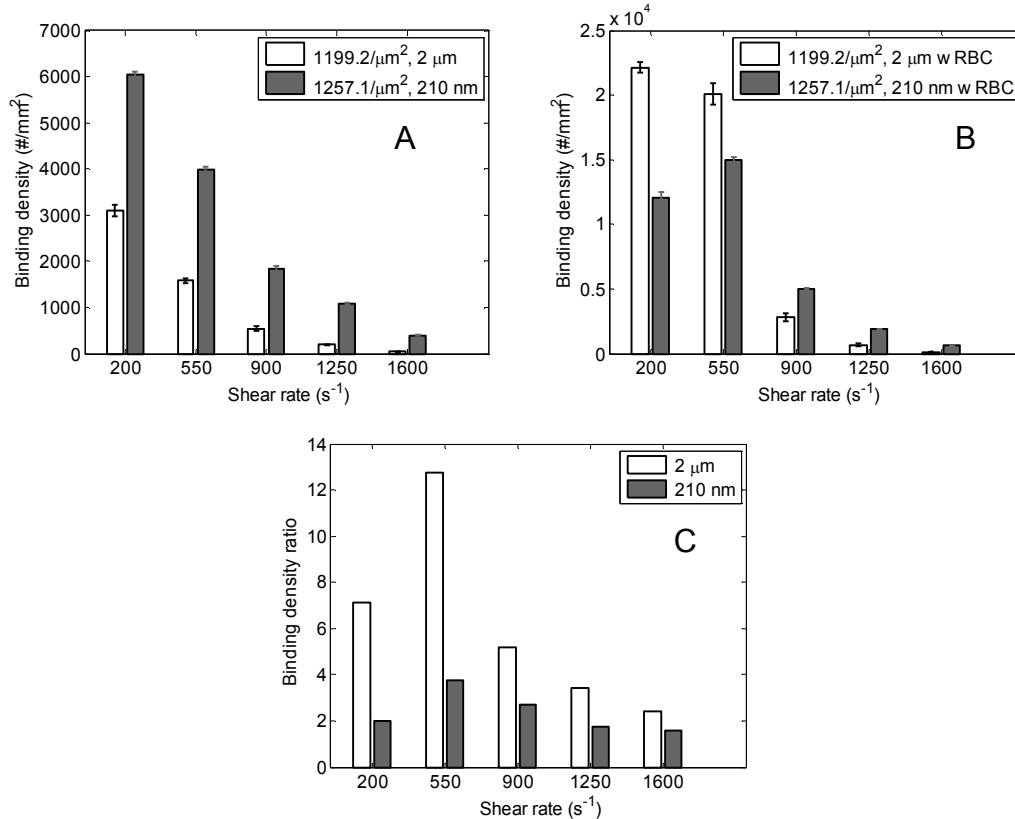


Figure 10: Normalized particle binding density (#/mm²) for 210 nm (1257.1 anti-ICAM-1/μm²) and 2 μm (1199.2 anti-ICAM-1/μm²) particles are compared for (A) pure buffer flow case and (B) RBC 25% flow case at different shear rates; (C) Comparing ratio of particle binding density of RBC flow case to pure buffer flow case for 210 nm (1257.1 anti-ICAM-1/μm²) and 2 μm (1199.2 anti-ICAM-1/μm²) particles at different shear rates;

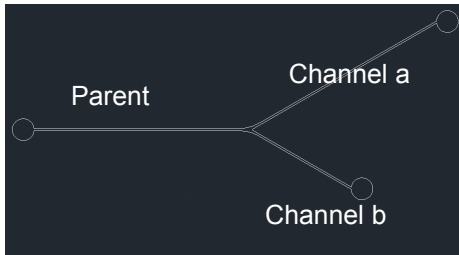
Prominent binding is observed for the 2 μm particle for RBC 25% flow case when compared to 210 nm particles due to size based enhanced particle margination to the CFL. Particles or cells marginate toward the near wall cell free region when flowing along with RBCs [82, 92-94]. This occurs because of their interaction with RBCs and the deformation of the RBCs in flow. The collision between the deforming RBCs during flow easily pushes out particles or cells of size comparable to RBCs to the cell free plasma region. In Eckstein et al's work, a size selective enhanced exclusion of beads of diameter greater than 2.2 μm was observed [95].

In this confined region the interaction between the RBCs and particles increases the collision between the anti-ICAM-1 coated particles and the ICAM-1 coated PDMS surface and this leads to increased particle binding. A similar phenomenon was observed in other studies [82-83, 96]. Comparatively only a smaller percentage of 210 nm particles marginates toward the near wall region and most of them tend to flow along with RBCs in the core region because of their smaller size [95]. This along with their smaller size compared to the CFL (2-10 μm) [53, 97] produces lower increase in particle binding density compared to the 2 μm particle case.

4.3.3 Daughter channels with asymmetric flow velocity

In micro circulation, daughter channels can have differences in flow velocities between them after branching [55]. In order to study the effect of this asymmetric flow distribution between daughter branches on particle binding, we conducted tests in channels of geometries that produce this effect. The parent and daughter channels were of the same cross sectional area, but of different lengths. This would produce a variation in flow rate between the daughter channels such that the shear rate of one daughter channel would be half of the other. Daughter channel 'b' had half the length of channel 'a' (Figure along with Table 1) for this purpose. Table 1 lists the shear rates of flow in parent and the two daughter channels for the three flow cases performed. Flow tests were conducted for 210 nm and 2 μm particles having an anti-ICAM-1 coating density of 1905.3/ μm^2 and 1199.2/ μm^2 , suspended in 25% hematocrit whole blood.

Table 1: Shear rates in the parent channel and in daughter channels a and b for the different flow cases studied. Image shows the top view of the flow channel design that produces asymmetric flow in daughter channels



Flow case	Shear rate in parent channel	Shear rate in daughter channel a	Shear rate in daughter channel b
1	200	66.6	133.3
2	900	300	600
3	1600	533.3	1066.6

The binding density for 210 nm particles at a concentration of 108/ml is given in Fig 8 A. For the three flow cases at a shear rate of 200, 900 and 1600 s⁻¹ in the parent channel, higher particle binding density is observed in the daughter channel when compared to the parent channel. Daughter channel 'a' has 1/3rd and 'b' has 2/3rd the shear rate of the parent channel and between them channel 'b' has twice the shear rate of channel 'a'. The daughter channel 'a' shows almost 2 times higher binding density than channel 'b'. This can be explained by channel 'a' having half the flow shear rate of channel 'b'. 210 nm particles show similar increased binding density with decreased shear rate pattern as discussed earlier (Fig. 3).

For the 2 μm particles almost similar particle binding density was observed in parent and daughter channels for all shear rates other than for 1600, 1066.6 and 900 s⁻¹ (Fig 8 B) after normalization. These results match well with what we saw for RBC 25% case of 2 μm particles at different shear rates for a particle anti-ICAM-1 density of 1199.2/μm² (Fig 5). It is observed that the particle binding density begins to decrease dramatically for shear rate above 600 s⁻¹. This is because of large drag force from these higher shear rates acting on the particle,

which leads to decreased receptor ligand reaction and also increased particle detachment.

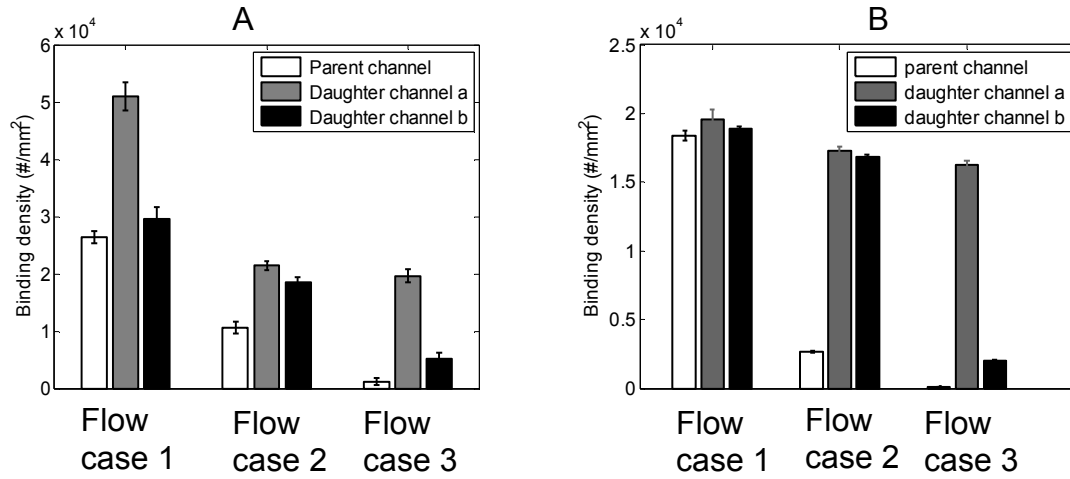


Figure 11: Normalized particle binding density in parent channel and daughter channels a and b for the asymmetric flow case under RBC flow for (A) 210 nm particles at 1905.3 anti-ICAM-1/μm² and (B) 2 μm particles at 1199.2 anti-ICAM-1/μm².

In flow channels where the daughter branches have different flow velocities, there might be a preferential, non-linear distribution of RBCs/particles to the daughter branch with the faster flow [98-100]. Thus the daughter channel with higher flow velocity/shear rate ends up receiving more RBCs/particles. We didn't observe such a preferential flow of particles to the daughter channel having the higher shear rate. This could be because our particle size is much smaller when compared to the flow channel cross section. Our 2 μm particle is only 0.02 times the size of the channel with a length and height of 100 μm each (210 nm particle becomes more insignificant). The above mentioned non-linear distribution are prominent only when the diameter of RBC/particle is of the same range as the channel diameter [99].

4.3.4 Attachment and detachment profiles

210 nm particles

To provide a more quantitative and physical understanding of particle binding process, attachment and detachment rates of particles are derived from the particle binding time histories. The time history profiles of particle density during attachment and detachment processes in pure buffer flow are shown in Fig S4. Attachment and detachment processes for NP of three different anti-ICAM-1 densities are compared.

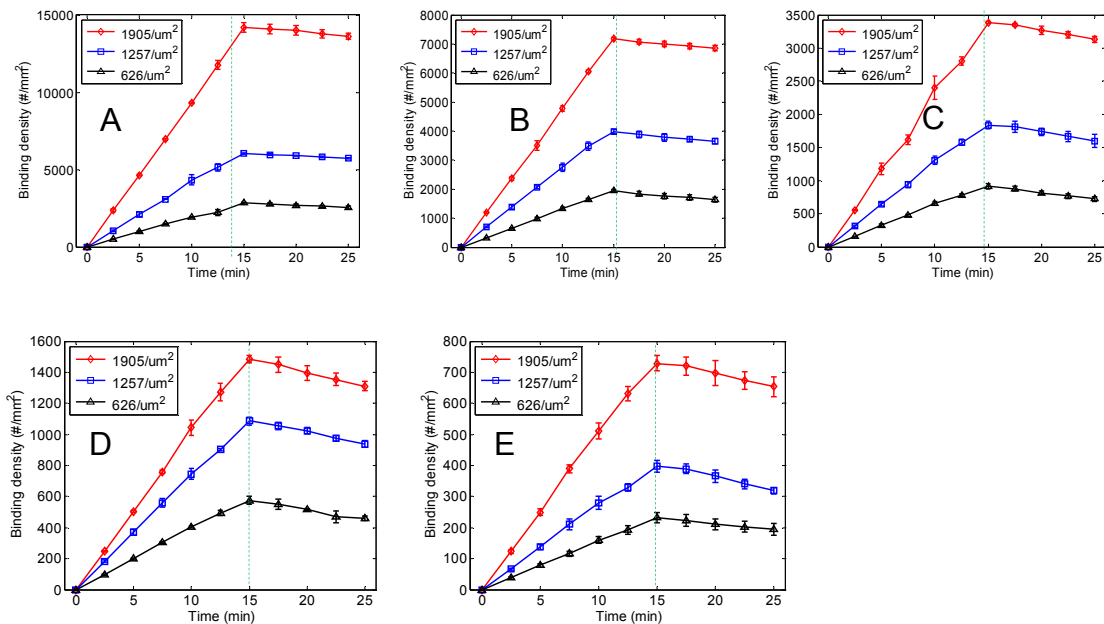


Figure 12: Attachment and detachment time history profile of normalized particle binding density data for 210 nm particles at shear rates (A) 200 s⁻¹ (B) 550 s⁻¹ (C) 900 s⁻¹ (D) 1250 s⁻¹ & (E) 1600 s⁻¹. All three anti-ICAM-1 particle densities of 1905.25, 1257.1 and 625.8 /μm² are studied. Dashed green line indicates the start of detachment period. Error bars represent standard deviation for three independent flow cases.

Time lapse microscopy was performed on the 210 nm particles binding in the microfluidic channel. Images were taken every 2.5 minutes and binding profile for a total time of 15 minutes was analyzed. This was followed by a washout period of 10 minutes at the same shear rate to clear unbound particles in solution and to study particle detachment process. During the first 15 minutes of attachment, particle binding density increases linearly with time for a certain shear rate. The binding rate is calculated from the slope of the binding density time history profile. The binding rate is found to decrease with increased shear rate (Fig. S6 A). Increased anti-ICAM-1 density on the particle leads to a higher binding rate. Particle detachment was observed when buffer solution was flowed through the microfluidic channel after 15 minutes. For 210 nm particles a detachment of ~4-6% of particles occurred when compared to the total number of attached particles. This indicates that 210 nm particles are hard to be detached once they adhered to the surface. This is likely due to the small size of the particle that leads to small drag force acting on them and strong ligand-receptor binding even through the formation of a single bond.

2 μm particles

Similar to 210 nm particles, the attachment and detachment rates of 2 μm particles in pure buffer flow are derived from the particle binding time histories. Time lapse microscopy on the particle binding in the microfluidic channel was performed every 2.5 minutes. Binding profile for a total of 20 minutes was analyzed and this was followed by a washout period of 10 minutes to clear unbound particles in solution and to study particle detachment process. The first 20 minutes of attachment

showed particle binding density increasing linearly with time for a certain shear rate (Fig S5). The binding rate is calculated from the slope of the binding density time history profile. The binding rate is found to decrease with increased shear rate (Fig. S6 C). Increased anti-ICAM-1 density on the particle leads to higher binding rate. Particle detachment was observed when pure buffer solution was flowed through the microfluidic channel after 20 minutes of particle attachment study. 2 μm particles have high detachment rate, much higher than the attachment rate (Fig S6 C & D). This indicates shear based drag force acting on particles is dominant on the 2 μm particles compared to 210 nm particles.

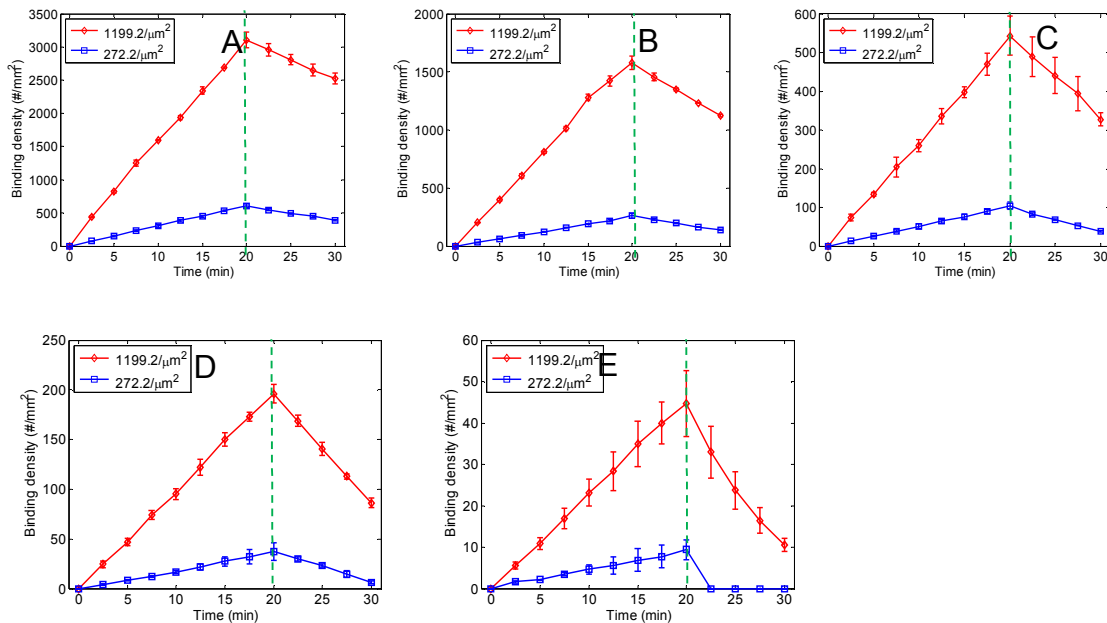


Figure 13: Attachment and detachment time history profiles of normalized particle binding density for 2 μm particles at shear rates (A) 200 s⁻¹ (B) 550 s⁻¹ (C) 900 s⁻¹ (D) 1250 s⁻¹ & (E) 1600 s⁻¹. Both anti-ICAM-1 particle densities of 1199.2 and 272.2 / μm^2 are studied. Dashed green line indicates the start of detachment period. Error bars represent standard deviation for three independent flow cases.

4.3.5 Derivation of attachment and detachment rates from experimental data

To retrieve NP adhesion and detachment rate, a first order particle adhesion kinetics is used to fit the binding history:

$$\frac{\partial c_s}{\partial t} = k_a c_0 - k_d c_s$$

Where c_0 is the initial bulk concentration of the NPs, c_s is surface concentration of binding NPs, k_a and k_d are attachment and detachment rates respectively. During early stage of binding, c_s is very small, thus, detachment can be neglected. The accumulation of NPs bonded to the surface can be found as $c_s = k_a c_0 t$. Through data fitting, the adhesion rates under different shear rates and antibody densities are plotted in Fig S6. As shown from the figure, the adhesion rate is found to decrease with shear rates and increases with antibody density coated on particle surface. 210 nm particles are more than one order of magnitude higher in adhesion rate compared to 2 μm particles for pure buffer case.

Likewise, setting $k_a=0$, $\frac{\partial c_s}{\partial t} = -k_d c_s$, the detachment rate can be found by fitting the detachment curve using formula $c_s = \exp(-k_d t + \text{const})$. The detachment rate is found to increase with shear rate and decrease with antibody density. It should be noted that 2 μm particles with antibody density of 272.2 / μm^2 are all washed away thus have no data available at shear rate of 1600 s⁻¹.

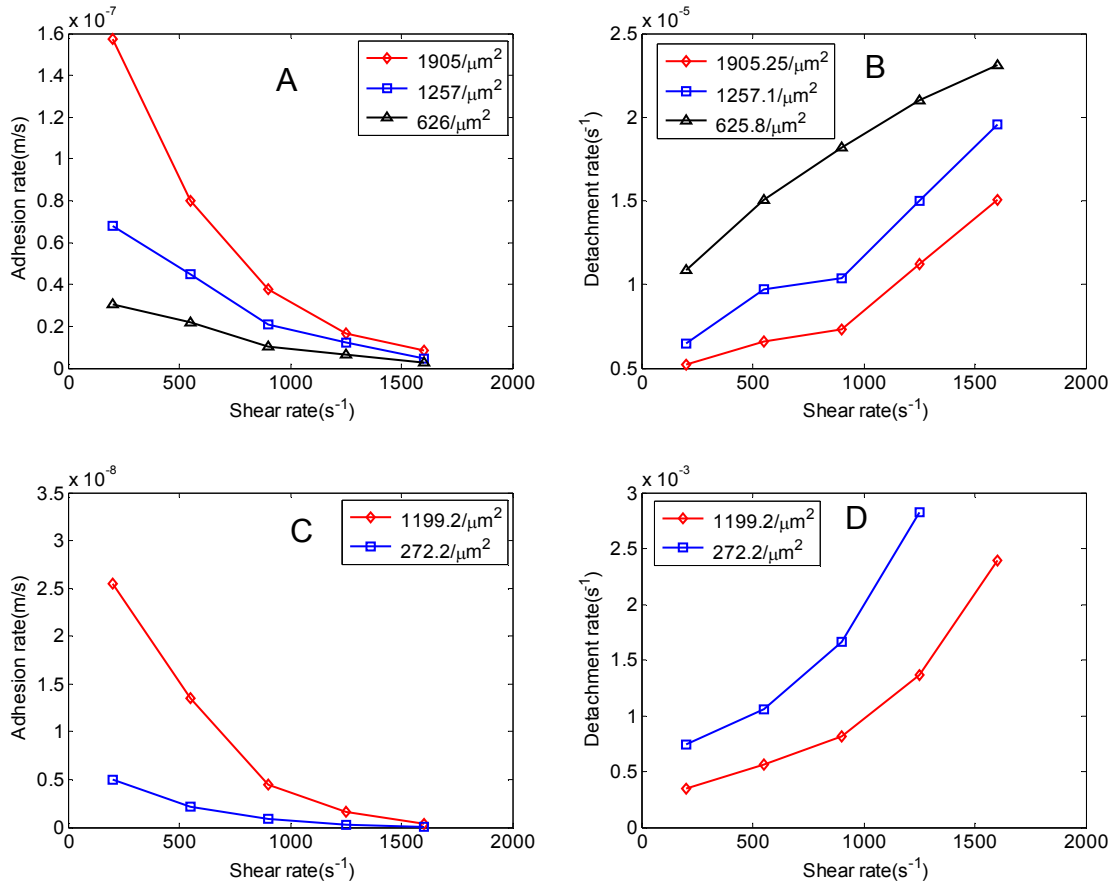


Figure 14: Particle attachment and detachment rates for 210 nm (A-B) and 2 μm particles (C-D), respectively.

4.3.6 Normalization process to bring all flow cases to a total particle count of 10⁶/flow case

- Consider the flow rate to be 1 ml/hr to achieve 200/s shear rate.
- Particle concentration: 10⁸/ml
- Flow time: 10 minutes

Table 2: Detailed steps of the normalization process performed to bring all flow cases to a total particle count of 10^6 /flow case

Shear rates	Corresponding flow rate	Total particle flown in 10 minutes	Total particle binding (hypothetical)	Particle binding after normalization to 10^6 particles/flow case i.e. $\left(\frac{\text{Total particles binded}}{\text{Total particles flown}}\right) * 10^6$
200/s	1 ml/hr	16666666.6	10000000	600000
900/s	4.5 ml/hr	75000000	30000000	400000
1600/s	9 ml/hr	150000000	50000000	333333.3

4.4 Conclusion

The binding density of anti-ICAM-1 coated 210 nm and 2 μm particles on ICAM-1 modified PDMS microfluidic devices is characterized in this work. The study employs various factors that influence particle distribution and binding such as flow shear rate, particle size, flow along with RBCs, vessel geometry, antibody coating density on the particle, particle concentration and effect of asymmetric flow distribution between daughter channels.

The particle binding densities for both 210 nm and 2 μm particles decrease with increased shear rate for pure buffer case. This can be explained by the decreased available time for particle to diffuse/marginate toward the wall under increased flow rate. RBCs play an important role in particle binding and distribution pattern. Both 210 nm and 2 μm particles show enhanced binding density at 25% hematocrit RBC flow. 210 nm particles showed 2-3 fold increase in binding under blood flow till a shear rate of 550 s^{-1} and 2 times increase in binding for much higher shear rates when compared to the pure buffer case. Similarly, 2 μm particles show around 6-10 fold increase in binding for shear rates up to 550 s^{-1} and around 4 times increased binding for much higher shear rates when compared to the pure buffer case. The steep drop in binding density observed for the RBC 25% flow case of 2 μm particles beyond a shear rate of 550 s^{-1} is a result of high shear flow induced large drag force acting on the bigger 2 μm particles leading to their detachment. The smaller 210 nm particles have much lower drag force acting on them compared to the 2 μm particles.

In terms of vessel geometry, both particles show a slight increase in binding density at the bifurcation region compared to the straight channels. This is observed for both pure buffer and RBC 25% flow case. Disturbance of flow at the bifurcation region leads to enhanced particle collision with the wall and results in higher particle binding density. This contributes to the enhanced binding observed at the branching section. Higher antibody coating density facilitates more rapid formation of sufficient ligand-receptor bonds to assure firm attachment of particles. Higher particle anti-ICAM-1 coating density thus increases binding density, except for high shear rate cases for 2 μm particles where shear based detachment drag force nullifies the enhancement brought by increased antibody density.

The results produced in our study can be related to clinically relevant drug delivery systems like liposomes[101], trimethyl chitosan (TMC)[102] and Poly(lactic-co-glycolic acid) (PLGA) based particles [103]. Our model system is spherical in shape and made of polymerized polystyrene, similar to structures generated through conventional techniques of particle fabrication like emulsion, precipitation and polymerization of formulations. The application of ligand based targeting is currently largely employed in such platforms to attain specific attachment and receptor mediated endocytosis to diseased cells. The ligand functionalization provides better therapeutic performance especially for macromolecules that cannot easily enter cells on their own [102-104]. Such targeted platforms also expresses better uptake by cells based on vascular permeability [105], tumor penetrability [105] and ligand-receptor density and affinity [106-107]. The particle

sizes in our study roughly cover the size range of established delivery platforms [102-103, 108].

Our work helps to determine the transport properties of drug carriers in the microvasculature. From this study we conclude that 2 μm particles have better binding efficiency based on number count and particle volume, for low to medium shear rate flow regions. For disease conditions where a higher particle concentration or dosage is acceptable (drug toxicity not an issue) and higher shear flows are involved, the smaller particles in the 200 nm scale would be more suitable. Properties like the enhanced particle margination and binding to the wall at high particle flow concentration observed in this study favour the use of NPs. Other advantages like the ability to be better retained in tissues via the enhanced permeability and retention effect, longer circulation period and better targeting ability are also in favour of NPs.

When designing targeted vascular drug carriers, various parameters have to be considered like the disease condition, permissible drug toxicity based particle concentration, reticuloendothelial system evading properties etc. This work is part of a project to develop a customized biomimetic microfluidic experimental platform that mimics specific microvasculature conditions based on disease state and physiological conditions. These goals are to be achieved by coating the microfluidic channels with endothelial cells to mimic vascular morphology and to mimic disease condition by introducing specific cytokines. Thus a more physiologically relevant test condition can be set up for studying nano/micro drug carrier distribution and binding.

Chapter: 5

Model 2: endothelial cell coated vascular morphology mimicking platform

5.1 Introduction

An endothelial cell coated blood vessel model on a microfluidic channel is the most fitting approach to prototype an *in vivo* blood vessel. Our model has been designed to mimic spatially controlled healthy and diseased vascular morphology regions in the same channel. This model will advance the understanding of mechanisms involved in drug carrier binding in a blood vessel at cellular level. It also examines the boundary effect on targeted binding in healthy vs. diseased sections of a blood vessel.

The endothelial cell coated blood vessel model proposed here has a top and bottom chamber separated by a semi-permeable, porous, cell culture friendly membrane (Figure 15). Endothelial cells will be grown on the membrane such that the apical plane of the cell faces the top chamber and the basal plane the bottom chamber of the device. The upper and lower chambers are denoted as the apical side and the basal side respectively, corresponding to cell polarity. The chambers are designed such that a section of the apical side can be accessed from the basal side through the semi-permeable membrane. Endothelial cells growing on this section can be specifically simulated to be pathologically challenged through cytokine based activation from the basal chamber. This facilitates the simulation

of spatially controlled healthy and diseased endothelial cells in the same channel. Achieving a stable and confluent monolayer of endothelial cells, adapting them to physiological flow conditions and characterizing cell growth and cell parameters in this device form important steps in this study. Once these are established, microfluidic flow studies on drug carrier particle binding will be performed under physiologically relevant conditions.

Primary BAOECs are used in this study and achieving a confluent monolayer of endothelial cells, adapting them to physiological flow conditions and establishing parameters for stable ICAM-1 expression form important steps in this study. We looked into the characteristics of endothelial cells cultured in our platform by studying the longevity of endothelial cells in these channels and investigating details on cell shape change and alignment by studying remodeling of actin microfilament network once exposed to FSS. Once the *in vitro* bio-mimetic blood vessel platform was established, flow studies on drug carrier particle binding were performed under physiologically relevant conditions. We characterized targeted nanodrug delivery in this more realistic blood vessel model and studied boundary effect of drug carrier binding in direct cytokine activated vs. non activated upstream and downstream vessel regions. This model will advance the understanding of mechanisms involved in drug carrier binding in a blood vessel at cellular level.

5.2 Materials and Methods

5.2.1 Materials

Human ICAM-1/CD54 MAb (Clone BBIG-I1) Mouse IgG1, ICAM-1/human IgG1 Fc chimera, biotinylated anti-human ICAM-1 (clone BBIG, mouse IgG1 κ) and Normal Goat IgG biotinylated control were purchased from R&D Systems, Minneapolis, MN). Protein G was bought from Biovision, Milpitas, CA. Horseradish peroxidase (HRP)-conjugated rat anti-mouse κ -light chain monoclonal antibody, neutrAvidin coated fluorescent yellow-green polystyrene 210 nm particles, Block-Aid, Amplex Ultra Red reagent and biotinylated-HRP were purchased from Invitrogen Carlsbad, CA. Mouse anti-human ICAM-1 monoclonal IgG1 antibody (clone 15.2) was from Ancell, Bayport, MN and HRP-conjugated rat anti-mouse IgG1 monoclonal antibody from BD Biosciences San Jose, CA. Bovine serum albumin (BSA) and 3-aminopropyltrimethoxysilane were bought from Sigma Aldrich, St Louis, MO. Streptavidin coated 2 μ m fluorescent green polystyrene particles were purchased from Bangs Laboratories Inc., IN and polydimethylsiloxane from Dow Corning, Midland MI.

5.2.2 Fabrication of bio-mimetic blood vessel model

Blood vessel mimicking channels are photolithographically fabricated on a silicon wafer and cast out of PDMS. The master for fabricating the channels is patterned on a silicon wafer using SU-8 2050 photoresist (MicroChem Corp.). Sylgard 184 PDMS (Dow Corning Corp.) was prepared according to manufacturer's instruction and cast over the photoresist pattern. The upper channel is 350 μ m wide and 100

μm tall, and the lower channel is 1000 μm wide and 100 μm tall. A polycarbonate (PC), track-etched thin clear membrane (Whatman, GE Healthcare) with 1 μm diameter pores and an average calculated pore density of 1.5×10^7 pores/cm² is embedded between two PDMS channels. The process by which the device has been arranged has been detailed in other publications [109-111]. The PDMS slabs containing the top and bottom channels are carefully peeled off the master template. The property of PDMS is tuned to be more cell culture friendly by extended baking (4 hrs at 80°C) to ensure complete cross linking of monomers [112], and any leftover monomers are extracted by soaking them in ethanol overnight [113]. The bottom PDMS channel is kept thin to facilitate microscopy based imaging using higher magnification objectives. The bottom PDMS channel layer is bonded on to a thin glass slide by exposing the sides in contact to oxygen plasma. Upper and lower PDMS channels are bonded to the membrane by using a thin PDMS mortar film. The mortar film is a mixture of PDMS prepolymer (10:1 ratio of base and curing agent) with toluene in equal proportion and a thin layer (~2-3 μm) is obtained by spin-coating this on a glass slide at 1500 rpm for 60 s. PDMS channel sides were stamped onto this thin film. Then the device is assembled with the membrane in between the PDMS slabs and making sure the channels are aligned. After assembly the device is placed in an oven at 60°C overnight for curing the PDMS mortar and ensuring the integrity of the device. Inlet and outlet ports were punched to provide access to top and bottom channels.

5.2.3 Endothelial cell culture in the device

BAOECs were cultured in hepes buffered DMEM supplemented with 10% heat inactivated fetal bovine serum (Atlanta Biologicals, Inc.) and 1% penicillin-streptomycin (Sigma-Aldrich). The device was sterilized in UV light overnight. Prior to cell seeding the upper channel and membrane of the device was coated with 50 µg/ml fibronectin solution (Sigma-Aldrich) overnight at 37°C. The channel was rinsed with media to remove any excess, unattached fibronectin. BAOECs cells were seeded onto the semi-permeable membrane in the upper channel at a density of 2×10^7 cells/ml. Cell seeded devices were placed in an incubator under standard culture conditions (37°C and 5% CO₂) overnight to allow cell attachment and spreading on the membrane. For the next 12 hrs the upper channel of the device was subjected to flow based media change at low FSS (0.01 dyne/cm²). Thus a constant supply of fresh media was available for the BAOECs without being subjected to FSS effects. Later the flow rate of media in the upper channel was gradually increased to subject the endothelial cells to physiologically relevant FSS values.

5.2.4 Application of shear stress

Quiescent phenotype of endothelial cells is critical to the success of our work and for this the confluent layer of BAOECs were subjected to physiologically relevant FSS. To calculate the volumetric flow rate that correspond to the required maximum FSS experienced by the endothelial cells, the following equation was used [114].

$$\tau_{cell} = \frac{6\mu Q}{wh^2}$$

On reaching confluence, the BAOECs were subjected to a FSS of 12 dyne/cm². The flow was brought about using a high precision and extremely low pulsation peristaltic pump (ISMATendothelial cell, IPC-N series) and the entire setup was placed in standard culture conditions. The use of a peristaltic pump allows multiplex access to the flow channel, providing the flexibility of introducing new entities (particles, specific biomolecules etc.) without disturbing the laminar FSS the BAOECs are being exposed to.

5.3 Results and Discussion

5.3.1 Design of microfluidic device

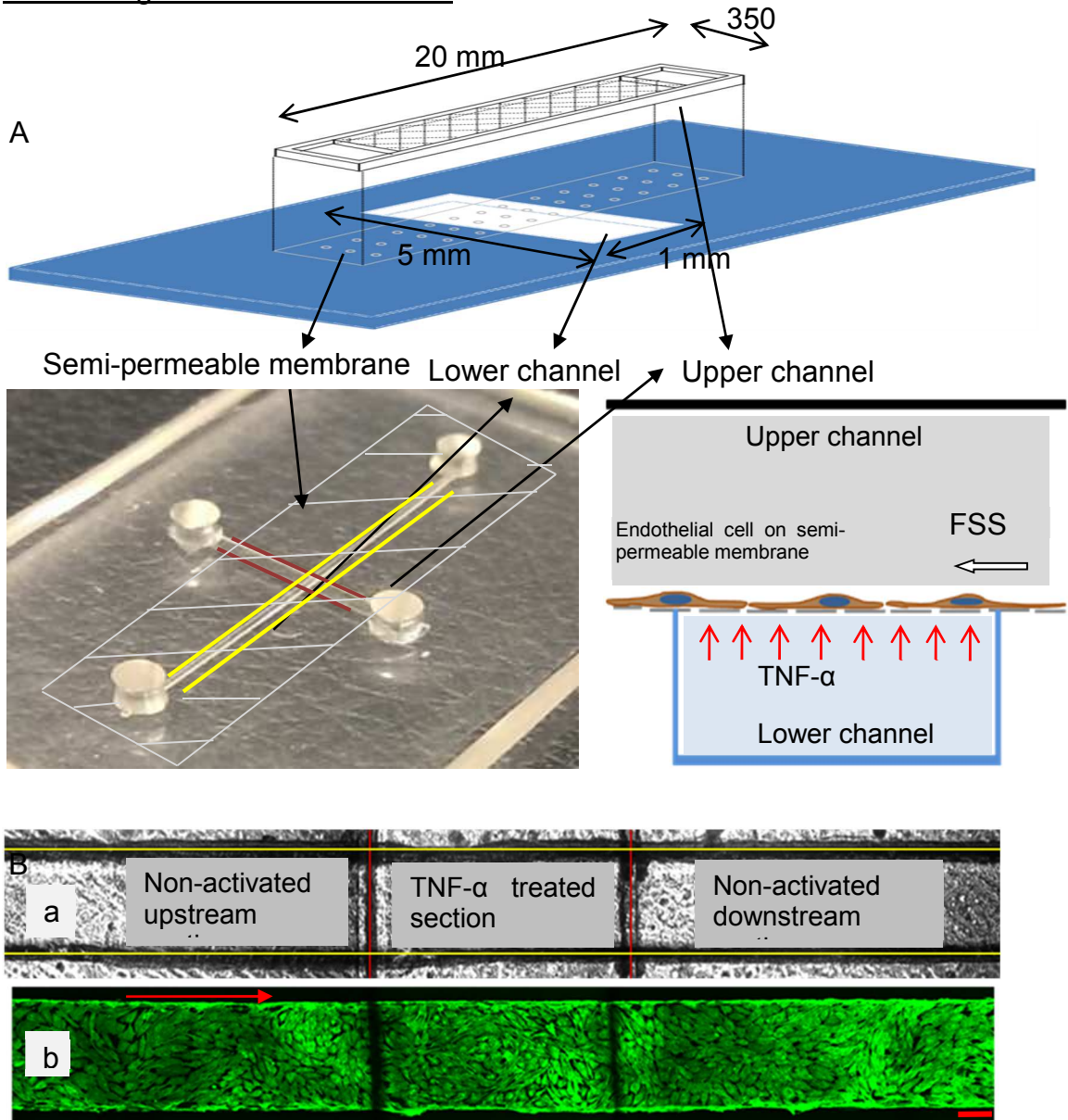


Figure 15: A, Graphical schematic (left) and photograph (center) of the bi-layer device showing the upper (marked with yellow lines) and lower (marked with red lines) channel separated by the semi-permeable membrane. Schematic on the extreme right depict endothelial cell growth on semi-permeable membrane and TNF- α treatment from the lower channel. B, (a) Bright field image of the top (marked with yellow lines) and bottom (marked with red lines) channel defining the upstream, TNF- α activated and downstream sections, (b) Fluorescence labeled actin cytoskeleton (FITC phalloidin) images of confluent BAOEC layer aligned to flow (12 dyne/cm² FSS for 24 hrs). The cells grow on the semi-permeable membrane in the top channel of the device. Arrow shows flow direction (Scale bar: 100 μ m)

The microfluidic device channels are made of PDMS and the upper channel is 20 mm long and has a width of 350 μm . The lower channel is 5 mm long and 1 mm wide and is arranged perpendicular to the top channel (Figure 15 A). The top channel is bonded to the bottom channel with the semipermeable membrane in between through O_2 plasma bonding and by applying liquid PDMS along the channel edges. The porous PC membrane is cell culture friendly and provides the base for cell growth and proliferation. Such membrane based mimicking of biological platforms has been widely demonstrated [110-111, 115-116]. Transport of materials between the upper and lower channels is limited to diffusion through the membrane pores. This allows for spatially controlled and independent transport between the channels without leakage.

5.3.2 On-chip cell culture

Endothelial cells are constantly exposed to blood flow as they form the 'tunica intima' or the inner coat of a blood vessel. The exposure of endothelial cells to this shear stress activates a number of cellular mechano-sensors, which along with adaptor molecules regulate the expression of genes and proteins relevant to endothelial cell functions in healthy and disease conditions [117-118]. Maintaining the quiescent phenotype of endothelial cells is critical to the success of a biomimetic blood vessel model and subjecting the endothelial cells to native *in vivo* FSS is important [119]. Pro-inflammatory and proliferative pathways of vascular endothelial cells become down-regulated when the endothelial cell layer is exposed to directed and sustained FSS [120]. To validate the bio-mimetic nature of our device, confluent layer of BAOECs were subjected to physiological levels of

FSS (12 dyne/cm²). BAOECs were exposed to steady and directed laminar FSS for a time period of 5 days to check the longevity of maintaining a confluent cell layer. Confluent and flow aligned BAOEC layer after 5 days looked similar to the F-actin stained illustrative image of BAOECs at 12 dyne/cm² FSS after 24 hrs in Figure 15 B (b), confirming the maintenance of a quiescent and sustaining phenotype by the BAOECs.

5.3.3 Endothelial cell alignment and stress fiber arrangement under FSS

To further examine the state of BAOECs under flow in our device, their actin assembly characteristics were studied. endothelial cells exposed to FSS undergo a change in cell shape and their microfilament network remodels and aligns to the direction of flow [121]. We examined this by staining F-actin stress fibers of BAOECs growing in the upper channel. The exposure of cells to flow at 12 dyne/cm² resulted in alteration of cell shape from the typical cobblestone pattern to fusiform as observed in endothelial cells *in vivo* [122-123]. The cells and their actin stress fibers were uniformly aligned in the direction of flow (

Figure 16B). The control (no flow) case had the F-actin fibers arranged in a radial pattern or emerging from the edges, a mechanism to maintain the cell well-spread (

Figure 16A). To better depict the relationship between cell orientation and flow direction, the angle (α) between the orientation of stress fibers and the width (short-axis) of the microchannel was plotted. It is observed that for the control case the

Stress fibers align at an average angle of 51.4° , while the cells exposed to flow show an average angle of 90.1° (

Figure 16C). This result is consistent with previous studies [121, 124].

The thickness of the cortical actin and width of stress fibers were calculated from the fluorescence labeled actin cytoskeleton images. In BAOECs subjected to 12 dyne/cm^2 of FSS for 4 hrs, the thick cortical actin was found to reorganize into actin stress fibers along the direction of flow (Figure 17). About ~ 2 fold decrease in thickness of cortical actin is observed (Figure 17 A). The width of stress fibers increases ~ 2 fold as well for BAOECs subjected to FSS (Figure 17 B). Previous works have identified JNK activity-dependent cortical actin remodeling into stress fibers when exposed to flow, allowing the cells to maintain their mechanical integrity and cell-cell contact [125].

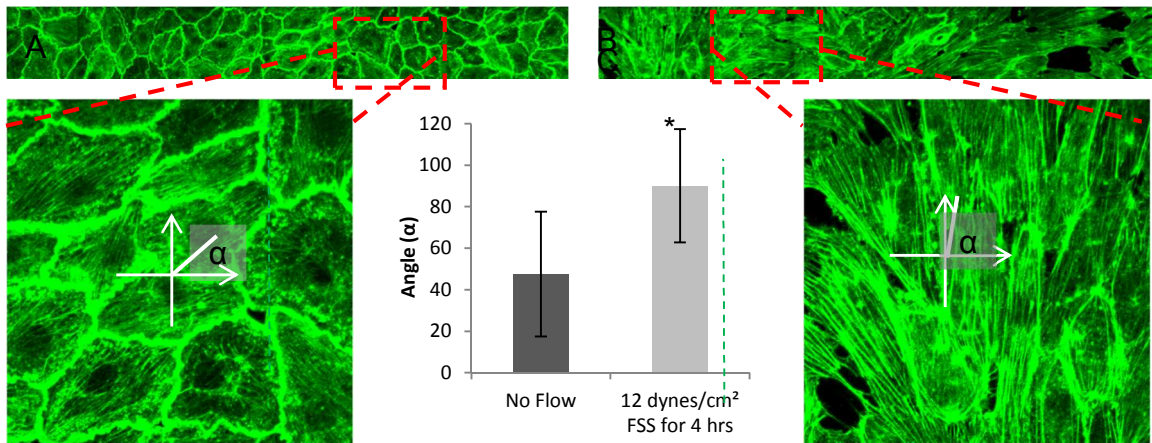


Figure 16: Organization of F-actin stress fibers (green) in BAOECs assessed by confocal microscopy (A) Static case; Cell stress fibers tend to align parallel to the width of the channel. (B) After 4 hrs of flow at 12 dyne/cm^2 FSS; Cell stress fibers tend to align parallel to the flow direction. Inserts show zoomed in images of stress fiber alignment. Arrow marks the flow direction. (C) Quantitative measurement of stress fiber alignment angle (α) to the width of the channel under static and flow shear stress case (* $p < 0.001$, ** $p < 0.0001$, *** $p < 0.00001$, by Student's t test)

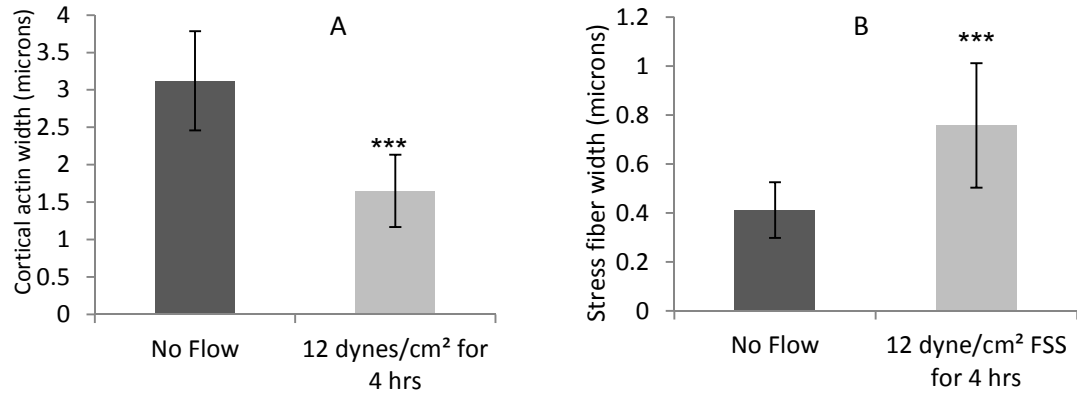


Figure 17: Reorganization of cortical actin into stress fibers in BAOECs subjected to FSS. Flow-induced actin remodeling was observed by fluorescence labeling of the actin cytoskeleton with FITC-conjugated phalloidin in BAOECs treated with 12 dyne/cm² FSS for 4 hrs. Comparison of (A) Cortical actin thickness; (B) Stress fiber width; distribution in static and flow (12 dyne/cm² FSS for 4 hrs) culture conditions. (*p<0.001, ** p<0.0001, *** p<0.00001, by Student's t test)

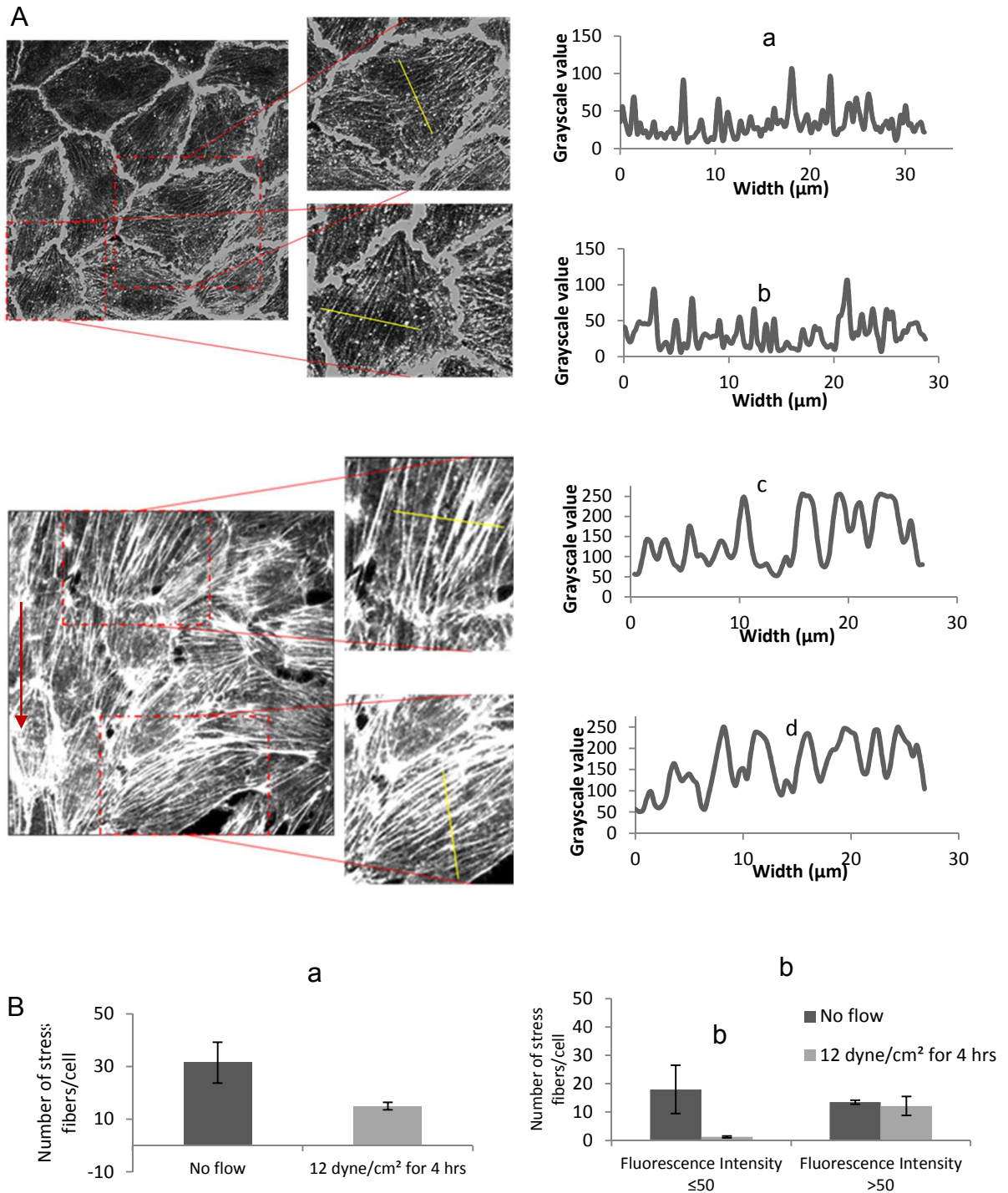


Figure 18: Comparison of stress fiber distribution in BAOECs subjected to FSS with no flow case. Actin stress fibers of BAOECs are labeled with FITC-conjugated phalloidin. (A), Fluorescence intensity (grayscale value) of stress fibers is quantified using ImageJ software across the marked line and corresponding line graphs are plotted for, (a,b) no flow (control) case; and (c,d) endothelial cells treated with 12 dyne/cm² FSS for 4 hrs. (B), (a) Total number of fluorescence intensity (grayscale value) peaks of stress fibers in control and flow case; (b) Thin and thick actin stress fibers were marked by classifying stress fibers based on grayscale value ≤ 50 as thin and >50 as thick in the BAOECs for both control and FSS case. Arrow indicates flow direct. (Scale bar: 10 μ m).

Since the actual aggregate of stress fibers cannot be understood from analyzing the width of the stress fibers alone (thickness of stress fibers in the z direction not considered), we quantified their fluorescence intensity in grayscale value and plotted the corresponding line graphs (Figure 18 A). This gives us an idea of stress fiber density present in the cell (Figure 18 B) as well. The exposure of endothelial cells to FSS organizes thick stress fibers along the direction of flow both *in situ* and *in vitro* [126]. We observe multiple but less intense stress fiber distribution across the cytoplasm of BAOECs for the no flow case based on fluorescence intensity [Figure 18 A, (a,b)]. BAOECs subjected to flow have fewer but more profound and sharp stress fiber distribution [Figure 18 A, (c,d)]. Stress fiber density in the cells was quantified by doing a line profile across the cytoplasm of BAOECs and using ImageJ software to calculate fluorescence intensity [127]. The software identifies stress fibers by their increased fluorescence relative to areas devoid of stress fibers. Sharp, distinct peaks represented individual stress fibers, while the width and fluorescence intensity of the peak indicated the thickness of a stress fiber [Figure 18 B, (a)]. Thin and thick actin stress fibers were quantified for both control and FSS cases by classifying stress fibers based on fluorescence intensity (grayscale value). For statistical purposes, stress fibers with fluorescence intensity ≤ 50 grayscale value were arbitrarily marked as thin and >50 as thick [Figure 18 B, (b)]. The no flow case has almost an equal distribution of thin and thick stress fibers, while the BAOECs subjected to FSS have a significant distribution of thick stress fibers in their cytoplasm. Laminar and sustained FSS induces thicker stress

fiber organization in endothelial cells along with the direction of flow along with maintaining elongated cell morphology.

5.4 Conclusion

By smart integration of biology and engineering it was possible to design a biomimetic blood vessel environment that combines microenvironmental control with cell specific transport and signalling. Endothelial cells were cultured under *in vivo* levels of flow, a more realistic and accurate environment as an intact endothelium is exposed to constant blood flow. These cells had access to an uninterrupted nutrient supply and could be triggered with external cues from the apical or basal side. We established the longevity of maintenance of a uniform monolayer of endothelial cells when cultured under flow to a minimum of at least 5 days. The F-actin stress fiber remodeling and arrangement pattern shift once subjected to FSS. There was a significant increase in the presence of stress fibers in the cell cytoplasm, oriented to the long axis of the cell and arranged parallel to each other once subjected to flow. The presence of cortical actin also diminished in the endothelial cells after exposing to FSS. This platform is to be used for characterizing the activation of endothelial microenvironment by studying the expression of surface ICAM-1 after local action of TNF- α , and also to study the dynamics of change in vascular permeability once triggered with thrombin, an acute blood vessel inflammatory mediator. These studies have been explained in the following chapters.

Chapter 6

Dynamics of endothelial activation by local action of pro-inflammatory cytokines

6.1 Introduction

The biological relevance of the conventional cell culture models is limited. Both understanding of pathophysiology and design of adequate interventions demand alternative bio-mimetic model platforms with intermediate ratios of feasibility/complexity, allowing researchers to more adequately address specific inquiries in the relevant context. We are combining endothelial microfluidics/flow adaptation approach with local cytokine application via a permeable “sub-endothelial compartment” and antibody-coated nanoparticles as imaging probes. This approach allowed us to define flow-mediated local heterogeneity of endothelial activation by cytokines that appears to reflect the pathophysiology of the process. Such pro-inflammatory processes are also symptomatic of enhanced endothelial permeability due to inter-cellular gap formation and this phenomenon has been characterized using fluorescent dye diffusion studies. Furthermore, the results of this study support design of drug delivery systems employing affinity nanocarriers targeted to the pathological endothelium.

Inflammatory conditions like rheumatoid arthritis, inflammatory bowel disease, asthma, chronic airway inflammation, atopic dermatitis, and psoriasis [20, 21]. as well as presence of foreign materials leads to the action of several inflammatory mediators (e.g., Vascular endothelial growth factor- (VEGF)-A, Tumor necrosis

factor- (TNF)- α , Interleukin- (IL)-6, and IL-1 β) on the blood vessel. This leads to an increase in vessel permeability and delivery of immunoglobulins, antiproteases, constituents of the complement and coagulation systems and other acute phase proteins to the site to act in local host defense and initiate tissue repair. Furthermore, the expression of adhesion molecules, such as intercellular adhesion molecule- (ICAM)-1, vascular cell adhesion molecule- (VCAM)-1, and E-selectin on activated blood vascular endothelial cells, induce neutrophil and monocyte infiltration which collectively increase the permeability of endothelial cell junctions [128-139]. Determining the underlying mechanism requires multidisciplinary approaches [140-141]. By understanding this we can engineer nanodrug carriers with optimized ligands and coating densities to facilitate trans-endothelial drug delivery with high efficacy at sites of inflammation [142].

An *in vitro* bio-mimetic blood vessel should be able to model *in vivo* physiological characteristics like pathological microenvironment, relevant flow dynamics and vessel shape dimensions. Microfluidic engineering enables integration of precisely controlled flow in channels, whose shape and dimensions can be designed to requirement with resolution limits in the micron scale. In the previous section details about the fabrication of the biomimetic blood vessel system and the characterization of endothelial cell growth in this device were presented. In this chapter TNF- α mediated ICAM-1 expression was produced in the endothelial cells and anti-ICAM-1 coated 210 nm and 1 μ m particles were used as imaging probes to characterize their presence under physiologically relevant conditions. Binding studies using ICAM-1 ab coated particles of different sizes and coating densities

under physiologically relevant flow conditions allowed investigation of spatial organization of ICAM-1 expression at different levels of detection sensitivity. This approach allowed us to study the dynamics of flow-mediated heterogeneous expression of ICAM-1 in endothelial microenvironments when locally activated. F-actin depolymerization and rearrangement were also found to occur in sections that were locally TNF- α triggered. The upregulated expression of surface ICAM-1 is evident and steady in the locally TNF- α treated region, but decreases along the length of the channel in the downstream section to match with the basal expression levels observed in the upstream regions. F-actin depolymerization and rearrangement also follows the same trend.

6.2 Methods

6.2.1 TNF- α treatment

BAOECs after being subjected to 24 hrs or more of flow at 12 dyne/cm² were treated with TNF- α to locally activate ICAM-1 expression on the endothelial cell layer. This treatment was performed on an 80-90% confluent cell layer. BAOECs were locally activated by introducing DMEM media containing 10 Units (U)/ml of TNF- α for 2 hrs in the lower channel of the device. A time course study on TNF- α based expression of surface ICAM-1 by BAOECs was performed and 2 hrs of treatment was found to be optimal (Figure 20). TNF- α diffuses through the semi-permeable pores of the membrane separating the lower from the upper channel and spatially controls the direct activation of BAOECs only present above the lower channel. BAOECs on the upstream or downstream sections of the upper channel with respect to the TNF- α treated region do not come in direct contact with the inflammatory cytokine. Here the BAOECs are cytokine treated from the basal side of the cell.

6.2.2 Binding of anti-ICAM-1 coated particles on BAOEC layer

A particle binding study was performed on TNF- α activated live BAOECs in a continuous manner by introducing particles at their respective concentrations for designated flow times (Table 4) without stopping the flow and while TNF- α activation of endothelial cells is still conducted from the lower channel. This keeps the targeted drug carrier binding study set-up as close to native, *in vivo* condition as possible and maintains a stable endothelial cell niche microenvironment.

Table 3: Final particle concentration (#/ml) for 210 nm and 1 μm particles. The total particle volume is constant for both particles

Particle size	Final particle concentration	Total particle volume (μm^3)
210 nm	$4.77 * 10^9/\text{ml}$	20000000
1 micron	$3.85 * 10^7/\text{ml}$	20000000

Table 4: FSS and corresponding volumetric flow rate values along with flow time for 6, 12 and 18 dyne/cm^2 cases. Flow time decreases with FSS to maintain the 'total number of particles/flow case' a constant

Flow shear stress (dyne/cm^2)	Flow rate in ml/hr (viscosity: 0.007 $\text{dyne sec}/\text{cm}^2$ for media)	Flow time (minutes) for particle flow study in media/pure buffer
6	1.8	6
12	3.6	4
18	5.4	2

The particle working concentrations for performing binding test of 210 nm and 1 μm particles were chosen such that the total volume of particles remained a constant (Table 3). Also, in order to make sure the 'total number of particles/flow case' remains a constant for all particle binding FSS cases, the flow time decreased with an increase in FSS (Table 4). This maintains the total volume of particle solution in all cases the same.

The particles were infused into the upper channel of the device and after their designated flow time unbound particles were removed by flushing with a buffer solution. The wash buffer contains a plasma membrane stain (CellMask™, Life technologies) to fluorescently tag the BAOECs. The particle bound BAOECs are then fixed in paraformaldehyde (3.7%). Particle binding is analyzed by phase contrast and fluorescence microscopy (FV1000-IX81, Olympus) and image analysis was performed using ImageJ software.

6.2.3 Preparation and characterization of anti-ICAM-1 coated particles

Neutravidin coated 210 nm and 1 μm fluorescent particles (Invitrogen Corp.) were diluted to 10^{10} and 10^9 particles/ml respectively using BlockAid™ solution (Invitrogen Corp.) and sonicated. Biotinylated Protein G (29988, Thermo Scientific) diluted in 1% BSA solution was bound to the NeutrAvidin coating on the particles initially. This is followed by binding ICAM-1/Control IgG (or both) antibody (NB500-318, Novus Biologicals) with specificity for bovine cells to the Protein G coated particles. The particles were incubated for 12 hrs on a shaker at 4°C for both coating steps and the unbound protein G/antibody was removed by centrifugation. The particles were also washed in 1% BSA solution to remove any leftover unbound protein G/antibody, and finally the particles were diluted to their respective working concentrations (Table 1). The concentration of the particles available was analyzed on a microplate reader at 485 nm excitation/530 nm emission and compared to a calibration curve constructed from stock particle solution.

The anti-ICAM-1 coating density on the particle was determined using ELISA. 210 nm particles were conjugated with anti-ICAM-1 at 100% (possible maximum) and 50% of coating density, while 1 μ m particles only had the maximum antibody coating density case. ELISA was performed using an HRP conjugated anti-mouse k-light chain specific monoclonal antibody to characterize the particle surface antibody density for both micro/nano particles. The specificity of the reagent to mouse antibody light chains provides a direct measurement of the anti-ICAM-1 binding sites available on the particle. Particles were incubated with 5% HRP conjugated anti-mouse k-light chain specific monoclonal antibody for 30 minutes, followed by washing with 1% BSA solution and clearing out of unbound antibody through centrifugation. 50 μ l of the particle solution were loaded on a 96-well plate and the particle concentration was analyzed. Then 50 μ L of Amplex Ultra Red reagent was added to each wells and the reaction was allowed to proceed for 10 minutes at room temperature. The fluorescence intensity of the particle sample with Amplex Ultra Red reagent was observed on a microplate reader at 544 nm excitation/590 nm emission. The fluorescence intensities were converted to the number of HRP molecule using the calibration curves prepared using biotinylated-HRP conjugation. Assuming a 1:1 binding ratio between anti-ICAM-1 and secondary antibody, the anti-ICAM-1 density on the particles were determined. 210 nm and 1 μ m particle antibody coating density based on fluorescence intensity was compared to estimate the relative accuracy of the technique.

Complete saturation of anti-ICAM-1 coating on 210 nm particles produced 232.5 ± 25 anti-ICAM-1/particle and this was brought down to 112.9 ± 19 anti-ICAM-

1/particle as well using control IgG antibody. These correspond to $1851.2 \pm 199/\mu\text{m}^2$ for the maximum antibody density case and 898.9 ± 151 anti-ICAM-1/ μm^2 respectively. $1 \mu\text{m}$ particles have an antibody density of 2367.8 ± 264 anti-ICAM-1/particle which corresponds to 232.9 ± 25 anti-ICAM-1/ μm^2 .

6.3 Results and Discussion

6.3.1 Targeted binding of anti-ICAM-1 coated particles on BAOEC layer

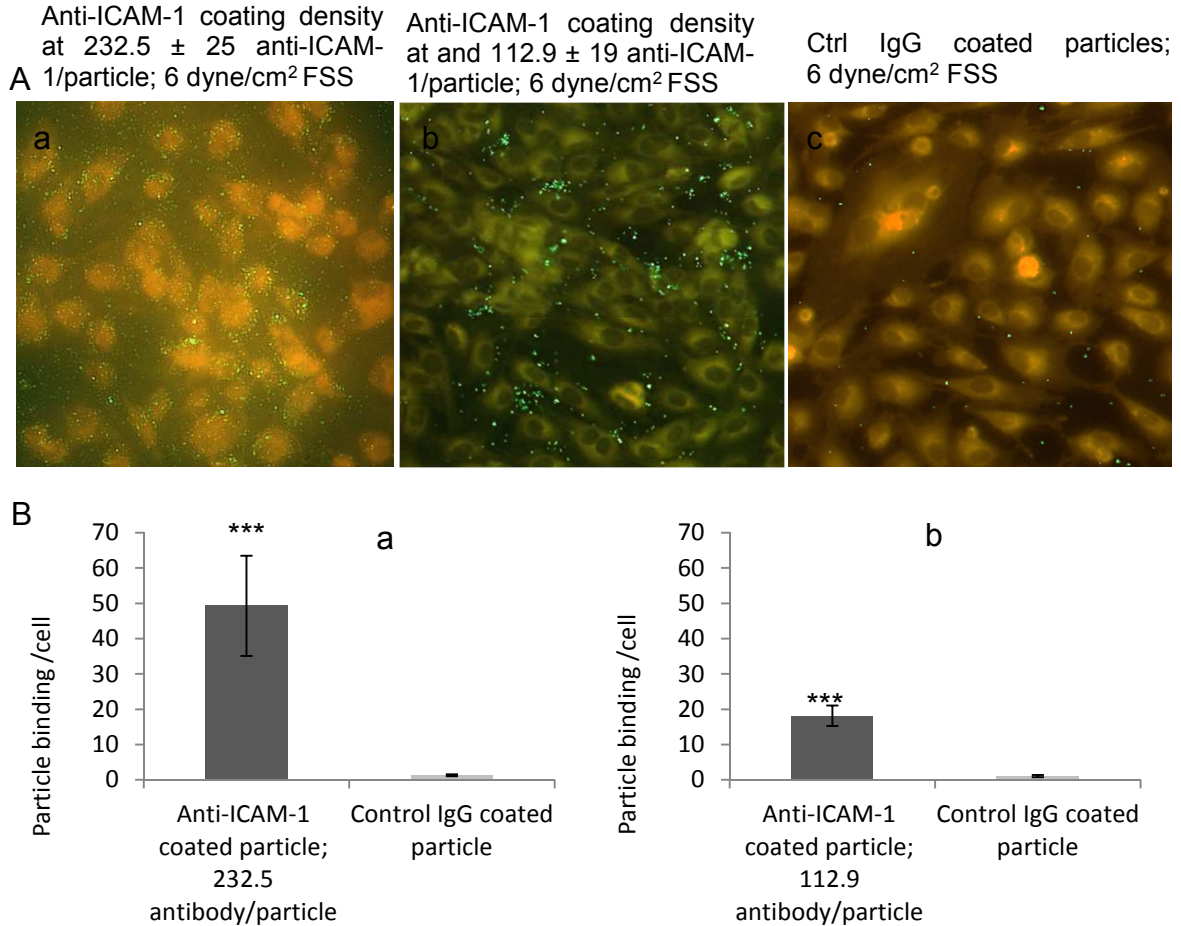


Figure 19: Binding of Anti-ICAM-1/Control IgG coated 210 nm particles on BAOECs under flow. A, Fluorescence micrographs show binding of particles to TNF- α activated BAOECs under different conditions, (a) Anti-ICAM-1 coated particles with a density of $\sim 1900/\mu\text{m}^2$ (~ 230 molecules/particle) at FSS of 6 dyne/cm²; (b) Anti-ICAM-1 coated particles with a density of $\sim 1000/\mu\text{m}^2$ (~ 110 molecules/particle) at FSS of 6 dyne/cm²; (c) Control IgG coated particles at FSS of 6 dyne/cm². (Scale bar: 20 μm). B, Quantification of anti-ICAM-1 and control IgG coated particle binding per cell at FSS of 6 dyne/cm² on TNF- α activated BAOECs, (a) Anti-ICAM-1 coated particles with a density of $\sim 1900/\mu\text{m}^2$ (~ 230 molecules/particle) and Control IgG coated particles; (b) Anti-ICAM-1 coated particles with a density of $\sim 1000/\mu\text{m}^2$ (~ 110 molecules/particle) and Control IgG coated particles. (* $p < 0.001$, ** $p < 0.0001$, *** $p < 0.00001$, by Student's t test)

TNF- α activated BAOECs would have upregulated expression of ICAM-1 among other endothelial cell surface proteins [143]. A time course study on TNF- α based expression of surface ICAM-1 by BAOECs cultured in petri-dish showed 2 hrs of treatment to be optimal (Figure 20). The BAOECs are cytokine-treated from the basal side of the cell. To understand the difference in basal and apical cell side TNF- α treatment on surface ICAM-1 expression, BAOECs were subjected to these two cases separately. The cells expressed similar levels of ICAM-1 expression for both cases characterized by targeted particle binding (Figure 21). In our work, the ICAM-1 expression was evaluated by studying specific binding of anti-ICAM-1 coated particles to endothelial cells in the upper channel. 210 nm nanoparticles coated with anti-ICAM-1 or control IgG were perfused at 6 dyne/cm² FSS. Anti-ICAM-1 coated NP bound to cytokine-activated endothelial cell specifically, exceeded binding of control IgG coated NP by ~20 times and ~50 times when coated by anti-ICAM at 112.9 ± 19 and 232.5 ± 25 antibody/particle, respectively ($p < 0.00001$) (Figure 19). Anti-ICAM-1 coated NP binding to TNF- α treated endothelial cell was further enhanced in FSS-exposed compared to static endothelial cells, consistent with observations in other models [144] (Figure 19 vs. Figure 20)

6.3.2 Time course study on TNF- α based expression of surface ICAM-1 by BAOECs under static culture condition

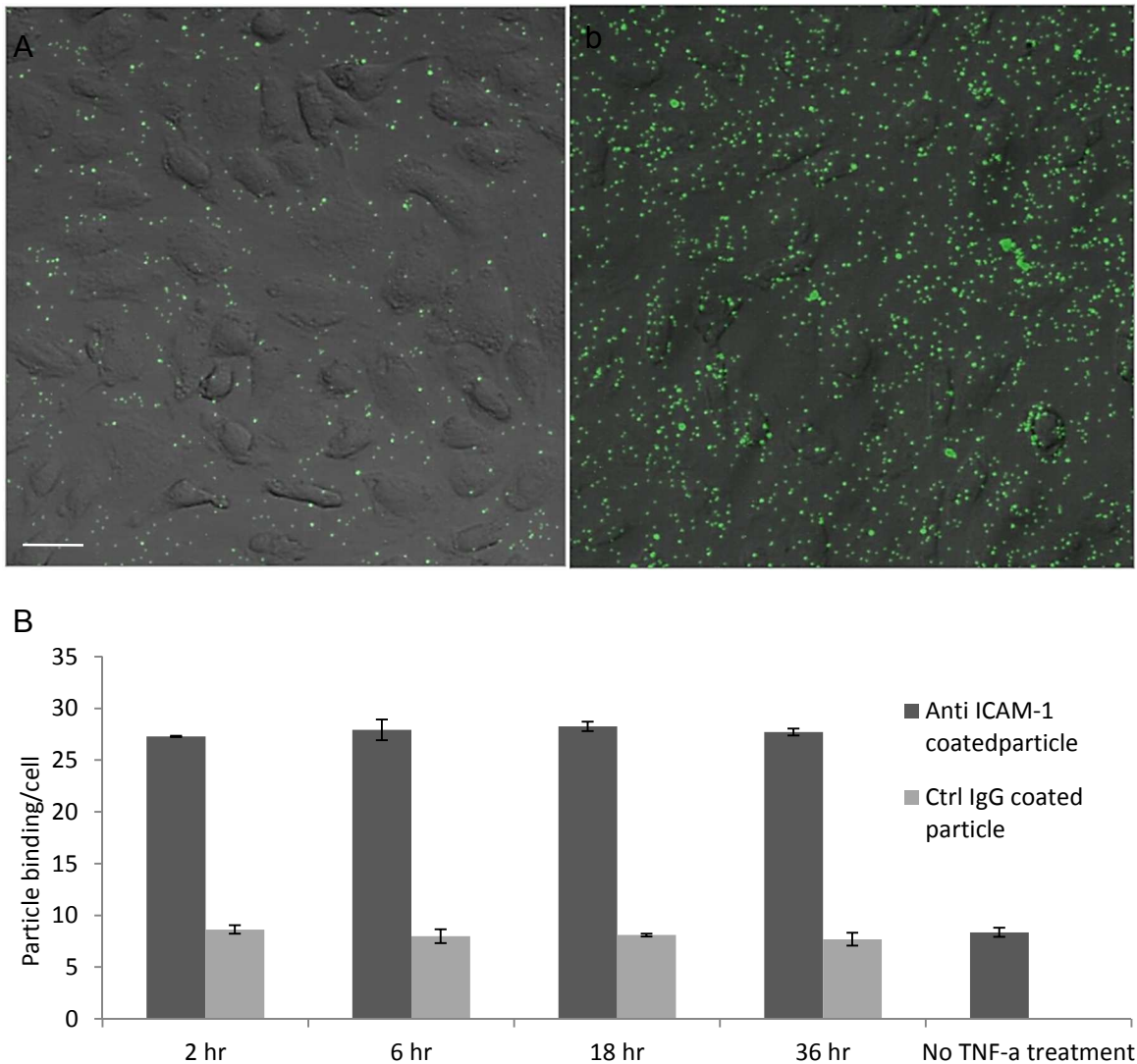


Figure 20: Binding of Anti-ICAM-1/Control IgG coated 210 nm particles on BAOECs cultured in a petri dish. A, Fluorescence micrographs show binding of particles to 2 hr TNF- α (10 U/ml) activated BAOECs, (a) Anti-ICAM-1 coated particles with a density 232.5 anti ICAM-1/particle; (b) Control IgG coated particles. (Scale bar: 20 μ m). B, Quantification of anti-ICAM-1 and control IgG coated particle binding per cell on TNF- α activated and control BAOECs.

6.3.3 BAOECs treated with TNF- α from the basal and apical side of the cell

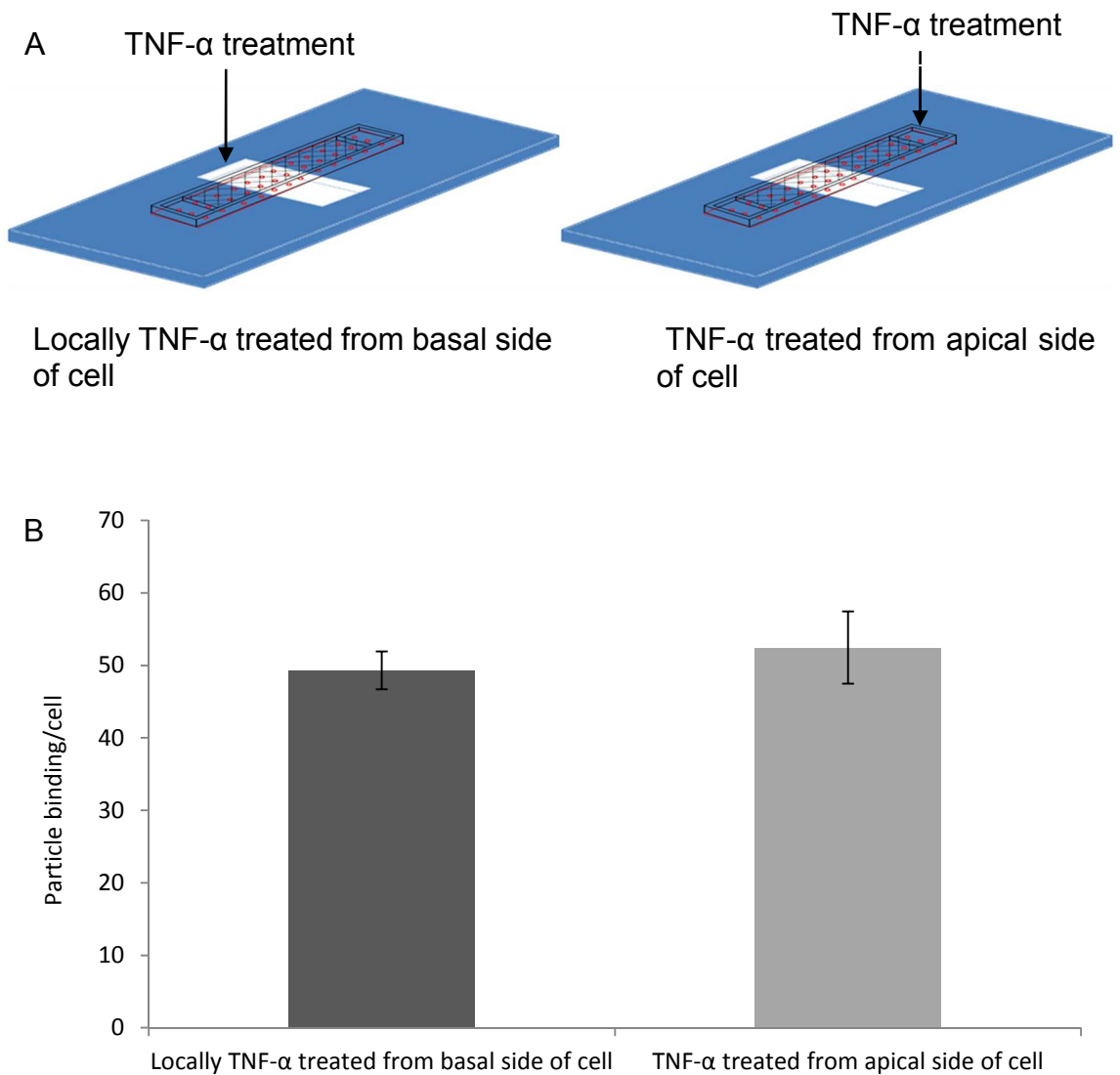


Figure 21: Binding of anti-ICAM-1 coated 210 nm particles (232.5 anti ICAM-1/particle) on BAOECs treated with TNF- α (10U/ml) from the basal and apical side of the cell, (A) Schematic illustrating the TNF- α treatment procedure; (B) Particle binding/cell quantification of anti-ICAM-1 coated 210 nm particles (232.5 anti ICAM-1/particle) on ICAM-1 expressing BAOECs. (n=100 cells from three independent experiment for each case)

6.3.4 Characterization of flow-mediated localized BAOEC activation using fluorescent probes

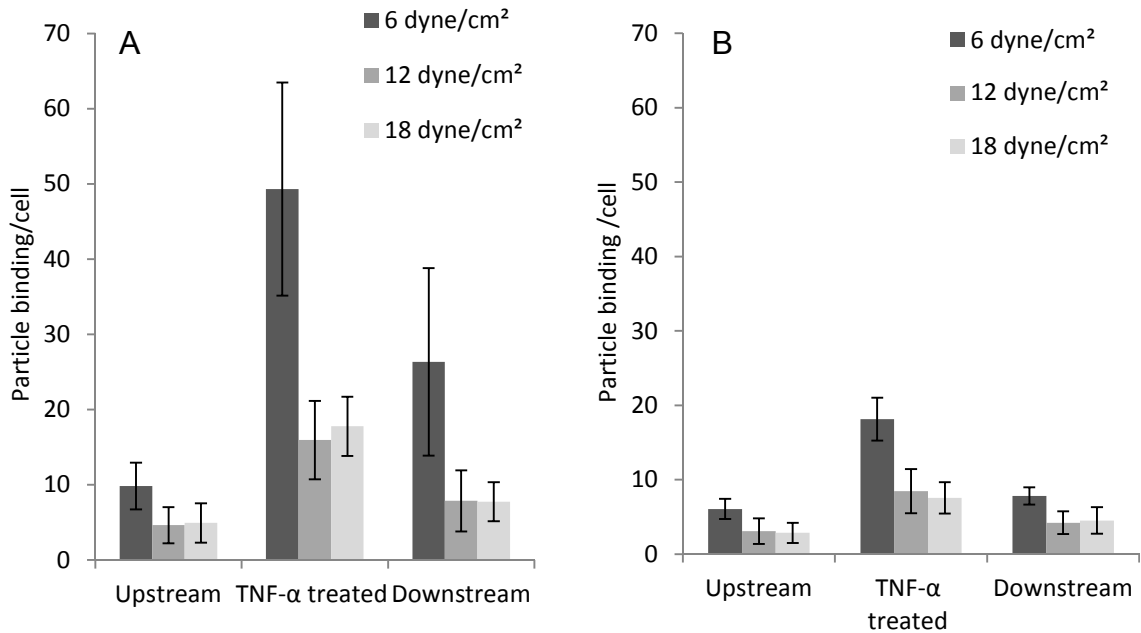


Figure 22: Targeted binding of anti-ICAM-1 coated particles of different antibody coating density on BAOECs in the upstream, TNF- α treated and downstream sections of the channel at different shear rates. Quantification of particle binding density per cell at 6, 12 and 18 dyne/cm² for 210 nm particles with A, anti-ICAM-1 coating density of 232.5 ± 25 anti-ICAM-1/particle and B, anti-ICAM-1 coating density of 112.9 ± 19 anti-ICAM-1/particle. Data are shown as mean \pm S.D. (n=50 cells). $p < 0.01$ by one way ANOVA test for particle binding data compared between upstream, TNF- α treated and downstream regions for both 232.5 ± 25 and 112.9 ± 19 anti-ICAM-1/particle cases.

The design of our bio-mimetic blood vessel platform allows a section of the upper channel to be accessed independently. This facilitates spatially controlled cytokine activation of endothelial cells. Having both direct cytokine-activated and non-activated endothelial cells in the same channel allowed investigation of the heterogeneous nature of ICAM-1 expression and the hemodynamic control of the marginal zone between inflammation foci and relatively normal vasculature. Investigating the binding of anti-ICAM-1 coated particles of different size and

antibody coating densities to ICAM-1 under physiologically relevant FSS characterizes the distribution and accessibility of ICAM-1 on endothelial cells. Such studies can shed light on parameters involved in receptor-ligand recognition for activated blood cells and affinity drug carriers.

As the endothelial cells were fluorescently tagged, the boundaries of individual cells were marked and the number of particles binding per cell was counted using ImageJ software. The binding of fluorescent particles to ICAM-1 in the upstream, TNF- α treated and downstream areas of the channel was studied using antibody coated 210 nm and 1 μ m particles. Flow rates of 6, 12 and 18 dyne/cm² were employed after the BAOECs were treated with TNF- α for 2 hrs under a steady and sustained FSS of 12 dyne/cm².

BAOECs in the TNF- α treated section of the upper channel have around 4-5 times higher particle binding density compared to the upstream section for 210 nm particle with a coating density of 232.5 ± 25 anti-ICAM-1/particle (Figure 22 B) ($p < 0.01$). A similar trend was observed for the lower antibody coating density case (Figure 22 A) and this was consistent for all the flow cases for both particle antibody coating densities. This clearly showed a significant increase in surface ICAM-1 expression in BAOECs at the TNF- α treated section. The p value is < 0.01 by one way ANOVA test for particle binding data compared between TNF- α treated, upstream and downstream regions for both 210 nm particle antibody coating density cases. The downstream section of the channel also showed significantly higher (around 2 times) particle binding density compared to the upstream section ($p < 0.01$).

The particle binding density depends on the antibody coating density. When compared to the 232.5 ± 25 anti-ICAM-1/particle case, the particle binding density was around half for the 112.9 ± 19 / anti-ICAM-1 particle case. Previous studies have reported the binding kinetics of particles with higher anti-ICAM-1 coating density to be significantly faster [145-146]. This increased binding density of particles with higher antibody coating is consistent with other studies and our previous work [68, 145]. The particle binding density decreased when the FSS increased from 6 to 12 dyne/cm² for both anti-ICAM-1 coating density cases. An increase in FSS reduced the available time for particles to diffuse/marginate towards the endothelial cell surface, which reduced their binding density [145]. The particle binding density also doesn't reduce for FSS > 12 dyne/cm² (Figure 22). Similar behavior has been reported in previous studies where it is observed that flow can't generate enough drag force on the particle to significantly reduce the particle binding density after a critical shear rate [145]. Here the receptor-ligand bond strength between the 210 nm particle and the ICAM-1 molecules expressed on the endothelial layer should be higher than the drag force produced by the FSS on the nanometer scale particle (drag force generated is proportional to the size of the particle).

Binding of anti-ICAM-1 coated 1 μ m particles was also studied, but no significant binding was observed in any sections of the channel for a FSS range of 6-18 dyne/cm². Particle binding characteristics similar to that of 210 nm ones were observed when the FSS was brought down to 1.5 dyne/cm² (Figure 24). Drag force generated on the bigger 1 μ m particle is higher, making them easily detachable. In

addition, the role of accessibility and surface congruency of ICAM-1 is more limiting for large vs small ligand-coated particles.

6.3.5 ICAM-1 and F-actin distribution pattern along the channel length

In order to study the transition in ICAM-1 expression in the different sections (upstream, TNF- α treated and downstream) of the channel, we divided these sections into smaller segments and inspected the particle binding per cell along the length of the channel (Figure 23 B). An increase in particle binding density as a result of ICAM-1 expression by BAOECs was first observed in the upstream section of the channel very close to the TNF- α treated section (red lines mark the boundary in Figure 23A and B). Elevated particle binding density was observed all along the 1 mm long TNF- α treated section and extended into the nearby downstream regions. Particle binding density in the downstream section was significantly higher than that of the upstream section even though both sections were not TNF- α treated directly. There was a smooth decrease in particle binding along the channel length in the downstream section and after a channel length of about 3 mm the particle binding density became comparable to that of the upstream region. TNF- α treatment leads to cell-cell barrier dysfunction and intercellular gap formation in endothelial cells, thus increasing blood vessel permeability [147-149]. The increase in particle binding in the upstream section close to the TNF- α treated section and along the length of the downstream section could be due to a synergistic influence of flow and TNF- α diffusion through the BAOEC layer which has increased permeability in the TNF- α treated region. Flow directed from the TNF- α treated to the downstream section carried a majority of

the diffused TNF- α molecules towards the downstream section. The exposure to TNF- α led to upregulation of ICAM-1 expression on BAOECs here, which decayed along the channel length as the distance from direct TNF- α exposure increased and endothelial cells in its path bound remaining TNF- α .

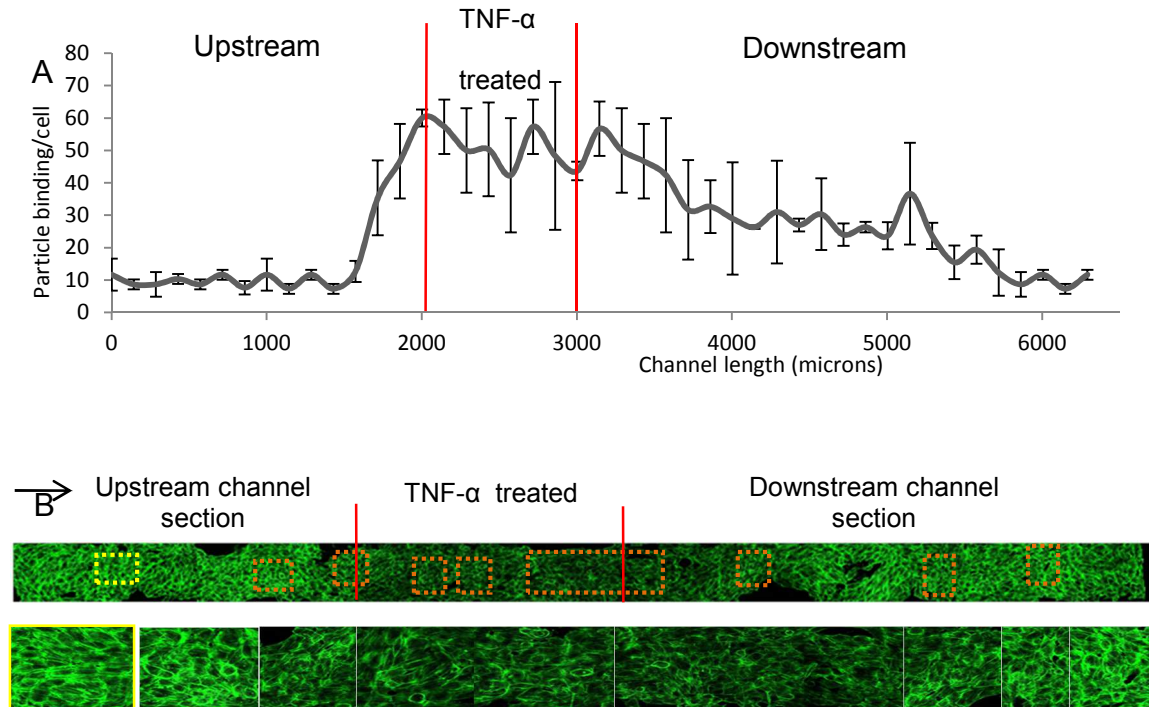


Figure 23: Analysis of particle binding and F-actin stress fiber arrangement along the length of the channel after TNF- α treatment. A, Particle binding per cell at 6 dyne/cm² FSS along the length of the channel divided into upstream, TNF- α treated and downstream sections. Data are shown as mean \pm S.D. B, F-actin stained image of BAOECs aligned to FSS at 12 dyne/cm² for 4 hrs and TNF- α treated for 2 hrs at 10 U/ml. Zoomed in images (corresponding to dashed boxes) give better understanding of F-actin arrangement. Yellow bordered image represents control BAOECs flow aligned to 12 dyne/cm² FSS. Dashed boxes and magnified images are arranged in the same order. Arrow indicates flow direction. (Scale bar: 100 μ m)

Inflammatory conditions lead to rearrangement of the actin cytoskeleton at endothelial cell junctions, regulation of endothelial permeability and barrier modulation [150-153]. We looked into F-actin stress fiber arrangement after TNF-

α treatment along the channel length to further understand the endothelial cell microenvironment (Figure 23 B). A confluent BAOEC layer was exposed to 4 hrs of FSS at 12 dyne/cm², which was followed by 2 hrs of localized TNF- α treatment (10 U/ml) from the lower channel. The cells were stained for F-actin stress fibers and their arrangement was studied in the upstream, TNF- α treated and downstream sections. BAOECs exposed to FSS in the upstream section had stress fibers aligned to flow direction (yellow bordered image in Figure 23 B). After 2 hr exposure to TNF- α , there was a thinning of stress fiber filaments in the central area of the cell cytoplasm. This thinning started around the border of upstream and TNF- α treated sections. It was consistently observed all throughout the TNF- α treated section and continued towards the downstream section. The F-actin stress fiber thickness in the cell center increased smoothly to levels comparable to the upstream section after about 1 mm length in the downstream section. The thinning in F-actin fibers was likely due to TNF- α induced F-actin remodeling observed in endothelial cells [147]. Rearrangement in F-actin stress fibers is also observed in BAOECs after TNF- α treatment. These isolated disruptions of the F-actin lattice were sparsely observed in the upstream regions close to TNF- α treated section, while they were more common in the TNF- α treated section. This was observed in the downstream section as well but the frequency of occurrence decreased along the channel length. This rearrangement of F-actin is a good indicator of barrier dysfunction and intercellular gap formation as a result of TNF- α treatment [147-149], which is consistent with our assumption of TNF- α diffusion to the upper channel from the lower channel.

6.3.6 Targeted binding of anti-ICAM-1 coated particles of 1 micron size on flow aligned BAOECs

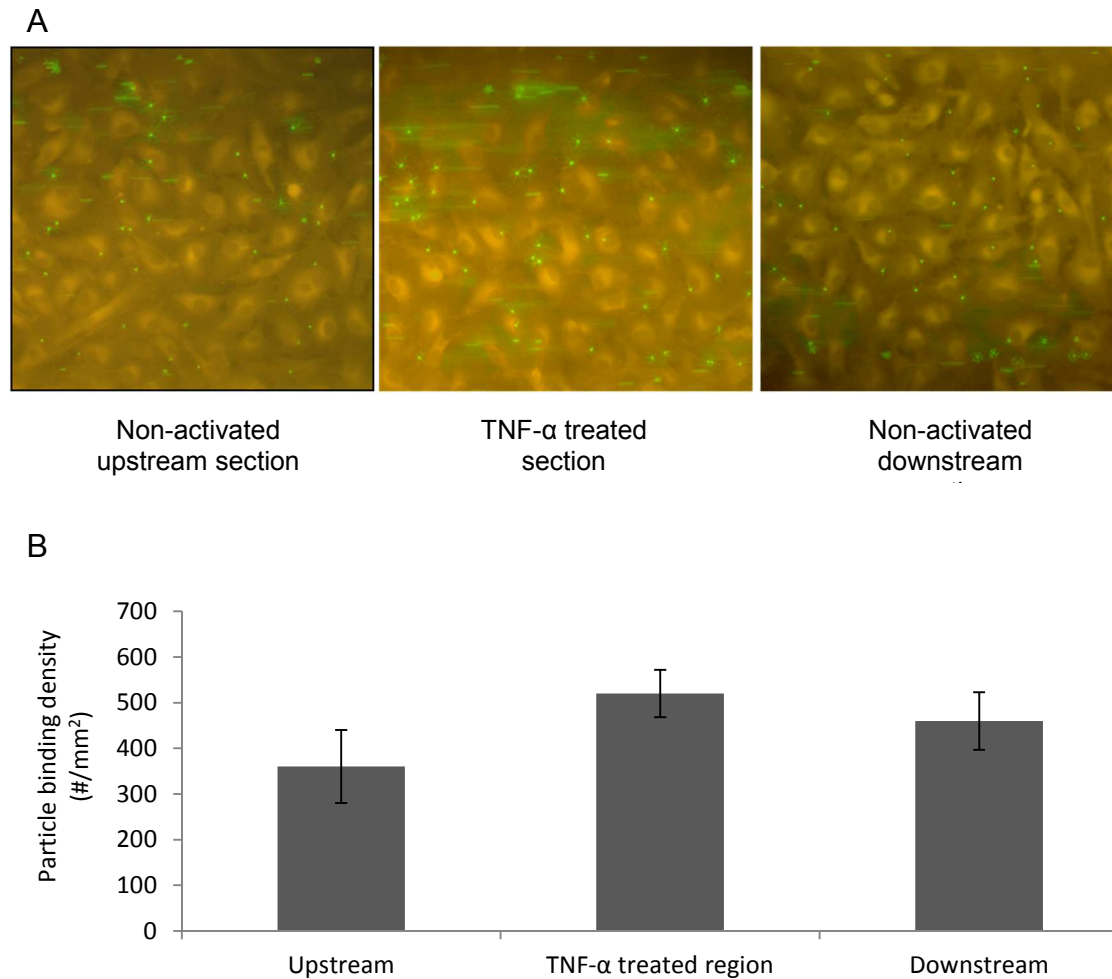


Figure 24: Targeted binding of anti-ICAM-1 coated particles of 1 micron size on flow aligned BAOECs in the upstream, TNF- α treated and downstream sections of the channel at 1.5 dyne/cm². A, Fluorescence micrographs show binding of particles on TNF- α activated BAOECs. B, Quantification of particle binding density per area at 1.5 dyne/cm² for 1 μ m particles with anti-ICAM-1 coating density of \sim 1500/ μ m²

6.3.7 Dynamic nature of surface ICAM-1 expression by endothelial cells

The biomimetic blood vessel microfluidic model has a closed design and this allows the maintenance of cell culture friendly conditions inside the channel to sustain cell growth outside an incubator. By mounting the required experimental set-up on a microscope table (Figure 25 A), real time *in situ* studies can be performed on our blood vessel model. We applied this to study the dynamics of endothelial surface ICAM-1 expression induced by flow mediated TNF- α activation. The dynamics were characterized by studying the specific binding of anti-ICAM-1 coated 210 nm fluorescent particles (232.5 ± 25 anti-ICAM-1/particle) on BAOECs activated locally with TNF- α . The device with a monolayer of flow aligned endothelial cells in the upper channel was mounted on the microscope table and subjected to a FSS of 12 dyne/cm² for 6 hrs before being locally TNF- α treated from the lower channel for 4 hrs. Anti-ICAM-1 coated particles were introduced to the flow and images were taken every 20 minutes to analyze the increase in particle binding on cell surface. The particle binding density per cell increased corresponding to an upregulation of ICAM-1 expression by BAOECs. This study provides a better understanding of the dynamics of ICAM-1 upregulation by BAOECs over time. Unlike that observed in static petri-dish studies where the ICAM-1 upregulation peaked after 2 hrs (Figure 20), this *in situ* observation under FSS showed a linear increase in ICAM-1 upregulation which peaked after 3 hrs and 20 minutes (Figure 25 C). The increased ICAM-1 expression in this case was a combined effect of flow and cytokine activation, as one could expect *in vivo*. This study provides a better understanding of the transient nature of ICAM-1 receptor

upregulation by BAOECs when locally activated by TNF- α in a flow-mediated realistic environment.

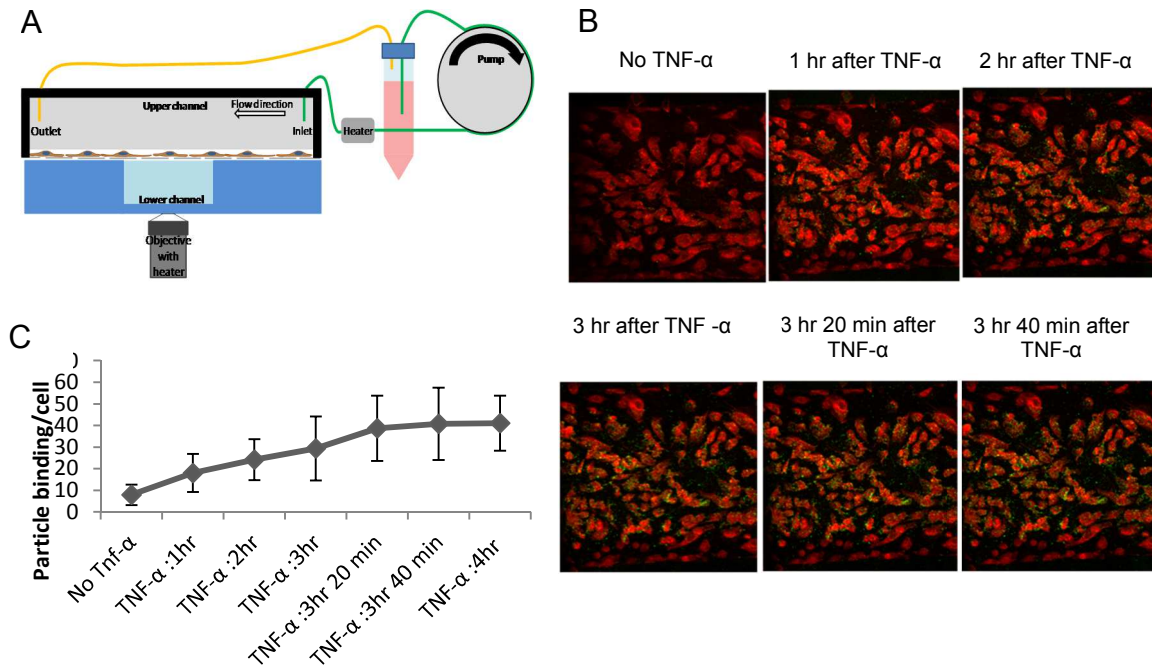


Figure 25: (A) Illustration of the real time particle binding study system on live cells. 210 nm particle binding per cell data over time to characterize surface ICAM-1 expression by BAOECs. (B) Images of 210 nm (green fluorescence) particle binding over stained (red) cells for different time points; (C) Particle binding per cell data for BAOECs before and after TNF- α over time.

6.4 Conclusion

The biomimetic blood vessel model in this study is a tool with unprecedented ability to investigate the microenvironment of endothelial cells. The microfluidic chip can mimic a close to native environment for endothelial cells by facilitating *in vivo* levels of flow and biomolecule supply, along with an opening for localized access. We characterized BAOEC culture under physiological levels of flow and analyzed their F-actin organization pattern. Localized TNF- α treatment was performed on the BAOECs from the lower channel and ICAM-1 upregulation in the upstream, TNF- α treated and downstream section of the channels was analyzed. We utilized this platform to perform targeted drug delivery by characterizing particle binding per cell for a FSS range of 6-18 dyne/cm² using 210 nm particles. The novelty of this device revealed that BAOECs in the downstream section of a channel express higher ICAM-1 compared to the upstream section. By analyzing the particle binding along the length of the channel we characterized the nature of upregulation and fall in ICAM-1 expression for BAOECs from the upstream to TNF- α treated and downstream channel sections. We also outlined the nature of TNF- α based actin depolymerization and rearrangement along channel length. This work highlights the versatile nature and functionality of the microfluidic

Chapter 7

Characterizing vascular permeability using a biomimetic microfluidic blood vessel model

7.1 Introduction

7.1.1 Vascular permeability and pathological significance

Blood vessels are permeable, which allows for transportation of small molecules such as water, ions, nutrients, even a whole cell across vessels. This capability is called vessel permeability [154]. Endothelial cells line the blood vessel lumen and form a semi-permeable barrier through cell-cell conjunction. This basal level vascular permeability is essential in the selective transport between blood and the interstitial space of all organs. Such permeability barrier is maintained through tight cell-cell junctions and is controlled by growth factors, cytokines and other stress related molecules [155]. Disruptions in the endothelial cell layer barrier can result in increased permeability. The permeability of blood vessels increase on detection of a potentially harmful substance, foreign organism, or injured tissue cells, to supply plasma proteins to the extravascular compartment in need of repair. This is mediated by several inflammatory mediators (e.g., Vascular endothelial growth factor- (VEGF)-A, TNF- α , Interleukin- (IL)-6, IL-1 β and thrombin delivers immunoglobulins, antiproteases, constituents of the complement and coagulation systems and other acute phase proteins to the site to act in local host defense and initiate tissue repair. Furthermore, the expression of adhesion molecules such as

ICAM-1, vascular cell adhesion molecule- (VCAM-)1, and E-selectin on activated blood vascular endothelial cells, induce neutrophil and monocyte infiltration which collectively increase the permeability of endothelial cell junctions [128-139]. These effects are observed as part of various disease states, and the understanding of the underlying mechanism requires multidisciplinary approaches [140-141]. Characterizing permeability of the endothelial cells that form the inner layer of blood vessels provides fundamental physiological information and is essential for evaluating drug and other biomolecule uptake. By understanding this we can engineer nanodrug carriers with optimized ligands and coating densities to facilitate trans-endothelial drug delivery with high efficacy at sites of inflammation [142].

7.1.2 Associated diseases

Vascular disruption and vessel leak is a common feature of acute and chronic injury and diseases such as atherosclerosis. Increased arterial endothelial cell permeability is considered an initial step in atherosclerosis [156-157]. In fact, atherosclerosis shows heterogeneous spotty leaky sites along healthy vessel [158]. During tumor growth, some unique pathophysiological characteristics that are not observed in normal tissues or organs are present, such as extensive angiogenesis and hence hypervascularity, defective vascular architecture, impaired lymphatic drainage/recovery system, and greatly increased production of a number of permeability mediators. This leads to higher pressure inside tumors. While the interstitial fluid pressure (IFP) in normal tissues is actively controlled and remains close to atmospheric levels, IFP in most human tumors is highly

elevated [159]. Getting chemotherapy agents into solid tumors can be a challenge because of high fluid pressure. Various other disease conditions also exhibit inflammation and increased vascular permeability as symptoms. In diabetes, hypoxic environment upregulated VEGF expression induces further elevated vascular permeability. Increased permeability of fluid and protein can lead to diabetic macular edema [160]. Other inflammatory conditions like rheumatoid arthritis, inflammatory bowel disease, asthma, chronic airway inflammation, atopic dermatitis, and psoriasis are also characterized by similar signs of inflammation [20, 21]. A better understanding of the dynamic nature of increase in vascular permeability and the peptide moieties involved can improve the ability to specifically target these sites to deliver drugs.

7.1.3 Dynamic nature of vessel permeability

Vascular permeability is a dynamic process. The processes are mediated by acute or chronic exposure to vascular permeabilizing agents, particularly vascular permeability factor/ VEGF, VEGF-A [161]. Experimental work has demonstrated that there are three patterns of increased leakage of fluid from vessels on three different times after injury. After endothelium exposure to histamine or thrombin a transient immediate and acute response can last for 30-60 minutes. A second response would happen 2-3 h after injury and lasts for up to 8 h. Local cells synthesize prostaglandins and platelet activating factors and mediate this response. If there has been some direct necrosis of the endothelium, a prolonged immediate response would occur over 24 h. In natural diseases all three responses may be activated, and sometimes an overlap of the three processes happens if

active inflammation is sustained [162-164]. Vascular permeability has also been found to be influenced by numerous (at least 25) gene products [161]. The dynamic nature of vascular permeability and the environmental factors involved are still elusive.

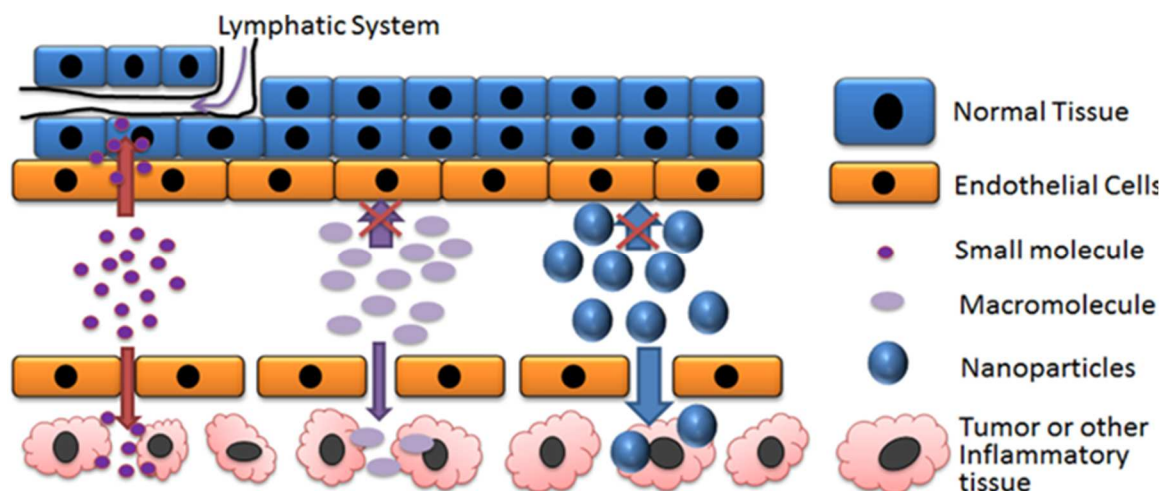


Figure 26: Schematic describing transport of molecules through the cardiovascular and lymphatic system in normal tissue with basal blood vessel permeability and tumor or other inflammatory tissues with increased blood vessel permeability.

7.1.4 Current *in vivo* and *in vitro* platforms

The complex cellular mechanisms contributing to an increase in the permeability of blood vessels are partially understood. Scientists have employed *in vivo* and *in vitro* platforms to understand the underlying mechanism. Miles assay and its variants are established techniques to analyze vascular permeability *in vivo* [165-168], as shown in Figure 27 (A-C). This assay determines the leakage of a visible dye from the vasculature into the surrounding tissue spectrophotometrically but has several limitations including that it only allows a single time point analysis, a high degree of variability and low repeatability, and an inability to investigate

localized differences in vascular permeability [161, 169]. *In vivo* studies also often require complex mammalian models and time-consuming surgical protocols, making animals an expensive and challenging platform. They also raise ethical issues and such models also respond differently than humans as interspecies predictability is low in response to drugs and diseases [13]. *In vivo* studies also allow limited control of the heterogeneous physical, chemical, and biological parameters influencing the blood vessel and present challenges with respect to imaging as well [14].

Relatively easier and simple *in vitro* platforms are also being used to better understand the phenomenon behind leaky and heterogeneous vasculature by measuring the flux of molecules of various sizes that traverse endothelial cells cultured in transwell chambers [170-174], as shown in Figure 27 (D-E). To measure the permeability of the cultured endothelial cell monolayer *in vitro*, conventional assays such as trans-endothelial electrical resistance (TEER) [175-176] and tracer leakage [177-178] are widely used. TEER based assays are based on electrical impedance measurements which do not provide direct quantitative measurement of biomolecule transportation. *In vitro* studies are also mostly performed under static conditions without consideration of the FSS conditions the endothelium are exposed to *in vivo*. Kim *et al* [179] studies cytokine mediated controlled permeability on an endothelial cell layer through NP extravasation in a microfluidic platform. However, this study was performed under static condition without consideration of the FSS conditions the endothelium is exposed to *in vivo*. A few studies do incorporate FSS in the study of endothelial cell permeability [180-

181]. An *in vitro* blood vessel model that incorporates endothelial cell culture under native conditions with the capability to model specific disease and physiological flow conditions has huge potential. Such a biomimetic system can greatly accelerate drug screening process in pharmacological studies.

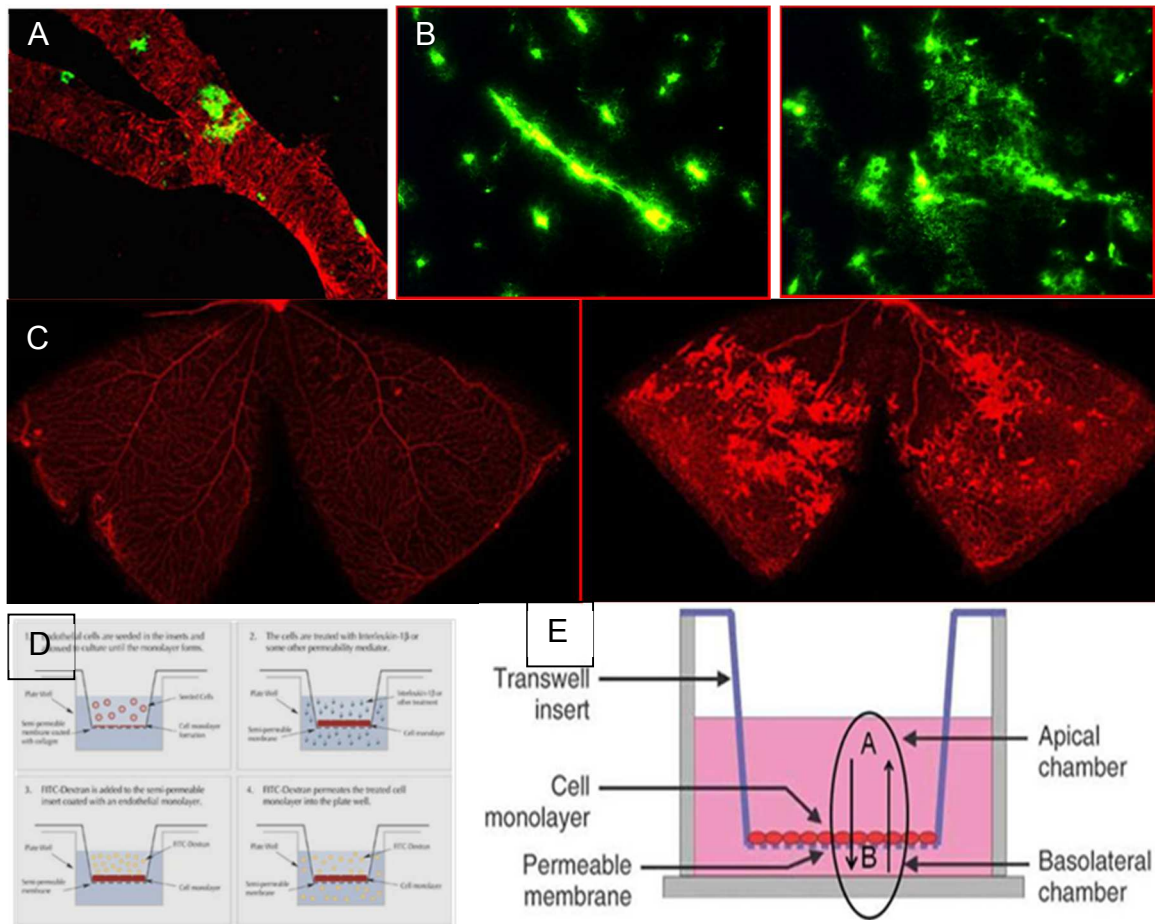


Figure 27: *In vivo* (A,B & C) and *in vitro* (D & E) techniques to analyze vascular permeability. A, Tumor vessel (red) showing localized leaky spots (green) [182];B, Fluorescent dye highlights intact blood vessel with basal permeability (Left). Tumor blood vessel with increased vascular permeability (Right)[183];C, Normal mouse retina. Right image (Left). Abnormal blood vessel growth and permeability characteristic of diabetes and inflammatory signaling [184-186]; D, Commercial *in vitro* vascular permeability test platform based on transwell inserts [187]; E, Bi-directional transport studies using Caco-2 cells on transwell insert [188].

7.1.5 Significance of FSS

Blood vessel endothelium is constantly exposed to FSS at its apical side due to blood flow. Maintaining the natural phenotype of endothelial cells is critical to the success of a biomimetic blood vessel model and subjecting the endothelial cells to native *in vivo* FSS is important [119]. Exposing the endothelial cell layer to directed and sustained FSS at *in vivo* levels down regulates their pro-inflammatory and proliferative pathways [120] and is critical to the expression of endothelial cell responses [189]. The mechanical stress caused on the endothelial cell layer due to this is an important extrinsic factor capable of modifying vessel barrier properties by altering the inter-endothelial junctions and the endothelial cell-extracellular matrix interactions [190-193]. It can also activate intracellular signaling events altering barrier properties like, increased intracellular Ca^{2+} levels and the generation of inositol trisphosphate [194-196], activation of Rac [197-198], RhoA-dependent reorganization of actin cytoskeleton [191-192, 199] and β_1 -integrin-dependent increase in caveolin-1 phosphorylation [191]. Therefore integrating *in vivo* levels of flow to the endothelial cell culture is important in limiting the chances of the cell monolayer undergoing phenotype drift and no longer reflecting its *in situ* characteristics. An *in vitro* blood vessel model that can sustain endothelial cell culture under native conditions, and is capable of evaluating the heterogeneous nature of vessel permeability when triggered by a single or a cocktail of inflammatory mediators holds huge potential. Such a translatory platform can bridge the gap between *in vivo* and traditional *in vitro* systems.

7.1.6 Thrombin

Thrombin, a protease produced on the surface of injured endothelium from prothrombin can induce profound alterations of endothelial cell monolayer permeability *in vitro* and *in vivo* [200]. Thrombin induces blood coagulation, as well as also triggers specific stimuli on the endothelial cell layer leading to paracellular gap formation and release of inflammatory mediators, vasoregulatory agents, and growth factors. Paracellular gap formation of the endothelium is accompanied by reversible cell rounding and compromised barrier function [201]. Barrier integrity of the endothelium is ensured by the cytoskeleton, which is regulated by actin stress fiber formation and via actomyosin-driven contraction to managing cell shape and attachment [202]. Actin filaments at the periphery of endothelial cells are linked to cell-to-cell adherence junctions. These organelles are formed by transmembrane calcium-dependent adhesive proteins called vascular endothelial cadherins. These molecules are associated inside the cells with a complex network of cytoskeletal molecules [203-205].

Proteinase-activated receptor (PAR) is the thrombin endothelial cell receptor protein and is similar to G-protein-coupled receptors containing seven transmembrane domains in its structure [206]. Binding of thrombin to PAR initiates activation of heterotrimeric G-proteins. This in turn produces a decrease in cyclic adenosine monophosphate level, increases intracellular Ca^{2+} and diacylglycerol concentration and activates the small G-protein, Rho, in the cell. Also, activation of myosin light chain kinase and inactivation of myosin phosphatases leads to phosphorylation of myosin light chains which stimulates stress fiber formation and

triggers actin-myosin contraction. In addition, Ca^{2+} /calmodulin-dependent protein kinase, protein kinase C, and tyrosine protein kinases regulate thrombin-induced rearrangement in the endothelial cytoskeleton [202]. These processes would sequentially lead to stimulation of an endothelial contractile reaction, which would eventually produce intercellular gaps.

This project studies the dynamics of acute increase in endothelial cell permeability brought about by thrombin, an inflammation triggering agent in blood vessels. Thrombin induces blood coagulation and triggers specific stimuli on the endothelial cell layer leading to paracellular gap formation and release of inflammatory mediators, vasoregulatory agents, and growth factors [200]. The *in vitro* bio-mimetic blood vessel platform used in this study consists of an upper and lower microfluidic channel separated by a semi-permeable membrane. Primary bovine aortic endothelial cells were cultured on the semi-permeable membrane under *in vivo* levels of flow. In order to study the increase in vascular permeability under inflammation, this monolayer of endothelial cells was exposed to flow of media spiked with thrombin and a tracer molecule. Efflux of fluorescein isothiocyanate (FITC)-dye and FITC-dextran tracer molecules were used to quantify the vascular permeability. The tracer molecule samples that permeated to the lower channel from the upper channel separated by the cell layer and membrane were collected real time and analysed to understand the dynamic nature of the process. The remodeling of F-actin stress fibers in endothelial cells on thrombin treatment was studied using immunofluorescence staining. This versatile platform facilitated the

study of the combined interplay of heterogeneous mechanisms contributing to an increase in permeability of blood vasculature.

7.2 Material and Methods

7.2.1 Fabrication and endothelial cell culture

Channels made of polydimethylsiloxane (PDMS) were photolithographically patterned and fabricated, and a monolayer culture of BAOECs was attained as explained in chapter # 5 and previous works [207]. The upper and lower channels are casted out of Sylgard 184 PDMS (Dow Corning Corp.). The upper channel is 20 mm long, 350 μm wide and 100 μm tall, and the lower channel is 5 mm long, 1000 μm wide and 100 μm tall. A polycarbonate (PC), track-etched thin clear membrane (Whatman, GE Healthcare) with 1 μm diameter pores and an average calculated pore density of 1.5×10^7 pores/ cm^2 is embedded between two PDMS channels. The bottom channel PDMS layer is bonded on to a thin glass slide by exposing the sides in contact to oxygen plasma. Upper PDMS channels is bonded to the membrane by using a thin PDMS mortar film (10:1 ratio of base and curing agent with toluene in equal proportion). The upper channel bonded to the membrane is then bonded to lower channel after making sure the channels are aligned. After each step the components were placed in an oven at 60°C for the appropriate time to enhance bonding. Inlet and outlet ports were punched to provide access to upper and lower channels.

Once fabricated, the devices were sterilized in UV light overnight and certified for cell culture. Prior to cell seeding the upper channel and membrane of the device were coated with 50 $\mu\text{g}/\text{ml}$ fibronectin solution (Sigma-Aldrich) overnight at 37°C. BAOECs cells were seeded in the upper channel at a density of 2×10^7 cells/ml and

let to attach on the semi-permeable membrane. Cell seeded devices were placed in an incubator under standard culture conditions (37°C and 5% CO₂) overnight to allow cell attachment and spreading on the membrane. On reaching confluence, the BAOECs were subjected to a physiologically relevant fluid shear stress (FSS) of 12 dyne/cm². The flow was brought about using a high precision and extremely low pulsation peristaltic pump (ISMAT endothelial cell, IPC-N series) and the entire setup was placed in standard culture conditions. Recirculation of media was not permitted while thrombin and tracer molecules were passed through the channels. To calculate the volumetric flow rate that correspond to the required maximum FSS experienced by the endothelial cells, the following equation was used [114].

$$\tau_{cell} = \frac{6\mu Q}{wh^2}$$

7.2.2 Thrombin treatment and cell permeability assay

BAOECs were treated with thrombin at 1 Unit (U)/ml concentration after being subjected to 6 hrs or more of flow in the microfluidic model. Thrombin induces an acute inflammatory response on endothelial cells and leads to profound increase in endothelial cell monolayer permeability. Thrombin was added to flow media along with the tracer molecule and the treatment was performed under flow on the apical side of the cells. The dosage and treatment time for thrombin to induce an increase in permeability on BAOEC monolayer was determined from other studies [208-211] and by performing cell permeability assay on transwell inserts. For this the BAOECs were seeded at a density of 2×10^4 cells in the luminal chamber of

ThinCert transparent insert for 12-well plates having a membrane with 1 μm pore diameter. Cells were cultured in DMEM with 10% of heat inactivated fetal bovine serum and, upon confluence the cells were treated with thrombin by replacing the medium in the luminal side with fresh DMEM (1% heat inactivated serum) supplemented with thrombin and tracer molecule. Media volumes of 1500 μl and 500 μl were maintained in the abluminal and luminal sides respectively to make sure the hydrostatic pressure between the chambers remained a constant. 750 μl of media from the abluminal chamber was replaced every 10 min and the presence of tracer molecule was monitored photometrically on the collected sample. To keep the permeability assay protocol in the biomimetic platform and the transwell insert study similar, the supplemented media in the luminal chamber was also replaced every 10 min to ensure a fresh and constant supply of thrombin and the tracer molecule.

7.2.3 Quantifying vascular permeability

Vascular permeability occurs through intercellular gap formation. We quantified the dynamics and kinetics of cell permeability caused by thrombin on BAOECs using our biomimetic blood vessel model. Fluorescent FITC sodium salt and FITC-Dextran (Sigma) of 376 and 4000 Da molecular weight were used as tracer molecules at 0.625 and 5 mg/ml respectively. The desired tracer molecule was included in flow media along with thrombin in the luminal upper channel and the extent of tracer molecule permeation to the abluminal lower channel is a direct indication of the level of vessel permeability. This was monitored real time by withdrawing 6 μl samples from the outlet of the lower channel every 10 minutes.

These samples were analyzed photometrically using Infinite 200 PRO NanoQuant microplate readers at 490 nm excitation and 521 nm emission. The volume of buffer solution in the lower channel was maintained constant by adding 6 μ l of PBS to the inlet before withdrawing the data sample. The abluminal media sample collected every 10 min for the transwell insert static cell case was also analyzed as described above.

7.2.4 Localization of Actin Filaments and Immunofluorescence Staining

In order to understand the correlation between the increase in vessel permeability and F-actin cytoskeletal arrangement patterns on thrombin treatment, the rearrangement of F-actin stress fibers was studied. Confluent monolayers were treated with 1 U/ml thrombin in DMEM medium (1% heat inactivated serum) for various lengths of time. The static case was performed on endothelial cells cultured on fibronectin coated cover slips, and for the flow case thrombin was spiked along with flow media in the biomimetic microfluidic blood vessel platform. After thrombin treatment, cells were fixed with 3.7% paraformaldehyde (Sigma) for 20 minutes and permeabilized with 0.5% Triton X-100 (Sigma) for 3 minutes. Endothelial cells were washed with PBS between each step and were finally stained with 50 μ g/ml FITC-phalloidin (Thermo Fisher Scientific Inc.) solution in PBS and processed for immunofluorescence microscopy. Observations were performed with a fluorescence confocal microscope (FV1000-IX81, Olympus) and image analysis was performed using ImageJ software.

7.2.5 Statistical analysis

The results are an average from three independent experiments with a p -value <0.05 . The results are presented as the mean \pm the standard deviation. An unpaired Student t test was used to analyze statistical differences between control and treated groups. Differences were considered statistically significant at $p < 0.05$.

7.3 Results and Discussion

7.3.1 On-chip cell culture

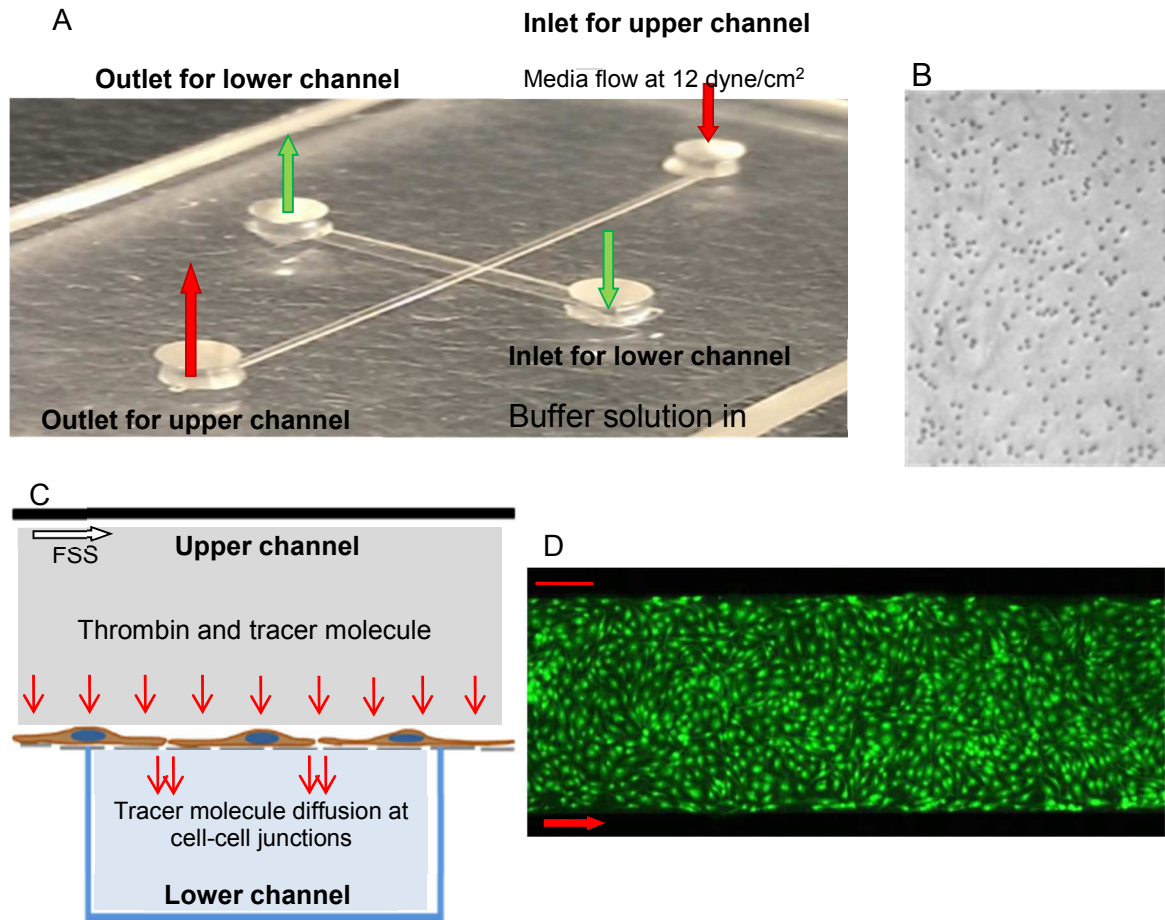


Figure 28: (A) Photograph of the bi-layer device showing the upper and lower channel separated by the semi-permeable membrane along with their inlets and outlets. The apical side of the endothelial cell layer face the upper channel are exposed to media flow. Thrombin and tracer molecule are added to media to study blood vessel permeability under acute inflammation. Tracer molecule diffusion to the lower channel is controlled by the extend of endothelial cell permeability under inflammation. The diffused data sample is collected from the lower channel. (B) Bright field image of the membrane with 1 μm diameter pores at an average density of $1.5 \times 10^7/\text{cm}^2$. (C) Schematic depiction of endothelial cell growth on semi-permeable membrane, thrombin treatment from upper channel and tracer molecule diffusion through intercellular gaps. (D) Fluorescence labelled actin cytoskeleton (FITC-phalloidin) images of confluent BAOEC layer aligned to flow (12 dyne/cm^2 FSS for 6 hrs) in the upper channel. Arrow shows flow direction (Scale bar: 100 μm)

Characterization of endothelial cell culture on the biomimetic blood vessel microfluidic device has been detailed in our prior work [207]. The device has the upper channel arranged perpendicular to the lower channel, and the media, thrombin and tracer molecule are flowed in through the inlet of the upper channel (Figure 28 A). The porous PC membrane is cell culture friendly and provides the base for cell growth and proliferation as demonstrated before [110-111, 115-116, 207]. Transport between the upper and lower channels is limited through the membrane pores present at an average density of $1.5 \times 10^7/\text{cm}^2$. This high pore density and the $1 \mu\text{m}$ pore diameter (Figure 28B) allow for free flow of tracer molecules through the membrane to the lower channel once it passes through the endothelial cell layer. As explained in Figure 28C, thrombin and tracer molecule flow along with media and thus thrombin would act on the endothelial cell from the apical side. With the onset of endothelial cell gap formation the tracer molecule would permeate through these gaps to the lower channel. Thus the extent of vessel permeability can be understood from the amount of tracer molecule in the lower channel.

An intact blood vessel endothelium is constantly exposed to FSS at its apical side due to blood flow. Therefore integrating *in vivo* levels of flow to the endothelial cell culture is important in limiting the chances of the cell monolayer undergoing phenotype drift and thus no longer reflecting *in situ* characteristics. Figure 28D is a micrograph of F-actin stained confluent BAOEC monolayer aligned to flow (12 dyne/cm^2 FSS for 6 hrs) in our blood vessel model. Details on cell shape, F-actin

filament alignment and reorganization on exposure to FSS in this device have been reported previously in chapter 5 here.

7.3.2 Characterizing vascular permeability on biomimetic blood vessel model

Our platform is utilized to understand the increase in vessel permeability during an inflammatory state under physiologically relevant conditions. We used fluorescent tracer molecules of two different molecular weights and analyzed their diffusive permeability from the upper to the lower channel of the device, separated by the endothelial cell monolayer. The amount of tracer molecule transported to the lower channel will be a measure of the dynamics of vascular permeability based on its inflammatory response to thrombin treatment.

Endothelial barrier integrity was determined by real-time measurement of tracer molecule transport to the lower abluminal channel from the upper luminal channel, when the endothelial cells were grown to confluence on the semi-permeable membrane separating the two channels. FITC sodium salt and FITC-dextran 4kD were used as low and high molecular weight tracer molecules respectively and they were analyzed photometrically. Figure 29 A and B shows the permeability curve for FITC sodium salt and FITC-dextran respectively, along with the control case where the cells were not treated with thrombin. The data sample was collected from the lower abluminal channel every 10 min. Tracer molecule concentration was quantified by comparing the fluorescence intensity of collected data samples to a concentration calibration curve. It is observed that for both tracer molecules, the concentration in lower channel starts to increase acutely within 10

min of thrombin treatment and reaches the max value (0.09 mg/ml for FITC sodium salt and 0.34 mg/ml for FITC-Dextran 4kDa) within 20-30 min. This means the permeability or gap formation of the endothelial cell monolayer initializes rapidly under flow and reaches its maximum within 20-30 minutes. There is an increase of around 3.5 times in permeability for both tracer molecules by then and this is a direct measure of the change in endothelial cell-cell gap formation. Then a fall in abluminal concentration of tracer molecule is observed which plateaus to a minimum value at about 60-70 min. This signifies the decrease in endothelial cell permeability due to the reduction in intercellular gaps as a result of barrier recovery by the endothelial cells after the acute increase in permeability. FITC sodium salt and FITC-dextran were included in flow media at different concentrations in the luminal channel for ease of photometrical detection and analysis. Vascular permeability dynamics of similar nature in BAOECs by thrombin have been elucidated in previous studies [208-210, 212-213].

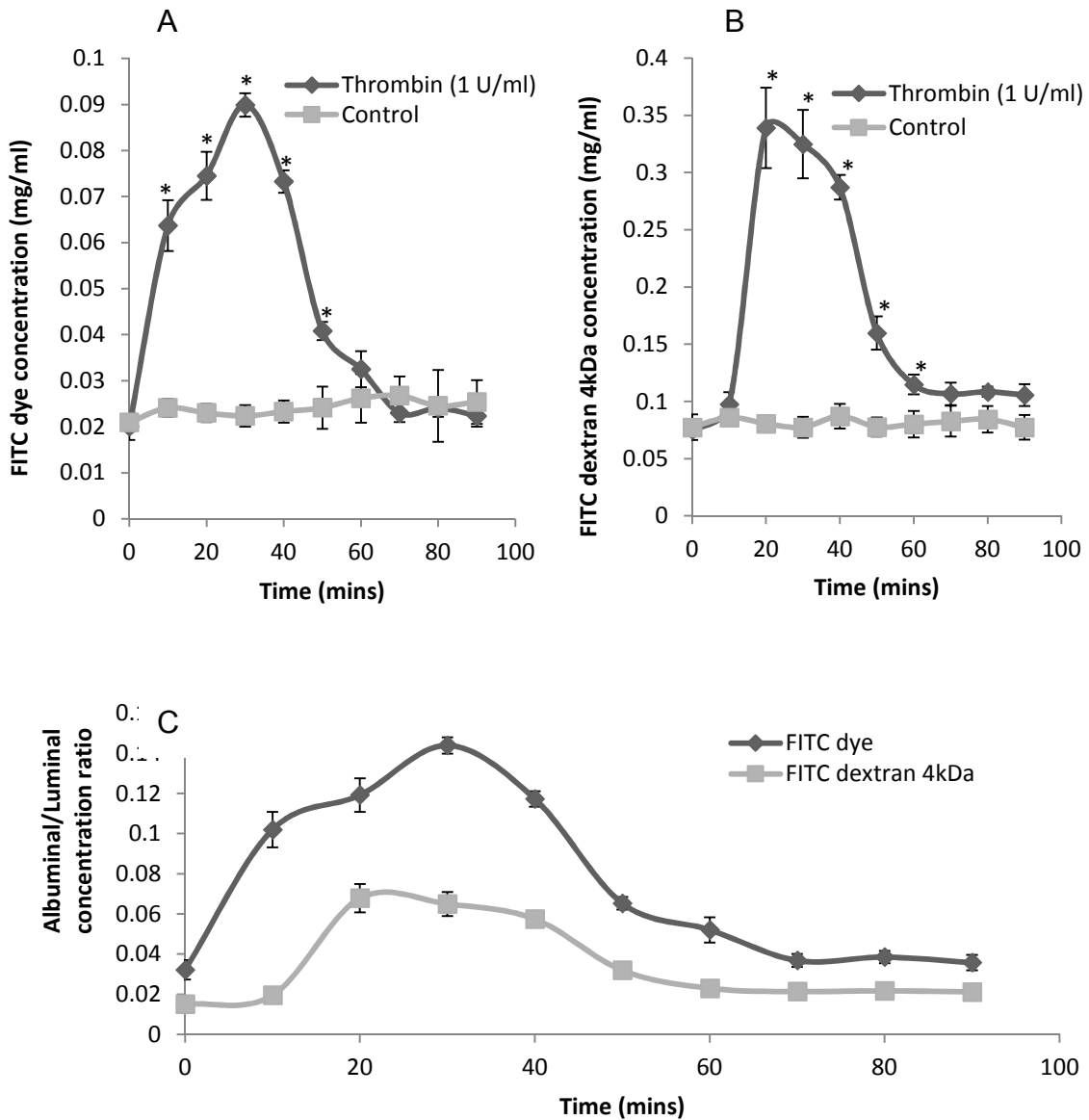


Figure 29: Permeability of the tracer molecule through the endothelial cell layer in the biomimetic device. (A) Permeability of FITC dye through the endothelial cell layer when treated with thrombin at 1 U/ml compared to control case. (B) Permeability of FITC dextran 4kDa through the endothelial cell layer when treated with thrombin at 1 U/ml compared to control case. (C) Normalized comparison of FITC dye and FITC dextran 4 kDa permeability on the endothelial cell monolayer when treated with thrombin at 1 U/ml. FITC dye with a lower molecular weight has higher permeability compared to FITC dextran 4 kDa. Asterisks indicate values significantly different from control values ($p < 0.05$).

Figure 29 C compares the concentration of the tracer molecules in the abluminal channel to their luminal concentration. For this, the concentration of tracer

molecule in the abluminal channel is divided by the respective luminal concentration and compared versus the thrombin treatment time. This normalizes the effect of doing the tests at different luminal concentrations for the two tracer molecules to an extent, and gives an idea on how the size of the tracer molecule affects permeability. It is found that the permeability of tracer molecule across the endothelial cells decreased with increasing molecular weight. The lower molecular weight FITC sodium salt diffused more through the intercellular gaps than the higher molecular weight FITC-dextran 4kD. Similar results have been previously observed in studies using tracer molecules of different size [214-218]. A reduction in diffusivity was observed with an increase in molecular weight of the tracer molecule.

7.3.3 Characterizing vascular permeability using transwell inserts

We compared the permeability data generated on the biomimetic platform to that produced using traditional transwell inserts. On transwell inserts we maintained a static culture of endothelial cells and treated with thrombin on reaching confluence. As explained in the methods section, we collect all the tracer molecules in the abluminal side in the blood vessel model by flushing 6 μ l of buffer solution through the lower channel every 10 min. Whereas in the transwell study only half of the total tracer molecules that permeated to the abluminal side gets collected. So the following reading would have leftover tracer molecules from the previous time point. We normalized this effect for the transwell data by mathematically subtracting the possible amount of tracer molecule leftover from the previous time point for all data points. As shown in Figure 30 A, thrombin significantly increased

the permeability of endothelial cell monolayer within 10 min, which reached a maximum by about 20-30 min. After this we observed a fall in tracer molecule concentration which signifies a decrease in endothelial permeability. The permeability is comparable to control case within about 80 min of thrombin treatment.

The dynamics of vessel permeability observed in the biomimetic blood vessel model and the traditional transwell system are similar. The recovery of endothelial barrier function was a steady and relatively slower process in the static transwell insert studies (about 80 min to plateau) compared to the flow integrated microfluidic blood vessel platform. The permeability was comparable to basal levels after about 80 min of thrombin treatment, compared to that achieved within 60-70 min in the biomimetic platform (Figure 30 B). We further examined the F-actin remodeling under thrombin treatment on endothelial cells in these two different platforms, to compare the transient nature of stress fiber alignment related to barrier integrity recovery.

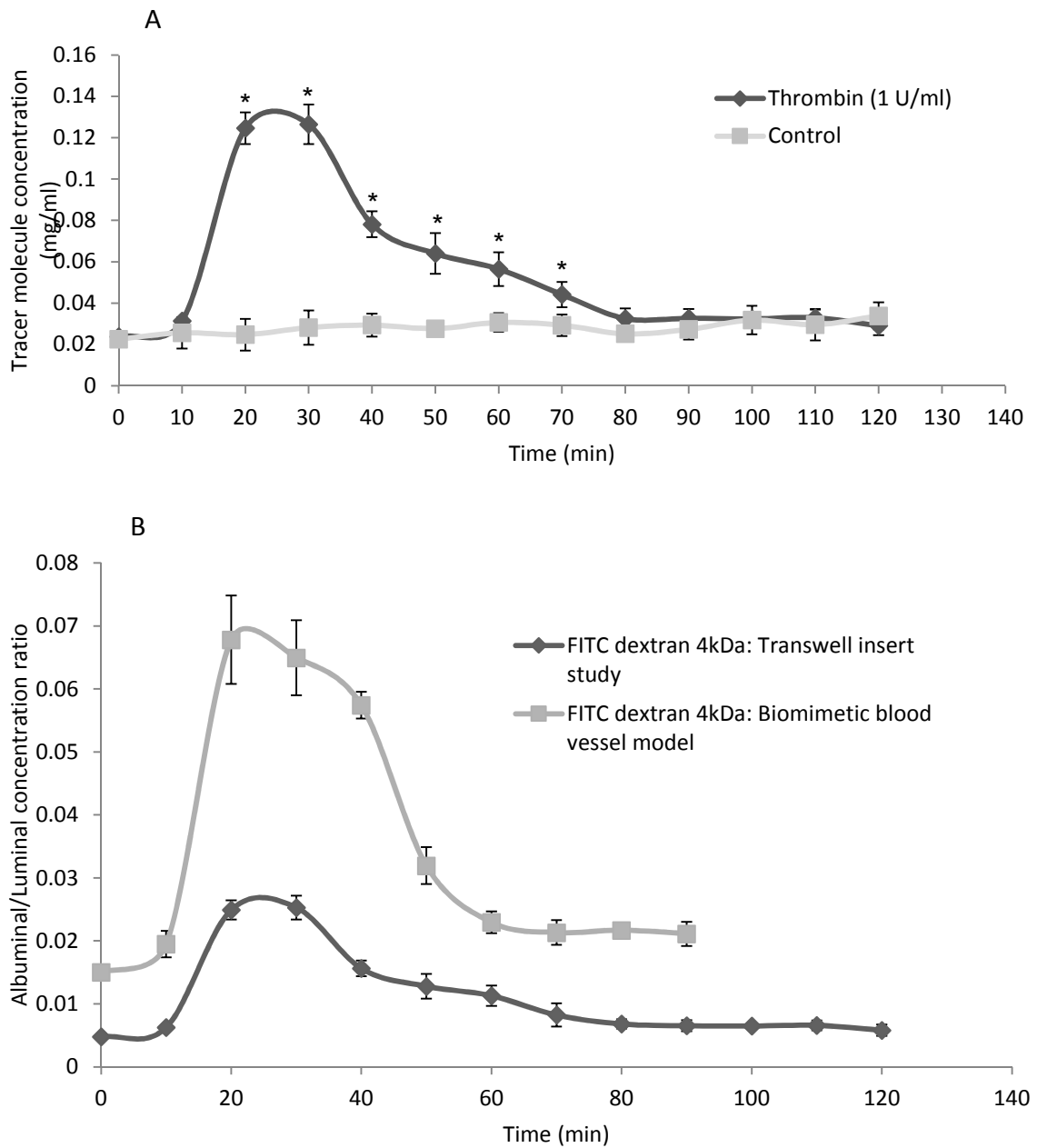


Figure 30: Permeability of tracer molecule through the endothelial cell layer in the transwell insert study. (A) Permeability of FITC dextran 4kDa through the endothelial cell layer when treated with thrombin at 1 U/ml compared to control case. (B) Normalized comparison of FITC dextran 4 kDa permeability on the endothelial cell monolayer in the biomimetic device and transwell insert case on thrombin treatment. Endothelial cell monolayer in the biomimetic device recovers its barrier integrity within about 60 min compared to about 80 min in the transwell insert case. Asterisks indicate values significantly different from control values ($p < 0.05$).

7.3.4 F-actin cytoskeletal remodeling

Thrombin treatment of endothelial cells leads to F-actin cytoskeletal filament formation and rearrangement. Thrombin induces myosin light chain phosphorylation and subsequent activation of acto-myosin based contractile systems. This leads to isometric tension development in the cell and thus endothelial cell retraction and increase in vessel permeability [219-222]. After demonstrating the kinetics of endothelial cell monolayer permeability through tracer molecule transport in static (endothelial cells cultured on transwell inserts) versus flow case (endothelial cells cultured in the biomimetic blood vessel model), confocal microscopy and immunofluorescence staining was used to examine the changes in F-actin stress fiber arrangement after thrombin treatment (1 U/ml). Figure 31 and Figure 32 show z-series composite micrographs of control and thrombin stimulated endothelial cell monolayers for both cases respectively. The control case consists of a monolayer of endothelial cells with tight intercellular contact and predominantly peripheral cortical actin. With thrombin stimulation, F-actin undergoes rapid and reversible redistribution and intercellular gap formation for both cases.

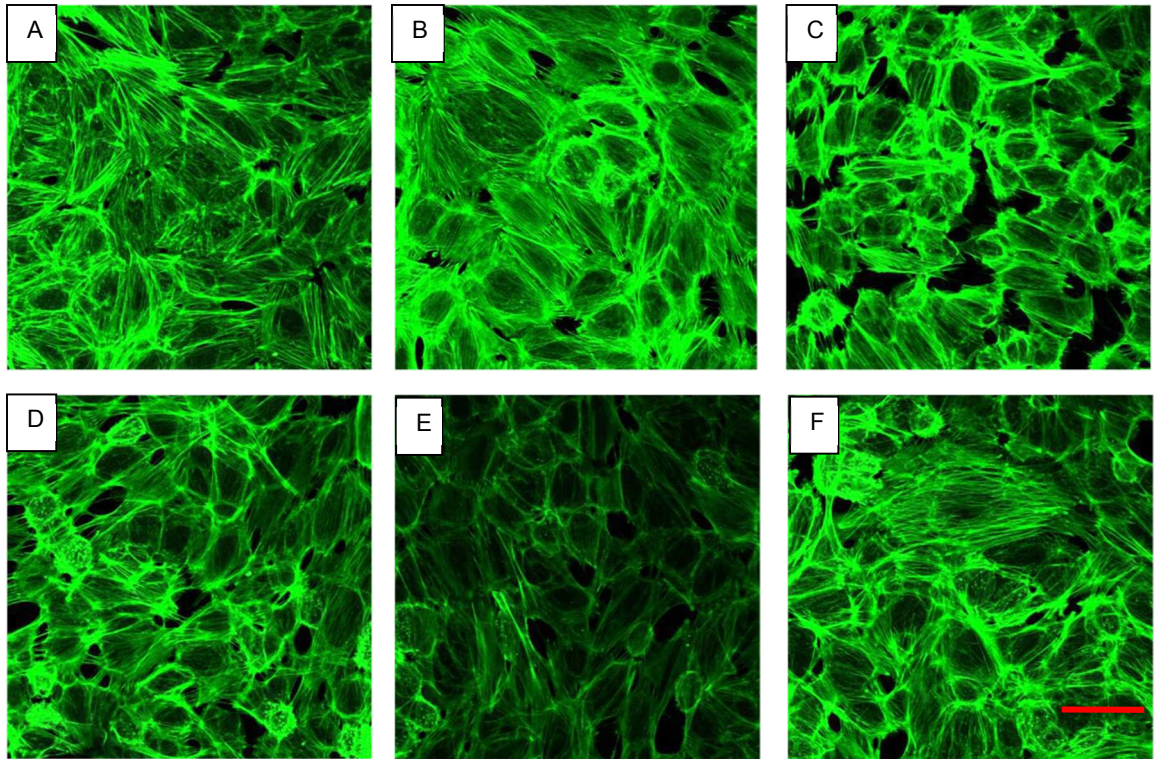


Figure 31: Thrombin induces F-actin remodeling on BAOECs cultured on a cover slip. (A) Control case not subjected to thrombin treatment. Note the tight intercellular contact and predominantly peripheral cortical actin staining; (B) 20 minutes of thrombin treatment at 1 U/ml appears to induce intercellular gap formation and marked increase in actin stress fiber formation. (C) 40 minutes of thrombin treatment at 1 U/ml increases intercellular gap formation and produces notable decrease in cell size possibly due to acto-myosin based cell contraction. (D) 60 minutes of thrombin treatment at 1 U/ml seems to reduce intercellular gaps. (E) 80 minutes of thrombin treatment at 1 U/ml has significantly reduced intercellular gaps and there is significant decrease in F-actin stress fiber presence. (F) 100 minutes of thrombin treatment at 1 U/ml produce cell characteristics comparable to control case. (Scale bar: 25 μ m)

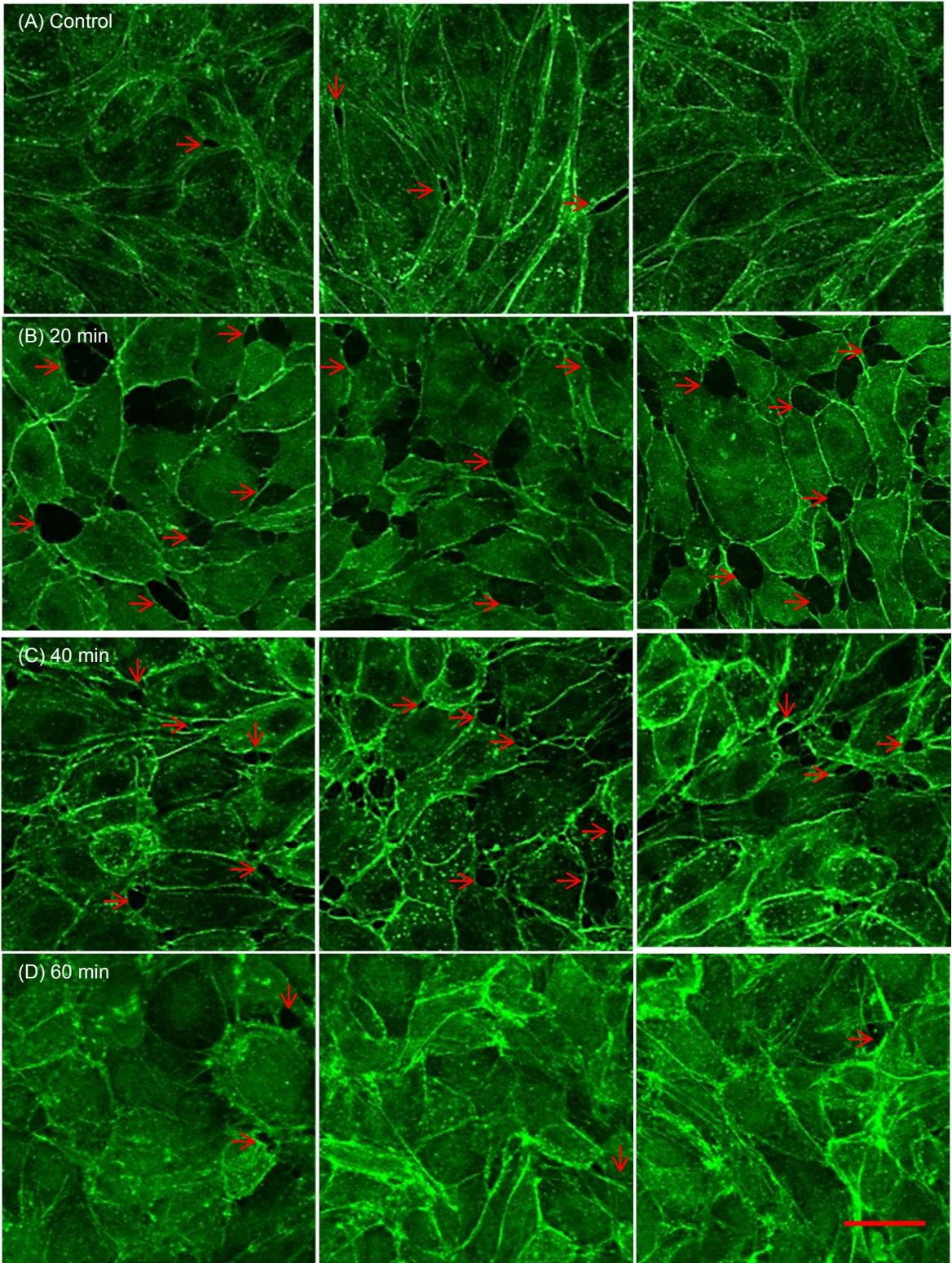


Figure 32: BAOECs cultured in the microfluidic biomimetic device are treated with thrombin along with flow which induces F-actin remodeling. (B) 20 minutes of thrombin treatment at 1 U/ml produce regions without F-actin stress fibers between cells which signify inter-cellular gap formation. (C) These gaps tends to reduce and bridge by increased cortical actin presence towards the cell periphery after 40 minutes of thrombin treatment. (D) There is steady presence of F-actin filaments on the cell monolayer after 60 minutes of thrombin treatment, signifying the decrease in inter-cellular gaps. (Scale bar: 25 μm)

For the static case where the cells were cultured on cover slips, detailed orientation of F-actin fibers and cell-cell gap formation were visible (Figure 31). After 20 min of thrombin treatment the actin had reorganized into prominent stress fibers aligned parallel to each other and to the long axis of the cell. Compared to the control case, the cells had retracted from one another and exhibit small gaps between adjacent cells while retaining their polygonal morphology. The endothelial cells still remained attached to one another and in many areas the stress fibers appeared to be contiguous between adjacent cells. 40 min of thrombin treatment increased intercellular gaps and produced notable decrease in cell size possibly due to acto-myosin based cell contraction. There was a reduction in intercellular gaps and a reversal in thrombin based inflammatory response by 60 min of treatment. 80 minutes of thrombin treatment produced cell monolayers with significantly reduced intercellular gaps and there was also a significant decrease in the presence of F-actin stress fiber in the cell cytoplasm. The 100 min case had cell characteristics comparable to that of control (no thrombin treatment) case.

The biomimetic blood vessel platform being thin enough allowed imaging of the endothelial cells at 60x magnification using an oil immersion objective. But the presence of multiple layers (glass, PDMS, membrane) of different refractive indices between the cell and the objective resulted in images that were compromised on details. Stress fiber presence and orientation were not well described in these images, but details on cell-cell gap formation were available (Figure 32). 20 min of thrombin treatment on endothelial cells under flow resulted in intercellular regions lacking F-actin stress fibers, which signify inter-cellular gap

formation. After 40 min, these gaps decreased in size and frequency. The gaps have reduced by increased cortical actin presence towards cell periphery. Further thrombin treatment (60 min) lead to uniform F-actin presence throughout the cell monolayer with reduced intercellular gaps, which was comparable to the control case.

Our results on static cover slip studies are comparable to already established literature. Thrombin stimulation initially causes polymerization of actin fibers in endothelial cells that organize into thick stress fibers and are arranged parallel to each other, leading to intercellular gap formation [220]. Further treatment is known to decrease F-actin quantity and return to the control case (no thrombin) level [223]. Quantifying F-actin content in thrombin activated endothelial cells has shown an increase in actin polymerization during the initial 30 min of thrombin treatment and then a reduction in total F-actin content by 60 min [220].

7.3.5 Comparison of biomimetic model to transwell insert study

Endothelial cells when removed from their native environment become separated from critical extracellular cues and can undergo phenotypic drifts. Traditional *in vitro* studies can provide an approximation of the true biology, but cannot account the true nature due to the lack of a holistic system [224-225]. An *in vivo* intact endothelium is exposed to multiple factors and is differentially regulated in space and time [224, 226]. Current *in vitro* platforms for studying endothelial cell biology and permeability have limitations in incorporating these numerous and dynamic factors. Our biomimetic blood vessel platform cultures endothelial cells in their

native flow environment and we can expose cells to multiple external cues in a controlled manner to understand their responses towards the heterogeneous environment. *In vivo* studies on rats and mice have found an increase in vascular permeability to reach its peak by around 15 min and fall back to control levels (or follow that trend) within 60 min of thrombin treatment [227-230]. The majority of *in vitro* studies have reported similar acute nature in the increase of vessel permeability by thrombin, but the dynamics of endothelial cell monolayer barrier recovery to reach control or baseline levels of permeability have been different. *In vitro* it usually takes longer than the average 60 min observed *in vivo*, an average of about 90-120 min [200, 208, 230-236].

In our work we checked the permeability of endothelial cells when treated with thrombin in our novel biomimetic blood vessel model under flow and also in the traditional transwell insert static culture system. The static platform produced endothelial cell permeability curves comparable to other studies where the barrier recovery occurred by around 80-90 min. In the biomimetic blood vessel model the endothelial cell layer achieved barrier recovery at a similar rate, within 60-70 min. We examined the F-actin remodeling pattern as well to understand the gap formation in cells subjected to thrombin. The static case had F-actin stress fiber formation, disassembly, related gap formation and its recovery on a time scale comparable to the tracer molecule based barrier recovery study (around 80 min). The endothelial cells in biomimetic blood vessel platform showed F-actin stress fiber based gap formation within 20 min and recovery of endothelial cell monolayer

barrier integrity by 60 min of thrombin treatment, supporting the tracer molecule permeability data.

7.4 Conclusion

Endothelial cells, when removed from their native tissue environment and cultured on traditional *in vitro* platform are uncoupled from critical extracellular cues and have a tendency to undergo phenotypic drift. This causes changes in cell signaling pathways and the transcriptional control machinery making such platforms hard to analyze. Inflammatory responses in endothelial cells produce an increase in vascular permeability by formation of intercellular gaps. In this study we use an engineered biomimetic blood vessel microfluidic model to characterize the dynamic nature of increase in vascular permeability, and compare these results to traditional transwell insert permeability assays. The biomimetic blood vessel model has a monolayer of endothelial cells cultured under *in vivo* levels of flow. This endothelial monolayer was treated with thrombin, a serine protease which induces a rapid and reversible increase of endothelial cell monolayer permeability. Thrombin disrupts the endothelial barrier function of the endothelial cell monolayer cultured on a semi-permeable membrane, which separates the bi-layer device. This induces para-cellular gap formation and allows the transport of tracer molecules through these gaps from the upper to the lower channel. Tracer molecule samples are collected real time and analyzed via spectroscopy, and the dynamic nature of the process is observed. On the biomimetic platform and transwell insert studies the transient nature of increase in permeability and their barrier recovery was comparable. F-actin stress fiber remodelling patterns were also studied as reorganization of the endothelial cell cytoskeleton provided the structural basis for changes in vascular permeability.

We present here a biomimetic blood vessel model capable of culturing endothelial cells under flow, while being possible to trigger them spatially and temporally from the basal or apical side. Our biomimetic platform is an apt replacement tool to perform blood vessel related studies. Platform like that of ours should be able to bridge the void space between traditional *in vitro* studies and the more complicated *in vivo* studies, providing vital tools for translational research to provide therapeutic gain and reduce drug attrition.

Chapter 8

Some general discussion and suggestions for future research

In this thesis, microfluidics, cell biology and aspects of engineering are brought together to construct *in vitro* blood vessel platforms to answer challenging questions in the field of targeted drug delivery and vascular biology. In this chapter, we provide discussions which cut across the results, and provide some suggestions for future work.

8.1 General discussions

The first half of the thesis concentrates on building a protein coating based blood microvessel model to characterize specific binding of drug model particles. The binding density of anti-ICAM-1 coated 210 nm and 2 μm particles on ICAM-1 modified PDMS microfluidic devices was characterized. The study employs various factors that influence particle distribution and binding, such as flow shear rate, particle size, RBCs, vessel geometry, antibody coating density on the particle, particle concentration and effect of asymmetric flow profiles. The results helped to determine the transport properties and binding of drug carriers in the microvasculature. Particles of the right size range provide better bioavailability and enhanced targeted binding, and these factors need to be considered to provide higher efficacy and minimal drug dosage. From this work we conclude that 2 μm particles have better binding efficiency based on number count and volume under low to medium flow shear rates. For disease conditions where a higher particle concentration or dosage is acceptable (drug toxicity not an issue) and higher shear

flows are involved, the smaller particles of the 200 nm scale would be more suitable. Properties like the enhanced particle margination and binding to the wall at high particle flow concentration observed in this work favours the use of NPs. Other advantages like the ability to be better retained in tissues via the enhanced permeability and retention effect, longer circulation period and better targeting ability are also in favour of NPs. When designing targeted vascular drug carriers various parameters have to be considered like the disease condition, permissible drug toxicity based particle concentration, reticuloendothelial system evading properties etc. Inspired by this work we developed the customizable biomimetic microfluidic blood vessel platform based on culturing endothelial cells under flow. This model is capable of mimicking specific blood vasculature conditions based on disease state and physiological spot of origin.

The biomimetic blood vessel model developed and explained in the second half of the thesis is a tool with unprecedented ability to investigate the microenvironment of endothelial cells. The simplicity of traditional *in vitro* models, which usually consist of a single cell type, makes them robust and suitable for high throughput research, but unfortunately provides only little biological relevance to the complex biological tissues of the real system. Furthermore, the culture conditions do not closely mimic the *in vivo* microenvironment due to the absence of the fluid flow and shear stresses [237]. Also, these cultures are less suited to provide a dynamically controlled flow of cell nutrients and stimuli and, additionally, the accumulation of waste leads to a pH drift in a static culture. Other drawbacks of the classical cell culture systems are the long growth times needed for cells to differentiate into

functional cells and the dependence on external signal detection systems that require manual withdrawing and manipulation of samples. The microfluidic chip we developed can mimic a close to native environment for endothelial cells by facilitating *in vivo* levels of flow and biomolecule supply, along with features that allow real-time studies. The endothelial monolayer can be accessed from their apical and basal side, allowing simulation of physiologic conditions as endothelial cells are triggered from blood vessel lumen side or tissue side or both. We characterized BAOEC culture under physiological levels of flow and analyzed their F-actin organization pattern. We utilized this platform to understand endothelial microenvironment responses to inflammatory triggering. Localized TNF- α treatment was performed on the BAOECs from the basal side of the cell and ICAM-1 upregulation in the upstream, TNF- α treated and downstream section of the channels were analyzed. Anti-ICAM-1 coated fluorescent imaging probes were used to characterize the upregulation of surface-ICAM-1 on endothelial cells. Particle binding per cell data was obtained using 210 nm particles and 1 μ m particles. By analyzing the particle binding along the length of the channel we characterized the nature of ICAM-1 expression for BAOECs along the channel length. We also outlined the nature of TNF- α based actin depolymerization and rearrangement along channel length. This platform also enabled the real-time study of increase in surface-ICAM-1 expression on endothelial cells by studying the amount of particle binding over time while TNF- α treatment was performed. It was of interest to note that ICAM-1 expression dynamics were different for cells cultured under flow from those in a static culture. The same platform was modified

to suit an assay to understand the dynamics of change in vascular permeability. Endothelial cells exhibit a loss of vascular barrier integrity as part of its response to inflammatory stimuli. Endothelial cell monolayers cultured under flow in our device were treated with thrombin, an acute inflammatory mediator. The dynamics of vascular permeability were understood by studying the extent of tracer molecule diffusion through the endothelial cell monolayer to the lower channel. The work was compared to traditional transwell insert study and the cells cultured under flow recovered their barrier integrity at a faster rate compared to the static case. These studies highlight the versatile nature and functionality of the microfluidic biomimetic blood vessel platform developed. This allowed studying detailed physiological events related to blood vessels, and in consequence understanding the influence of specific biomolecules on a specific function as well as on the healthy/diseased state modulation.

8.2 Future research

8.2.1 Co-culture of endothelial cells and SMCs

Endothelial cell-SMC interactions play a synergistic role in endothelial cell development, cell proliferation and differentiation, their response to growth factors, mechano-chemical coupling, cell motility and directional control [238-240]. Platforms where these two cell types are grown on the opposite sides of membrane have already been established [241-242] and applied to study the influence of SMCs in the effect of shear stress on endothelial biology [239], and SMC influence on the patterns of leukocyte adhesion to the endothelial cell [240]. We have done some initial scouting on how to facilitate SMC co-culture along with endothelial cells on our biomimetic blood vessel model to take it a step closer to mimicking *in vivo* niche.

The dimensions and shape of our established biomimetic blood vessel platform can be tuned to fit the co-culture of SMCs along with endothelial cells. The lower channel will be wider to increase the co-culture area and both channels will have the ability to be accessed separately. The upper and lower channel along with the membrane will be coated with 50 µg/ml fibronectin solution overnight at 37°C. BAOECs will be seeded onto the semi-permeable membrane in the upper channel followed by BAOSMCs cells seeding onto the semi-permeable membrane in the lower channel. The device will be placed in the incubator under standard culture conditions (37°C and 5% CO²) for 4 hrs after both cases of cell seeding to allow cell attachment and spreading on the membrane. Media will be frequently changed

in both the channels. We performed a proof-of-concept trial of this protocol and the cells were cultured for a day. Both the BAOECs and BAOSMCs were stained with Calcein AM (live cell stain) to evaluate their viability. Figure 33 shows micrographs of confluent layers of BAOECs and BAOSMCs growing in the upper and lower channel respectively. Further work on this platform can be conducted by subjecting the co-culture cell system to relevant FSS from the endothelial cell side and performing further characterizations.

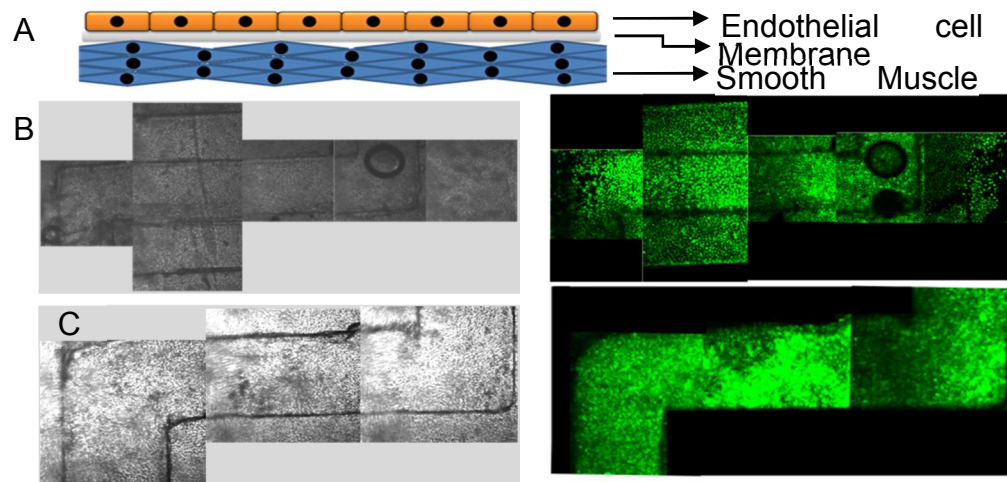


Figure 33: Image of a microfluidic platform devised to co-culture endothelial cells and SMCs on the opposite sides of a membrane. (A) Culture of endothelial cells and SMCs on the opposite sides of a porous membrane; (B) Brightfield micrograph of the upper channel (B) and of the lower channel (C); Calcein AM stained (D) BAOECs in upper channel and (E) BAOSMCs in lower channel.

8.2.2 Leukocyte recruitment and trans-migration studies

Our platform can also be tuned to perform leukocyte recruitment and trans-migration studies on an endothelial cell layer under inflammatory conditions. Recruitment of leukocytes from blood to tissues is a multi-step process playing a

major role in the activation of inflammatory responses. Tethering and rolling of leukocytes along the vessel wall, followed by arrest and transmigration through the endothelium result from chemo-attractant dependent signals. Shear forces exerted by the blood flow on leukocytes induce rolling via selectin-mediated interactions with endothelial cells and increase the probability that leukocytes will engage their chemokine receptors, facilitating integrin activation and consequent arrest. Flow based shear forces generate mechanical stimuli along with biochemical signals in the modulation of leukocyte-endothelial cell interactions [243]. The limitation of the static environment can be overcome with our custom built blood vessel model mimicking the *in vivo* conditions. Our device can create an *in vitro* biomimetic environment where the multi-step transmigration process can be imaged and quantified under mechanical and biochemical controlled conditions, including fluid dynamic settings, channel design, materials and surface coatings. By using an appropriate semi-permeable membrane (with a pore size that will allow leukocyte migration), we can study the dynamics and kinetics of the process. The results should be able to throw light at details of the process that are still elusive.

8.2.3 Modeling tumor environment

During tumor growth, some unique pathophysiological characteristics that are not observed in normal tissues or organs are present, such as extensive angiogenesis and hence hypervascularity, defective vascular architecture, impaired lymphatic drainage/recovery system, and greatly increased production of a number of permeability mediators. This leads to higher pressure inside tumors. While the interstitial fluid pressure (IFP) in normal tissues is actively controlled and remains

close to atmospheric levels, IFP in most human tumors is highly elevated [159]. Other causes of IFP include increased resistance to interstitial fluid flow and impaired lymphatic drainage [244]. As a result, transporting drug molecules into solid tumors can be a challenge. Cancer also remains the leading cause of death mainly due to tumor invasion and metastasis [245]. Studies on tumor invasion have not yet brought to light the details of the invasion cascades [246-247]. The entry of tumor cells into blood vessels is an important route for penetrating into the circulatory system and subsequently metastasizing to another organ through blood vessel walls [248]. Reproducing a tumor microenvironment consisting of blood vessels and tumor cells for modeling tumor invasion *in vitro* can provide answers to above mentioned maladies, but constructing such a system is particularly challenging. By tuning the right parameters we can model such a tumor microenvironment by growing 3D tumor blocks in hydrogel in the lower channel of our blood vessel model. This allows the study of blood vessel-3D tumor microenvironment interaction. The results and answers that could be generated on such a controlled tumor environment-blood vessel model would be relevant from a physiology and therapeutic perspective.

References

1. Muzykantov, V.R., *Targeted Drug Delivery to Endothelial Adhesion Molecules*. ISRN Vascular Medicine, 2013. 2013: p. 27.
2. Tang, L. and J. Cheng, *Nonporous silica nanoparticles for nanomedicine application*. Nano Today, 2013. 8(3): p. 290-312.
3. Suwussa Bamrungsap, Z.Z., Tao Chen, Lin Wang, Chunmei Li, Ting Fu & Weihong Tan, *Nanotechnology in therapeutics: a focus on nanoparticles as a drug delivery system*. Nanomedicine (Lond), 2012. 7(8): p. 1253-71.
4. Nazir, S., et al., *Nanomaterials in combating cancer: Therapeutic applications and developments*. Nanomedicine: Nanotechnology, Biology and Medicine, 2014. 10(1): p. 19-34.
5. Chakraborty C, P.S., Doss GP, Wen ZH, Lin CS, *Nanoparticles as 'smart' pharmaceutical delivery*. Front Biosci (Landmark Ed), 2013. 1(18): p. 1030-50.
6. Agnieszka Z. Wilczewska, K.N., Karolina H. Markiewicz, Halina Car, *Nanoparticles as drug delivery systems*. Pharmacological Reports, 2012. 64: p. 1020-1037.
7. Crielaard, B.J., et al., *Drug targeting systems for inflammatory disease: One for all, all for one*. Journal of Controlled Release, 2012. 161(2): p. 225-234.
8. Farokhzad, O.C. and R. Langer, *Impact of Nanotechnology on Drug Delivery*. ACS Nano, 2009. 3(1): p. 16-20.
9. Schroeder, A., et al., *Treating metastatic cancer with nanotechnology*. Nat Rev Cancer, 2012. 12(1): p. 39-50.
10. Peer, D., et al., *Nanocarriers as an emerging platform for cancer therapy*. Nat Nano, 2007. 2(12): p. 751-760.
11. Lobatto, M.E., et al., *Perspectives and opportunities for nanomedicine in the management of atherosclerosis*. Nat Rev Drug Discov, 2011. 10(11): p. 835-852.
12. Langer, R., *Drug Delivery and Targeting*. Nature, 1998. 392: p. 9-10.
13. Shanks, N., R. Greek, and J. Greek, *Are animal models predictive for humans?* Philosophy, Ethics, and Humanities in Medicine, 2009. 4(1): p. 2.
14. Staton, C.A., et al., *Current methods for assaying angiogenesis in vitro and in vivo*. International Journal of Experimental Pathology, 2004. 85(5): p. 233-248.
15. Pittman, R.N., *Oxygen Transport and Exchange in the Microcirculation*. Microcirculation, 2005. 12(1): p. 59-70.
16. Sottile, J., *Regulation of angiogenesis by extracellular matrix*. Biochimica et Biophysica Acta (BBA) - Reviews on Cancer, 2004. 1654(1): p. 13-22.
17. Bonetti, P.O., L.O. Lerman, and A. Lerman, *Endothelial Dysfunction: A Marker of Atherosclerotic Risk*. Arteriosclerosis, Thrombosis, and Vascular Biology, 2003. 23(2): p. 168-175.
18. Cines, D.B., et al., *Endothelial Cells in Physiology and in the Pathophysiology of Vascular Disorders*. Blood, 1998. 91(10): p. 3527-3561.
19. Koren, E. and V.P. Torchilin, *Drug carriers for vascular drug delivery*. IUBMB Life, 2011. 63(8): p. 586-595.
20. *Cancer Facts & Figures 2015*. <http://www.cancer.org/research/cancerfactsstatistics/cancerfactsfigures2015/index>.
21. Steyers, C.M. and F.J. Miller, *Endothelial Dysfunction in Chronic Inflammatory Diseases*. International Journal of Molecular Sciences, 2014. 15(7): p. 11324-11349.
22. Murdaca, G., et al., *Endothelial dysfunction in rheumatic autoimmune diseases*. Atherosclerosis, 2012. 224(2): p. 309-317.
23. Prati, C., et al., *Endothelial dysfunction in joint disease*. Joint Bone Spine, 2014. 81(5): p. 386-391.
24. Rajendran, P., et al., *The Vascular Endothelium and Human Diseases*. International Journal of Biological Sciences, 2013. 9(10): p. 1057-1069.
25. Trepel, M., R. Pasqualini, and W. Arap, *Chapter 4 Screening Phage-Display Peptide Libraries for Vascular Targeted Peptides*, in *Methods in Enzymology*, A.C. David, Editor. 2008, Academic Press. p. 83-106.

26. D'Onofrio, N., et al., *Vascular-homing peptides for targeted drug delivery and molecular imaging: Meeting the clinical challenges*. *Biochimica et Biophysica Acta (BBA) - Reviews on Cancer*, 2014. 1846(1): p. 1-12.
27. Zetter, B.R., *On target with tumor blood vessel markers*. *Nat Biotech*, 1997. 15(12): p. 1243-1244.
28. Dunehoo, A.L., et al., *Cell adhesion molecules for targeted drug delivery*. *Journal of Pharmaceutical Sciences*, 2006. 95(9): p. 1856-1872.
29. Vaupel, P., *Tumor microenvironmental physiology and its implications for radiation oncology*. *Seminars in Radiation Oncology*, 2004. 14(3): p. 198-206.
30. Cairns, R., I. Papandreou, and N. Denko, *Overcoming Physiologic Barriers to Cancer Treatment by Molecularly Targeting the Tumor Microenvironment*. *Molecular Cancer Research*, 2006. 4(2): p. 61-70.
31. Dejana, E., *Endothelial adherens junctions: implications in the control of vascular permeability and angiogenesis*. *The Journal of Clinical Investigation*, 1996. 98(9): p. 1949-1953.
32. Kumar, S., D.C. West, and A. Ager, *Heterogeneity in endothelial cells from large vessels and microvessels*. *Differentiation*, 1987. 36(1): p. 57-70.
33. Wojta, J., R.L. Hoover, and T.O. Daniel, *Vascular origin determines plasminogen activator expression in human endothelial cells. Renal endothelial cells produce large amounts of single chain urokinase type plasminogen activator*. *Journal of Biological Chemistry*, 1989. 264(5): p. 2846-2852.
34. Louise, C.B. and T.G. Obrug, *Human Renal Microvascular Endothelial Cells as a Potential Target in the Development of the Hemolytic Uremic Syndrome as Related to Fibrinolysis Factor Expression, in Vitro*. *Microvascular Research*, 1994. 47(3): p. 377-387.
35. Drake, T.A., et al., *Expression of tissue factor, thrombomodulin, and E-selectin in baboons with lethal Escherichia coli sepsis*. *The American Journal of Pathology*, 1993. 142(5): p. 1458-1470.
36. Packhaeuser, C.B., et al., *In situ forming parenteral drug delivery systems: an overview*. *European Journal of Pharmaceutics and Biopharmaceutics*, 2004. 58(2): p. 445-455.
37. Singh, R. and J.W. Lillard Jr, *Nanoparticle-based targeted drug delivery*. *Experimental and Molecular Pathology*, 2009. 86(3): p. 215-223.
38. Muro, S., et al., *Endothelial Targeting of High-Affinity Multivalent Polymer Nanocarriers Directed to Intercellular Adhesion Molecule 1*. *Journal of Pharmacology and Experimental Therapeutics*, 2006. 317(3): p. 1161-1169.
39. Greg Light, S.S., Eun-Jung Park, Denise Drane, *Student understanding of "surface-area-to-volume ratio" and its relationship to property change in the nano-science engineering context*. 2010.
40. Chacko, A.-M., et al., *Targeted nanocarriers for imaging and therapy of vascular inflammation*. *Current Opinion in Colloid & Interface Science*, 2011. 16(3): p. 215-227.
41. Kerbel, R. and J. Folkman, *Clinical translation of angiogenesis inhibitors*. *Nat Rev Cancer*, 2002. 2(10): p. 727-739.
42. Gimbrone, M.A., T. Nagel, and J.N. Topper, *Biomechanical activation: an emerging paradigm in endothelial adhesion biology*. *The Journal of Clinical Investigation*, 1997. 99(8): p. 1809-1813.
43. Zhai, Y., et al., *LIGHT, a novel ligand for lymphotoxin beta receptor and TR2/HVEM induces apoptosis and suppresses in vivo tumor formation via gene transfer*. *The Journal of Clinical Investigation*, 1998. 102(6): p. 1142-1151.
44. Min, J.-K., et al., *TNF-Related Activation-Induced Cytokine Enhances Leukocyte Adhesiveness: Induction of ICAM-1 and VCAM-1 via TNF Receptor-Associated Factor and Protein Kinase C-Dependent NF-κB Activation in Endothelial Cells*. *The Journal of Immunology*, 2005. 175(1): p. 531-540.
45. Kanwar, J.R., et al., *Requirements for ICAM-1 immunogene therapy of lymphoma*. *Cancer Gene Ther*, 2003. 10(6): p. 468-476.
46. Hiroaki Tanaka, M.Y., Takeshi Sunami, Masaichi Ohira, K. Hirakawa-Y.S. Chung, *Lipid-mediated gene transfection of intercellular adhesion molecule-1 suppresses the peritoneal metastasis of gastric carcinoma*. *International Journal of Molecular Medicine*, 2002. 10(5).
47. Mayrovitz, H.N., R.F. Tuma, and M.P. Wiedeman, *Relationship between microvascular blood velocity and pressure distribution*. *American Journal of Physiology - Heart and Circulatory Physiology*, 1977. 232(4): p. H400-H405.
48. <http://www.thefreedictionary.com/microvasculature>.
49. Fåhræus, R. and T. Lindqvist, *The Viscosity of the blood in narrow capillary tubes*. *American Journal of Physiology -- Legacy Content*, 1931. 96(3): p. 562-568.

50. YANG, B.H., et al., *Migration of a sphere in tube flow*. Journal of Fluid Mechanics, 2005. 540: p. 109-131.
51. Segré, G. and A. Silberberg, *Behaviour of macroscopic rigid spheres in Poiseuille flow Part 2. Experimental results and interpretation*. Journal of Fluid Mechanics, 1962. 14(01): p. 136-157.
52. Harry L, G., *The microcirculatory society Eugene M. Landis award lecture: The microrheology of human blood*. Microvascular Research, 1986. 31(2): p. 121-142.
53. Kim, S., et al., *The cell-free layer in microvascular blood flow*. Biorheology, 2009. 46(3): p. 181-189.
54. McHedlishvili, G. and N. Maeda, *Blood Flow Structure Related to Red Cell Flow: Determinant of Blood Fluidity in Narrow Microvessels*. The Japanese Journal of Physiology, 2001. 51(1): p. 19-30.
55. Pries, A.R., T.W. Secomb, and P. Gaehtgens, *Biophysical aspects of blood flow in the microvasculature*. Cardiovascular Research, 1996. 32(4): p. 654-667.
56. William I, R., *Ratio of red cell velocities near the vessel wall to velocities at the vessel center in cerebral microcirculation, and an apparent effect of blood viscosity on this ratio*. Microvascular Research, 1972. 4(1): p. 98-101.
57. Reinke, W., P. Johnson, and P. Gaehtgens, *Effect of shear rate variation on apparent viscosity of human blood in tubes of 29 to 94 microns diameter*. Circulation Research, 1986. 59(2): p. 124-132.
58. Gaehtgens, P., H.J. Meiselman, and H. Wayland, *Velocity profiles of human blood at normal and reduced hematocrit in glass tubes up to 130 μ diameter*. Microvascular Research, 1970. 2(1): p. 13-23.
59. Yasuhiko Sugii, S.N., Koji Okamoto, *In vivo PIV measurement of red blood cell velocity field in microvessels considering mesentery motion*. Physiological Measurement, 2002. 23(2).
60. Popel AS, J.P., *Microcirculation and hemorheology*. Annual Review of Fluid Mechanics, 2005. 37: p. 43-69.
61. Ho Seong Ji, J.Y.L.a.S.J.L., *In-vitro study on the hemorheological characteristics of chicken blood in microcirculation*. Rheology Journal, 2007. 19: p. 89-95.
62. Nanne, E.E., C.P. Aucoin, and E.F. Leonard, *Shear Rate and Hematocrit Effects on the Apparent Diffusivity of Urea in Suspensions of Bovine Erythrocytes*. ASAIO Journal, 2010. 56(3): p. 151-156
10.1097/MAT.0b013e3181d4ed0f.
63. Aarts, P., R. Heethaar, and J. Sixma, *Red blood cell deformability influences platelets--vessel wall interaction in flowing blood*. Blood, 1984. 64(6): p. 1228-1233.
64. Goldsmith, H.L. and S.G. Mason, *Particle motions in sheared suspensions XIII. The spin and rotation of disks*. Journal of Fluid Mechanics, 1962. 12(01): p. 88-96.
65. J. Siepmann, F.S., *Mathematical modeling of drug delivery*. International Journal of Pharmaceutics, 2008. 364(2): p. 328-343.
66. Lee, M.J.-E., et al., *Rapid Pharmacokinetic and Biodistribution Studies Using Cholorotoxin-Conjugated Iron Oxide Nanoparticles: A Novel Non-Radioactive Method*. PLoS ONE, 2010. 5(3): p. e9536.
67. Ogawa, M., et al., *New Nanosized Biocompatible MR Contrast Agents Based on Lysine-Dendri-Graft Macromolecules*. Bioconjugate Chemistry, 2010. 21(5): p. 955-960.
68. Haun, J.B. and D.A. Hammer, *Quantifying Nanoparticle Adhesion Mediated by Specific Molecular Interactions*. Langmuir, 2008. 24(16): p. 8821-8832.
69. Kona, S., et al., *Biodegradable nanoparticles mimicking platelet binding as a targeted and controlled drug delivery system*. International Journal of Pharmaceutics, (0).
70. Christopher A Baker, C.T.D., Alix Grimley, and Michael G Roper, *Recent advances in microfluidic detection systems*. Bioanalysis, 2009. 1(5): p. 967-975.
71. Wang, D.-A. and R.I. Mahato, *A Preface for Engineered Biomimetic Tissue Platforms for in Vitro Drug Evaluation*. Molecular Pharmaceutics, 2014. 11(7): p. 1931-1932.
72. Vunjak-Novakovic, G. and D.T. Scadden, *Biomimetic platforms for human stem cell research*. Cell stem cell, 2011. 8(3): p. 252-261.
73. Lee, J. and S. Lee, *Murray's law and the bifurcation angle in the arterial micro-circulation system and their application to the design of microfluidics*. Microfluidics and Nanofluidics, 2010. 8(1): p. 85-95.
74. Lew, H.S. and Y.C. Fung, *Entry flow into blood vessels at arbitrary Reynolds number*. Journal of Biomechanics, 1970. 3(1): p. 23-38.
75. Nagaoka, T. and A. Yoshida, *Noninvasive Evaluation of Wall Shear Stress on Retinal Microcirculation in Humans*. Investigative Ophthalmology & Visual Science, 2006. 47(3): p. 1113-1119.
76. Patrizia Nigro, J.-i.A., and Bradford C. Berk., *Flow Shear Stress and Atherosclerosis: A Matter of Site Specificity*. Antioxidants & Redox Signaling, 2011. 15(5): p. 1405-1414.

77. Pries, A.R., T.W. Secomb, and P. Gaehtgens, *Structure and hemodynamics of microvascular networks: heterogeneity and correlations*. American Journal of Physiology - Heart and Circulatory Physiology, 1995. 269(5): p. H1713-H1722.
78. Gearing, A.J.H. and W. Newman, *Circulating adhesion molecules in disease*. Immunology Today, 1993. 14(10): p. 506-512.
79. Blankenberg, S., et al., *Circulating Cell Adhesion Molecules and Death in Patients With Coronary Artery Disease*. Circulation, 2001. 104(12): p. 1336-1342.
80. Son, Y., *Determination of shear viscosity and shear rate from pressure drop and flow rate relationship in a rectangular channel*. Polymer, 2007. 48(2): p. 632-637.
81. Chau, L., M. Doran, and J. Cooper-White, *A novel multishear microdevice for studying cell mechanics*. Lab on a Chip, 2009. 9(13): p. 1897-1902.
82. Charoenphol, P., R.B. Huang, and O. Eniola-Adefeso, *Potential role of size and hemodynamics in the efficacy of vascular-targeted spherical drug carriers*. Biomaterials, 2010. 31(6): p. 1392-1402.
83. Namdee, K., et al., *Margination Propensity of Vascular-Targeted Spheres from Blood Flow in a Microfluidic Model of Human Microvessels*. Langmuir, 2013. 29(8): p. 2530-2535.
84. V R Shinde Patil, C.J.C., Y H Yun, S M Slack, and D J Goetz, *Particle diameter influences adhesion under flow*. Biophys Journal, 2001. 80(4): p. 1733-1743.
85. P Decuzzi, F.G., A Granaldi, A Curcio, F Causa, *Flow chamber analysis of size effects in the adhesion of spherical particles*. International Journal of Nanomedicine, 2007. 2(4): p. 689 - 696.
86. Goldman, A.J., R.G. Cox, and H. Brenner, *Slow viscous motion of a sphere parallel to a plane wall—II Couette flow*. Chemical Engineering Science, 1967. 22(4): p. 653-660.
87. Tan, J., et al., *Coupled particulate and continuum model for nanoparticle targeted delivery*. Computers & Structures, 2013. 122(0): p. 128-134.
88. Zhang Z, K.C., Donohue JF, Kim CS, *Comparison of micro- and nano-size particle depositions in a human upper airway model*. J Aerosol Sci, 2005. 36: p. 211-233.
89. Prabhakarandian, B., et al., *Bifurcations: Focal Points of Particle Adhesion in Microvascular Networks*. Microcirculation, 2011. 18(5): p. 380-389.
90. Lamberti, G., et al., *Adhesive interaction of functionalized particles and endothelium in idealized microvascular networks*. Microvascular Research, 2013. 89(0): p. 107-114.
91. Tan, J., et al., *The influence of size, shape and vessel geometry on nanoparticle distribution*. Microfluidics and Nanofluidics, 2013. 14(1-2): p. 77-87.
92. Abbitt, K.B. and G.B. Nash, *Rheological properties of the blood influencing selectin-mediated adhesion of flowing leukocytes*. American Journal of Physiology - Heart and Circulatory Physiology, 2003. 285(1): p. H229-H240.
93. Gentile, F., et al., *The margination propensity of spherical particles for vascular targeting in the microcirculation*. Journal of Nanobiotechnology, 2008. 6(1): p. 9.
94. Tan, J., A. Thomas, and Y. Liu, *Influence of red blood cells on nanoparticle targeted delivery in microcirculation*. Soft Matter, 2012. 8(6): p. 1934-1946.
95. Eckstein, E.C., A.W. Tilles, and F.J. Millero Iii, *Conditions for the occurrence of large near-wall excesses of small particles during blood flow*. Microvascular Research, 1988. 36(1): p. 31-39.
96. Melder, R.J., et al., *Selectin- and integrin-mediated T-lymphocyte rolling and arrest on TNF-alpha-activated endothelium: augmentation by erythrocytes*. Biophysical Journal, 1995. 69(5): p. 2131-2138.
97. Maeda, N., et al., *Erythrocyte flow and elasticity of microvessels evaluated by marginal cell-free layer and flow resistance*. American Journal of Physiology - Heart and Circulatory Physiology, 1996. 271(6): p. H2454-H2461.
98. Fenton, B., D. Wilson, and G. Cokelet, *Analysis of the effects of measured white blood cell entrance times on hemodynamics in a computer model of a microvascular bed*. Pflügers Archiv, 1985. 403(4): p. 396-401.
99. R T Yen, Y.C.F., *Effect of velocity of distribution on red cell distribution in capillary blood vessels*. The American journal of physiology, 1978. 09: p. H251-7.
100. Fung, Y.-C., *Stochastic flow in capillary blood vessels*. Microvascular Research, 1973. 5(1): p. 34-48.
101. Allen, T.M. and P.R. Cullis, *Liposomal drug delivery systems: From concept to clinical applications*. Advanced Drug Delivery Reviews, 2013. 65(1): p. 36-48.
102. Mourya, V.K. and N. Inamdar, *Trimethyl chitosan and its applications in drug delivery*. Journal of Materials Science: Materials in Medicine, 2009. 20(5): p. 1057-1079.

103. Danhier, F., et al., *PLGA-based nanoparticles: An overview of biomedical applications*. *Journal of Controlled Release*, 2012. 161(2): p. 505-522.
104. Lammers, T., et al., *Drug targeting to tumors: Principles, pitfalls and (pre-) clinical progress*. *Journal of Controlled Release*, 2012. 161(2): p. 175-187.
105. Rakesh, K.J. and S. Triantafyllos, *Delivering nanomedicine to solid tumors*. *Nature Reviews Clinical Oncology*, 2010. 7(11): p. 653-664.
106. Park, J.W., et al., *Anti-HER2 Immunoliposomes: Enhanced Efficacy Attributable to Targeted Delivery*. *Clinical Cancer Research*, 2002. 8(4): p. 1172-1181.
107. Orcutt, K.D., et al., *Effect of Small-Molecule-Binding Affinity on Tumor Uptake In Vivo: A Systematic Study Using a Pretargeted Bispecific Antibody*. *Molecular Cancer Therapeutics*, 2012. 11(6): p. 1365-1372.
108. Torchilin, V.P., *Multifunctional nanocarriers*. *Advanced Drug Delivery Reviews*, 2006. 58(14): p. 1532-1555.
109. Chueh, B.-h., et al., *Leakage-Free Bonding of Porous Membranes into Layered Microfluidic Array Systems*. *Analytical Chemistry*, 2007. 79(9): p. 3504-3508.
110. Young, E.W.K., et al., *Technique for Real-Time Measurements of Endothelial Permeability in a Microfluidic Membrane Chip Using Laser-Induced Fluorescence Detection*. *Analytical Chemistry*, 2010. 82(3): p. 808-816.
111. Huh, D., et al., *Acoustically detectable cellular-level lung injury induced by fluid mechanical stresses in microfluidic airway systems*. *Proceedings of the National Academy of Sciences*, 2007. 104(48): p. 18886-18891.
112. Eddington, D.T., J.P. Puccinelli, and D.J. Beebe, *Thermal aging and reduced hydrophobic recovery of polydimethylsiloxane*. *Sensors and Actuators B: Chemical*, 2006. 114(1): p. 170-172.
113. Lee, J.N., C. Park, and G.M. Whitesides, *Solvent Compatibility of Poly(dimethylsiloxane)-Based Microfluidic Devices*. *Analytical Chemistry*, 2003. 75(23): p. 6544-6554.
114. Khan, O. and M. Sefton, *Endothelial cell behaviour within a microfluidic mimic of the flow channels of a modular tissue engineered construct*. *Biomedical Microdevices*, 2011. 13(1): p. 69-87.
115. Huh, D., et al., *Reconstituting Organ-Level Lung Functions on a Chip*. *Science*, 2010. 328(5986): p. 1662-1668.
116. Ismagilov, R.F., et al., *Microfluidic Arrays of Fluid-Fluid Diffusional Contacts as Detection Elements and Combinatorial Tools*. *Analytical Chemistry*, 2001. 73(21): p. 5207-5213.
117. Chien, S., *Molecular basis of rheological modulation of endothelial functions: Importance of stress direction*. *Biorheology*, 2006. 43(2): p. 95-116.
118. Li, Y.-S.J., J.H. Haga, and S. Chien, *Molecular basis of the effects of shear stress on vascular endothelial cells*. *Journal of Biomechanics*, 2005. 38(10): p. 1949-1971.
119. Wasserman, S.M. and J.N. Topper, *Adaptation of the endothelium to fluid flow: in vitro analyses of gene expression and in vivo implications*. *Vascular Medicine*, 2004. 9(1): p. 35-45.
120. Chien, S., *Effects of Disturbed Flow on Endothelial Cells*. *Annals of Biomedical Engineering*, 2008. 36(4): p. 554-562.
121. Malek, A.M. and S. Izumo, *Mechanism of endothelial cell shape change and cytoskeletal remodeling in response to fluid shear stress*. *Journal of Cell Science*, 1996. 109(4): p. 713-726.
122. Wong, A., T. Pollard, and I. Herman, *Actin filament stress fibers in vascular endothelial cells in vivo*. *Science*, 1983. 219(4586): p. 867-869.
123. Kim, D.W., A.I. Gotlieb, and B.L. Langille, *In vivo modulation of endothelial F-actin microfilaments by experimental alterations in shear stress*. *Arteriosclerosis, Thrombosis, and Vascular Biology*, 1989. 9(4): p. 439-45.
124. Galbraith, C.G., R. Skalak, and S. Chien, *Shear stress induces spatial reorganization of the endothelial cell cytoskeleton*. *Cell Motility and the Cytoskeleton*, 1998. 40(4): p. 317-330.
125. Mengistu, M., et al., *Fluid shear stress-induced JNK activity leads to actin remodeling for cell alignment*. *Journal of Cellular Physiology*, 2011. 226(1): p. 110-121.
126. Katoh K, K.Y., Ookawara S., *Role of stress fibers and focal adhesions as a mediator for mechano-signal transduction in endothelial cells in situ*. *Vasc Health Risk Manag*, 2008. 4(6): p. 1273-1282.
127. Acharya, P.S., et al., *Fibroblast migration is mediated by CD44-dependent TGF β activation*. *Journal of Cell Science*, 2008. 121(9): p. 1393-1402.

128. Pober, J.S. and W.C. Sessa, *Evolving functions of endothelial cells in inflammation*. Nat Rev Immunol, 2007. 7(10): p. 803-815.
129. Jackson, J.R., et al., *The codependence of angiogenesis and chronic inflammation*. The FASEB Journal, 1997. 11(6): p. 457-65.
130. MS, K., *Vascular endothelial cell adhesion and signaling during leukocyte recruitment*. Adv Dermatol, 2004. 20: p. 163-201.
131. Wedmore, C.V. and T.J. Williams, *Control of vascular permeability by polymorphonuclear leukocytes in inflammation*. Nature, 1981. 289(5799): p. 646-650.
132. Arfors, K., et al., *A monoclonal antibody to the membrane glycoprotein complex CD18 inhibits polymorphonuclear leukocyte accumulation and plasma leakage in vivo*. Vol. 69. 1987. 338-340.
133. Williams, T.J. and P.J. Jose, *Mediation of increased vascular permeability after complement activation. Histamine-independent action of rabbit C5a*. The Journal of Experimental Medicine, 1981. 153(1): p. 136-153.
134. Björk, J., P. Hedqvist, and K.-E. Arfors, *Increase in vascular permeability induced by leukotriene b4 and the role of polymorphonuclear leukocytes*. Inflammation, 1982. 6(2): p. 189-200.
135. Tokita, K. and T. Yamamoto, *Differential role of neutrophils and monocytes during subcutaneous plasma extravasation*. Lab Invest, 2004. 84(9): p. 1174-1184.
136. Kerfoot, S.M., et al., *TNF- α -secreting monocytes are recruited into the brain of cholestatic mice*. Hepatology, 2006. 43(1): p. 154-162.
137. Brett, J., et al., *Tumor necrosis factor/cachectin increases permeability of endothelial cell monolayers by a mechanism involving regulatory G proteins*. The Journal of Experimental Medicine, 1989. 169(6): p. 1977-1991.
138. Fransen, L., et al., *Molecular cloning of mouse tumour necrosis factor cDNA and its eukaryotic expression*. Nucleic Acids Research, 1985. 13(12): p. 4417-4429.
139. Kriegler, M., et al., *A novel form of TNF/cachectin is a cell surface cytotoxic transmembrane protein: Ramifications for the complex physiology of TNF*. Cell, 1988. 53(1): p. 45-53.
140. Weis, S.M., *Vascular permeability in cardiovascular disease and cancer*. Current Opinion in Hematology, 2008. 15(3): p. 243-249 10.1097/MOH.0b013e3282f97d86.
141. Kumar, P., et al., *Molecular mechanisms of endothelial hyperpermeability: implications in inflammation*. Expert Reviews in Molecular Medicine, 2009. 11: p. null-null.
142. Muro, S., et al., *A novel endocytic pathway induced by clustering endothelial ICAM-1 or Pendothelial cellAM-1*. Journal of Cell Science, 2003. 116(8): p. 1599-1609.
143. Thomas, S.R., P.K. Witting, and G.R. Drummond, *Redox Control of Endothelial Function and Dysfunction: Molecular Mechanisms and Therapeutic Opportunities*. Antioxidants & Redox Signaling, 2008. 10(10): p. 1713-1766.
144. Chiu, J.-J., et al., *Shear Stress Increases ICAM-1 and Decreases VCAM-1 and E-selectin Expressions Induced by Tumor Necrosis Factor- α in Endothelial Cells*. Arteriosclerosis, Thrombosis, and Vascular Biology, 2004. 24(1): p. 73-79.
145. Thomas, A., J. Tan, and Y. Liu, *Characterization of nanoparticle delivery in microcirculation using a microfluidic device*. Microvascular Research, 2014. 94(0): p. 17-27.
146. Calderon, A.J., et al., *Optimizing endothelial targeting by modulating the antibody density and particle concentration of anti-ICAM coated carriers*. Journal of Controlled Release, 2011. 150(1): p. 37-44.
147. Goldblum SE, D.X., Campbell-Washington J., *TNF- α induces endothelial cell F-actin depolymerization, new actin synthesis, and barrier dysfunction*. Am J Physiol., 1993. 264(4 Pt 1): p. 894-905.
148. Peng, J., et al., *Protein kinase C- α signals P115RhoGEF phosphorylation and RhoA activation in TNF- α -induced mouse brain microvascular endothelial cell barrier dysfunction*. Journal of Neuroinflammation, 2011. 8(1): p. 28.
149. McKenzie, J.A.G. and A.J. Ridley, *Roles of Rho/ROCK and MLCK in TNF- α -induced changes in endothelial morphology and permeability*. Journal of Cellular Physiology, 2007. 213(1): p. 221-228.
150. Yuan, S.Y., *Protein kinase signaling in the modulation of microvascular permeability*. Vascular Pharmacology, 2002. 39(4-5): p. 213-223.
151. Schulte, D., et al., *Stabilizing the VE-cadherin-catenin complex blocks leukocyte extravasation and vascular permeability*. Vol. 30. 2011. 4157-4170.

152. Arce, F.T., et al., *Regulation of the Micromechanical Properties of Pulmonary Endothelium by SIP and Thrombin: Role of Cortactin*. *Biophysical Journal*, 2008. 95(2): p. 886-894.
153. Yuan SY, R.R., *Regulation of Endothelial Barrier Function. San Rafael (CA): Morgan & Claypool Life Sciences; Chapter 5, Signaling Mechanisms in the Regulation of Endothelial Permeability*. 2010.
154. Dvorak, H.F., et al., *Vascular permeability factor/vascular endothelial growth factor, microvascular hyperpermeability, and angiogenesis*. *Am J Pathol*, 1995. 146(5): p. 1029-39.
155. A. A. Miles, E.M.M., *Vascular reactions to histamine, histamine-liberator and leutaxine in the skin of guinea pigs*. *J Physiol*, 1952. 118(2): p. 228–257.
156. Morel, S. and B.R. Kwak, *Roles of connexins in atherosclerosis and ischemia-reperfusion injury*. *Curr Pharm Biotechnol*, 2012. 13(1): p. 17-26.
157. Wang, J.C. and M. Bennett, *Aging and atherosclerosis: mechanisms, functional consequences, and potential therapeutics for cellular senescence*. *Circ Res*, 2012. 111(2): p. 245-59.
158. Funk, S.D., A. Yurdagul, Jr., and A.W. Orr, *Hyperglycemia and endothelial dysfunction in atherosclerosis: lessons from type I diabetes*. *Int J Vasc Med*, 2012. 2012: p. 569654.
159. Lunt, S.J., et al., *Interstitial fluid pressure in tumors: therapeutic barrier and biomarker of angiogenesis*. *Future Oncology*, 2008. 4(6): p. 793-802.
160. Luty, G.A., *Effects of diabetes on the eye*. *Invest Ophthalmol Vis Sci*, 2013. 54(14): p. ORSF81-7.
161. Nagy, J., et al., *Vascular permeability, vascular hyperpermeability and angiogenesis*. *Angiogenesis*, 2008. 11(2): p. 109-119.
162. van Nieuw Amerongen, G.P., et al., *Transient and prolonged increase in endothelial permeability induced by histamine and thrombin: role of protein kinases, calcium, and RhoA*. *Circ Res*, 1998. 83(11): p. 1115-23.
163. Cotran, R.S. and G. Majno, *The Delayed And Prolonged Vascular Leakage In Inflammation. I. Topography Of the Leaking Vessels after Thermal Injury*. *Am J Pathol*, 1964. 45: p. 261-81.
164. Cotran, R.S., *The Delayed And Prolonged Vascular Leakage In Inflammation. Ii. An Electron Microscopic Study Of the Vascular Response after Thermal Injury*. *Am J Pathol*, 1965. 46: p. 589-620.
165. Miles, A.A. and E.M. Miles, *Vascular reactions to histamine, histamine-liberator and leukotaxine in the skin of guinea-pigs*. *The Journal of Physiology*, 1952. 118(2): p. 228-257.
166. Roberts, W.G. and G.E. Palade, *Increased microvascular permeability and endothelial fenestration induced by vascular endothelial growth factor*. *Journal of Cell Science*, 1995. 108(6): p. 2369-2379.
167. Dvorak, H.F., et al., *Induction of a Fibrin-Gel Investment: An Early Event in Line 10 Hepatocarcinoma Growth Mediated by Tumor-Secreted Products*. *The Journal of Immunology*, 1979. 122(1): p. 166-174.
168. Senger, D., et al., *Tumor cells secrete a vascular permeability factor that promotes accumulation of ascites fluid*. *Science*, 1983. 219(4587): p. 983-985.
169. Pink, D.B.S., et al., *Real-Time Visualization and Quantitation of Vascular Permeability *In Vivo*: Implications for Drug Delivery*. *PLoS ONE*, 2012. 7(3): p. e33760.
170. Cooper, J.A., et al., *Measurement of albumin permeability across endothelial monolayers in vitro*. Vol. 62. 1987. 1076-1083.
171. Kerkar, S., et al., *TNF- α and IL-1 β Increase Pericyte/Endothelial Cell Co-Culture Permeability*. *Journal of Surgical Research*, 2006. 132(1): p. 40-45.
172. Mark, K.S. and D.W. Miller, *Increased permeability of primary cultured brain microvessel endothelial cell monolayers following TNF- α exposure*. *Life Sciences*, 1999. 64(21): p. 1941-1953.
173. Albelda, S.M., et al., *Permeability characteristics of cultured endothelial cell monolayers*. Vol. 64. 1988. 308-322.
174. Del Vecchio PJ, S.-B.A., Shepard JM, Bizios R, Cooper JA, Malik AB., *Endothelial monolayer permeability to macromolecules*. *Fed Proc.*, 1987. 46(8): p. 2511-5.
175. Amerongen, G.P.v.N., et al., *Transient and Prolonged Increase in Endothelial Permeability Induced by Histamine and Thrombin: Role of Protein Kinases, Calcium, and RhoA*. *Circulation Research*, 1998. 83(11): p. 1115-1123.
176. Langelier EG, v.H.V., *Characterization of an in vitro model to study the permeability of human arterial endothelial cell monolayers*. *Thromb Haemost*, 1988. 60(2): p. 240-6.
177. Gillies, M.C., et al., *Effect of high glucose on permeability of retinal capillary endothelium in vitro*. *Investigative Ophthalmology & Visual Science*, 1997. 38(3): p. 635-42.

178. Andriopoulou, P., et al., *Histamine Induces Tyrosine Phosphorylation of Endothelial Cell-to-Cell Adherens Junctions*. *Arteriosclerosis, Thrombosis, and Vascular Biology*, 1999. 19(10): p. 2286-2297.
179. Kim, Y., et al., *Probing nanoparticle translocation across the permeable endothelium in experimental atherosclerosis*. *Proceedings of the National Academy of Sciences*, 2014. 111(3): p. 1078-1083.
180. Langelier EG, v.H.V., *Characterization of an in vitro model to study the permeability of human arterial endothelial cell monolayers*. *Thromb Haemost* 1988. 60: p. 240-246.
181. Jo, H., et al., *Endothelial albumin permeability is shear dependent, time dependent, and reversible*. Vol. 260. 1991. H1992-H1996.
182. *Leakier Tumor Vessels Enhance Drug Delivery*. 2010.
183. *Tumors Grow Faster Without Blood-Supply Promoting Molecule*. 2008.
184. *More accolades for omega 3's*.
185. Kris-Etherton, P.M., et al., *Fish Consumption, Fish Oil, Omega-3 Fatty Acids, and Cardiovascular Disease*. *Circulation*, 2002. 106(21): p. 2747-2757.
186. Finsterbusch, M., et al., *Neutrophils recruited by chemoattractants in vivo induce microvascular plasma protein leakage through secretion of TNF*. *The Journal of Experimental Medicine*, 2014. 211(7): p. 1307-1314.
187. *EMD Millipore*
188. *ISODA LAB*.
189. Davies, P.F., *Flow-mediated endothelial mechanotransduction*. Vol. 75. 1995. 519-560.
190. Davies, P.F., T. Mundel, and K.A. Barbee, *A mechanism for heterogeneous endothelial responses to flow in vivo and in vitro*. *Journal of Biomechanics*, 1995. 28(12): p. 1553-1560.
191. Ingber, D.E., *Mechanical Signaling and the Cellular Response to Extracellular Matrix in Angiogenesis and Cardiovascular Physiology*. *Circulation Research*, 2002. 91(10): p. 877-887.
192. Shyy, J.Y.-J. and S. Chien, *Role of Integrins in Endothelial Mechanosensing of Shear Stress*. *Circulation Research*, 2002. 91(9): p. 769-775.
193. Mehta, D. and A.B. Malik, *Signaling Mechanisms Regulating Endothelial Permeability*. *Physiological Reviews*, 2005. 86(1): p. 279-367.
194. Kuebler, W.M., X. Ying, and J. Bhattacharya, *Pressure-induced endothelial Ca²⁺ oscillations in lung capillaries*. *American Journal of Physiology - Lung Cellular and Molecular Physiology*, 2002. 282(5): p. L917-L923.
195. Nollert, M.U., S.G. Eskin, and L.V. McIntire, *Shear stress increases inositol trisphosphate levels in human endothelial cells*. *Biochemical and Biophysical Research Communications*, 1990. 170(1): p. 281-287.
196. Schwarz, G., et al., *Shear stress-induced calcium transients in endothelial cells from human umbilical cord veins*. *The Journal of Physiology*, 1992. 458: p. 527-538.
197. Hu, Y.L., et al., *Roles of Microtubule Dynamics and Small GTPase Rac in Endothelial Cell Migration and Lamellipodium Formation under Flow*. *Journal of Vascular Research*, 2002. 39(6): p. 465-476.
198. Tzima, E., et al., *Activation of Rac1 by shear stress in endothelial cells mediates both cytoskeletal reorganization and effects on gene expression*. Vol. 21. 2002. 6791-6800.
199. Birukov, K.G., et al., *Magnitude-dependent regulation of pulmonary endothelial cell barrier function by cyclic stretch*. *American Journal of Physiology - Lung Cellular and Molecular Physiology*, 2003. 285(4): p. L785-L797.
200. Rabiet, M.-J., et al., *Thrombin-Induced Increase in Endothelial Permeability Is Associated With Changes in Cell-to-Cell Junction Organization*. *Arteriosclerosis, Thrombosis, and Vascular Biology*, 1996. 16(3): p. 488-496.
201. Garcia, J.G.N., et al., *Inflammatory Events after Fibrin Microembolization: Alterations in Alveolar Macrophage and Neutrophil Function*. *American Review of Respiratory Disease*, 1988. 137(3): p. 630-635.
202. N. V. Bogatcheva, J.G.N.G., and A. D. Verin, *Molecular Mechanisms of Thrombin-Induced Endothelial Cell Permeability*. *Biochemistry*, 2001. 67(1): p. 75-84.
203. Tsukita, S., et al., *Molecular linkage between cadherins and actin filaments in cell-cell adherens junctions*. *Current Opinion in Cell Biology*, 1992. 4(5): p. 834-839.
204. Dejana, E., M. Corada, and M.G. Lampugnani, *Endothelial cell-to-cell junctions*. *The FASEB Journal*, 1995. 9(10): p. 910-8.

205. Kemler, R., *From cadherins to catenins: cytoplasmic protein interactions and regulation of cell adhesion*. Trends in Genetics, 1993. 9(9): p. 317-321.
206. Coughlin, S.R., et al., *Characterization of a functional thrombin receptor. Issues and opportunities*. Journal of Clinical Investigation, 1992. 89(2): p. 351-355.
207. Antony Thomas, H.D.O.-Y., Linda Lowe-Krentz, Vladimir R. Muzykantov, Yaling Liu., *Biomimetic channel modeling local vascular dynamics of pro-inflammatory endothelial changes*. Under Review, 2015.
208. Baron, D.A., et al., *Atriopeptin inhibition of thrombin-mediated changes in the morphology and permeability of endothelial monolayers*. Proceedings of the National Academy of Sciences of the United States of America, 1989. 86(9): p. 3394-3398.
209. Stockton, R.A., E. Schaefer, and M.A. Schwartz, *p21-activated Kinase Regulates Endothelial Permeability through Modulation of Contractility*. Journal of Biological Chemistry, 2004. 279(45): p. 46621-46630.
210. Buchan, K.W. and W. Martin, *Modulation of barrier function of bovine aortic and pulmonary artery endothelial cells: dissociation from cytosolic calcium content*. British Journal of Pharmacology, 1992. 107(4): p. 932-938.
211. van Nieuw Amerongen, G.P., et al., *GIT1 Mediates Thrombin Signaling in Endothelial Cells: Role in Turnover of RhoA-Type Focal Adhesions*. Circulation Research, 2004. 94(8): p. 1041-1049.
212. Stockton, R., et al., *Induction of Vascular Permeability: β PIX and GIT1 Scaffold the Activation of Extracellular Signal-regulated Kinase by PAK*. Molecular Biology of the Cell, 2007. 18(6): p. 2346-2355.
213. Chang, Y.S., et al., *Effect of Vascular Endothelial Growth Factor on Cultured Endothelial Cell Monolayer Transport Properties*. Microvascular Research, 2000. 59(2): p. 265-277.
214. Hoffmann, A., et al., *High and Low Molecular Weight Fluorescein Isothiocyanate (FITC)-Dextrans to Assess Blood-Brain Barrier Disruption: Technical Considerations*. Translational Stroke Research, 2011. 2(1): p. 106-111.
215. Sahagun, G., S.A. Moore, and M.N. Hart, *Permeability of neutral vs. anionic dextrans in cultured brain microvascular endothelium*. Vol. 259. 1990. H162-H166.
216. Gribbon, P. and T.E. Hardingham, *Macromolecular Diffusion of Biological Polymers Measured by Confocal Fluorescence Recovery after Photobleaching*. Biophysical Journal, 1998. 75(2): p. 1032-1039.
217. Bryers, J.D. and F. Drummond, *Local macromolecule diffusion coefficients in structurally non-uniform bacterial biofilms using fluorescence recovery after photobleaching (FRAP)*. Biotechnology and Bioengineering, 1998. 60(4): p. 462-473.
218. Periasamy, N. and A.S. Verkman, *Analysis of fluorophore diffusion by continuous distributions of diffusion coefficients: application to photobleaching measurements of multicomponent and anomalous diffusion*. Biophysical Journal, 1998. 75(1): p. 557-567.
219. Tiruppathi, C., et al., *Synergistic effects of tumor necrosis factor- α and thrombin in increasing endothelial permeability*. Vol. 281. 2001. L958-L968.
220. Goeckeler, Z.M. and R.B. Wysolmerski, *Myosin light chain kinase-regulated endothelial cell contraction: the relationship between isometric tension, actin polymerization, and myosin phosphorylation*. The Journal of Cell Biology, 1995. 130(3): p. 613-627.
221. Sandoval, R., et al., *Requirement for Ca^{2+} signaling in the mechanism of thrombin-induced increase in endothelial permeability*. Vol. 280. 2001. L239-L247.
222. Wysolmerski, R.B. and D. Lagunoff, *Involvement of myosin light-chain kinase in endothelial cell retraction*. Proceedings of the National Academy of Sciences, 1990. 87(1): p. 16-20.
223. Alieva, I.B., et al., *The Leading Role of Microtubules in Endothelial Barrier Dysfunction: Disassembly of Peripheral Microtubules Leaves Behind the Cytoskeletal Reorganization*. Journal of cellular biochemistry, 2013. 114(10): p. 2258-2272.
224. Aird, W.C., *Endothelial cell dynamics and complexity theory*. Critical Care Medicine, 2002. 30(5): p. S180-S185.
225. Minami, T., et al., *Thrombin and Phenotypic Modulation of the Endothelium*. Arteriosclerosis, Thrombosis, and Vascular Biology, 2004. 24(1): p. 41-53.
226. Aird, W.C., *Endothelial cell heterogeneity*. Critical Care Medicine, 2003. 31(4): p. S221-S230.
227. Cirino, G., et al., *Thrombin functions as an inflammatory mediator through activation of its receptor*. The Journal of Experimental Medicine, 1996. 183(3): p. 821-827.

228. Kim, M.-H., F.-R.E. Curry, and S.I. Simon, *Dynamics of neutrophil extravasation and vascular permeability are uncoupled during aseptic cutaneous wounding*. American Journal of Physiology - Cell Physiology, 2009. 296(4): p. C848-C856.
229. Curry, F.E., M. Zeng, and R.H. Adamson, *Thrombin increases permeability only in venules exposed to inflammatory conditions*. Vol. 285. 2003. H2446-H2453.
230. Kouklis, P., et al., *Cdc42 Regulates the Restoration of Endothelial Barrier Function*. Circulation Research, 2004. 94(2): p. 159-166.
231. Zhao, Y.D., et al., *Bone marrow-derived progenitor cells prevent thrombin-induced increase in lung vascular permeability*. Vol. 298. 2010. L36-L44.
232. Birukova, A.A., et al., *GEF-H1 is involved in agonist-induced human pulmonary endothelial barrier dysfunction*. Vol. 290. 2006. L540-L548.
233. Mehta, D. and A.B. Malik, *Signaling Mechanisms Regulating Endothelial Permeability*. Vol. 86. 2006. 279-367.
234. Tiruppathi, C., et al., *Electrical method for detection of endothelial cell shape change in real time: assessment of endothelial barrier function*. Proceedings of the National Academy of Sciences, 1992. 89(17): p. 7919-7923.
235. Mehta, D., et al., *Modulatory role of focal adhesion kinase in regulating human pulmonary arterial endothelial barrier function*. The Journal of Physiology, 2002. 539(Pt 3): p. 779-789.
236. Minshall, R.D., et al., *Role of Protein Kinase C ζ in Thrombin-induced RhoA Activation and Interendothelial Gap Formation of Human Dermal Microvessel Endothelial Cell Monolayers*. Microvascular Research, 2010. 80(2): p. 240-249.
237. Esch, M.B., T.L. King, and M.L. Shuler, *The Role of Body-on-a-Chip Devices in Drug and Toxicity Studies*. Annual Review of Biomedical Engineering, 2011. 13(1): p. 55-72.
238. GA, T., *Endothelial Cell Vascular Smooth Muscle Cell Co-Culture Assay For High Throughput Screening Assays For Discovery of Anti-Angiogenesis Agents and Other Therapeutic Molecules*. Int J High Throughput Screen, 2010. 1: p. 171-181.
239. Chiu, J.-J., et al., *Shear stress inhibits adhesion molecule expression in vascular endothelial cells induced by coculture with smooth muscle cells*. Vol. 101. 2003. 2667-2674.
240. Rainger, G.E., et al., *A novel system for investigating the ability of smooth muscle cells and fibroblasts to regulate adhesion of flowing leukocytes to endothelial cells*. Journal of Immunological Methods, 2001. 255(1-2): p. 73-82.
241. Fillinger, M.F., et al., *Coculture of Endothelial Cells and Smooth Muscle Cells in Bilayer and Conditioned Media Models*. Journal of Surgical Research, 1997. 67(2): p. 169-178.
242. Nackman, G.B., et al., *Endothelial cells modulate smooth muscle cell morphology by inhibition of transforming growth factor-beta1 activation*. Surgery, 1996. 120(2): p. 418-426.
243. Bianchi, E., et al., *Microfluidics for in vitro biomimetic shear stress-dependent leukocyte adhesion assays*. Journal of Biomechanics, 2013. 46(2): p. 276-283.
244. Heldin, C.H., et al., *High interstitial fluid pressure - an obstacle in cancer therapy*. Nat Rev Cancer, 2004. 4(10): p. 806-13.
245. Sutcliffe, S. and G.A. Colditz, *Prostate cancer: is it time to expand the research focus to early-life exposures?* Nat Rev Cancer, 2013. 13(3): p. 208-518.
246. Saharinen, P., et al., *VEGF and angiopoietin signaling in tumor angiogenesis and metastasis*. Trends in Molecular Medicine, 2011. 17(7): p. 347-362.
247. Zaravinos, A., et al., *Expression of miRNAs Involved in Angiogenesis, Tumor Cell Proliferation, Tumor Suppressor Inhibition, Epithelial-Mesenchymal Transition and Activation of Metastasis in Bladder Cancer*. The Journal of Urology, 2012. 188(2): p. 615-623.
248. Carmeliet, P. and R.K. Jain, *Angiogenesis in cancer and other diseases*. Nature, 2000. 407(6801): p. 249-257.

Curriculum Vitae

EDUCATION

- PhD, Bioengineering August 2015
- Master of Science, Bioengineering May 2012
- **Lehigh University**, Bethlehem, PA, U.S.A
- Bachelor of Technology**, Biomedical Engineering: May 2008
- **Sathyabama University**, Chennai, India

PROJECTS

Probing endothelial microenvironment characteristics on biomimetic blood vessel microfluidic models (Thesis)

Developed couple of *in vitro* blood vessel microfluidic platforms modeling physiologically relevant conditions

1) Cell receptor protein coated microfluidic channel modeling blood microvessels under inflammatory condition

- Characterized binding properties of 'ligand protein' coated model drug carrier particles (nano and micron size)
- Studied parameters for optimal drug carrier targeting in specific vascular geometries and hemodynamic conditions

2) Endothelial cell monolayer cultured in dual chamber microfluidic device; modeling quiescent and inflammatory states

- Capable of growing cells under flow, localized signaling-molecule triggering & real-time *in situ* study
- Studied cellular signaling and cytoskeletal dynamics in local vascular microenvironment during inflammation
- Current studies: Quantifying blood vessel permeability, Investigating endothelial cell-tumor interaction mechanisms
- In process of **commercializing** the blood vessel mimicking chip through 'QED program' and 'Particle Sciences Inc.'

US Provisional patent application # 62/078,471: Biomimetic blood vessel model to study local microvascular dynamics

Circulating Tumor Cell (CTC) capture on Micro-patterned surfaces

- Investigated CTC capture on antibody coated wave, herringbone & wave herringbone micron scale patterns
- Wave herringbone pattern induces mixing, enhances interaction between CTCs and the antibody coated surface
- Achieved high throughput CTC capture with high specificity and efficiency

DNA-Gold nanoparticle assembly towards bio-generating cell based shapes

- Fluorescent ssDNA oligonucleotide probes attached on gold NPs are uniformly and densely arranged on RBCs
- A closed lock structure is obtained through DNA hybridization. Mimics cell based shapes on RBC lysis

Enhanced specific uptake of nanodrug carriers in mammalian cells based on Sonoporation

- Cancer cells exposed to varying levels of ultrasound & microbubbles induce pore formation on cell membrane
- Studied targeted uptake of protein coated nanoparticles on these cells

SELECTED PUBLICATIONS

Antony Thomas, Yaling Liu (2015). Characterizing vascular permeability using a biomimetic microfluidic blood vessel model . *Under preparation*

Antony Thomas, Ou-Yang HD, Lowe-Krentz L, Muzykantov VR, Yaling Liu (2015). *In vitro* study on cellular level understanding of targeted drug delivery on a biomimetic blood vasculature model, *Under review(Biomaterials)*

Antony Thomas, Jifu Tan, Yaling Liu (2014). Characterization of nanoparticle delivery in microcirculation using a microfluidic device, *Microvascular Research*. 9: 17–27

Jifu Tan, Shah S, **Antony Thomas**, Ou-Yang HD, Yaling Liu (2013). The influence of size, shape and vessel geometry on nanoparticle distribution, *Microfluidics and Nanofluidics*. 14(1-2):77-87

Yaling Liu, Jifu Tan, **Antony Thomas**, Ou-Yang HD, Muzykantov VR (2012). The shape of things to come: importance of design in nanotechnology for drug delivery, *Therapeutic Delivery*. 3(2):181-94.

Jifu Tan, **Antony Thomas**, Yaling Liu (2011). Influence of Blood Cell-Particle Interaction on Nanoparticle Targeted Delivery in Microcirculation, *Soft Matter*. 8(6):1934-1946

HONORS & OTHER SKILLS

- Interviewed and work on 'CTC capture on Micro-patterned surfaces' featured on *Resolve magazine, Volume 1, 2015*
- P.C. Rossin Doctoral Fellow Award 2014; P.C. Rossin College of Engineering, Lehigh University
- Awarded the top prize in podium presentation at the annual Northeast Bioengineering Conference 2012
- Interviewed and work on targeted drug delivery featured on *Resolve magazine, Volume 1, 2012*
- Research project won first place in 2012 Lehigh annual research symposium
- Strong analytical, communication, presentation and interpersonal skills. Able to work in cross-disciplinary domain
- Diligent team player with ability to lead, and focus on improvement and success